

CARRIER TRANSPORT, RECOMBINATION, AND THE EFFECTS OF
GRAIN BOUNDARIES IN POLYCRYSTALLINE CADMIUM
TELLURIDE THIN FILMS FOR PHOTOVOLTAICS

BY

MOHIT TUTEJA

DISSERTATION

Submitted in partial fulfillment of the requirements
for the degree of Doctor of Philosophy in Materials Science and Engineering
in the Graduate College of the
University of Illinois at Urbana-Champaign, 2016

Urbana, Illinois

Doctoral Committee:

Professor Emeritus Angus A. Rockett, Chair
Professor Emeritus John R. Abelson
Assistant Professor Elif Ertekin
Assistant Professor André Schleife

ABSTRACT

Cadmium Telluride (CdTe), a chalcogenide semiconductor, is currently used as the absorber layer in one of the highest efficiency thin film solar cell technologies. Current efficiency records are over 22%. In 2011, CdTe solar cells accounted for ~8% of all solar cells installed. This is because, in part, CdTe has a low degradation rate, high optical absorption coefficient, and high tolerance to intrinsic defects. Solar cells based on polycrystalline CdTe exhibit a higher short-circuit current, fill factor, and power conversion efficiency than their single crystal counterparts. This is despite the fact that polycrystalline CdTe devices exhibit lower open-circuit voltages. This is contrary to the observation for silicon and III-V semiconductors, where material defects cause a dramatic drop in device performance. For example, grain boundaries in covalently-bonded semiconductors (a) act as carrier recombination centers, and (b) lead to localized energy states, causing carrier trapping. Despite significant research to date, the mechanism responsible for the superior current collection properties of polycrystalline CdTe solar cells has not been conclusively answered. This dissertation focuses on the macro-scale electronic band structure, and micro scale electronic properties of grains and grain boundaries in device-grade CdTe thin films to answer this open question.

My research utilized a variety of experimental techniques. Samples were obtained from leading groups fabricating the material and devices. A CdCl₂ anneal is commonly performed as part of this fabrication and its effects were also investigated. Photoluminescence (PL) spectroscopy was employed to study the band structure and defect states in CdTe polycrystals. Cadmium vacancy- and chlorine-related states lead to carrier recombination, as in CdTe films grown by other methods. Comparing polycrystalline and single crystal CdTe, showed that the key to explaining the improved performance of polycrystalline CdTe does not lie in macroscopic analysis. The nanoscale majority carrier concentration was studied using scanning microwave impedance microscopy, which revealed an existence of majority carrier depletion along the grain boundaries, independent of the growth process used, which was absent in films that were not subjected to CdCl₂ annealing. This effect promotes carrier separation and collection. Conductive atomic force microscopy showed enhanced conduction of electrons along the

grain boundaries in samples subjected to the CdCl_2 anneal treatment while holes were shown to move through the grain bulk. The separation of conduction channels minimizes recombination while simultaneously reducing series resistance and hence enhancing fill factor. Several technical capabilities demonstrated in this work can be easily extended to other semiconductor materials.

ACKNOWLEDGEMENTS

The research presented in this dissertation was possible in part due to the contribution of a number of people. I am grateful to have received the opportunity to interact with them and would like to express my sincere appreciation to:

- My parents, Gyan Chand Tuteja and Renu Bala Tuteja, and my sister, Falguni Tuteja, for always being loving, kind, encouraging, and supportive.
- Ragini Chaurasia, for your unconditional support.
- Prof. Angus Rockett, for being an extraordinarily supportive advisor. Thank you for providing me the liberty and opportunity to pursue the research that interests me. I could not have asked for a better supervisor.
- Dr. Scott MacLaren, for introducing me to scanning probe microscopy and providing so much instrument time for me to “play” with various experimental techniques. I can never thank you enough for all the opportunities that you have provided me.
- Dr. Julio Soares, for training me on the first instrument I used in the MRL.
- Dr. Aditya Mohite and Dr. Gautam Gupta, for taking me under your wing and providing me the awesome experience of working at Los Alamos National Lab.
- Prof. John Abelson, Prof. Elif Ertekin, and Prof. André Schleife, for agreeing to be a part of my thesis committee and for providing feedback at critical times.
- Allen Hall and Antonio Mei, for the numerous helpful ideas and discussions.
- Dr. Vasilios Palekis, Dr. Prakash Koirala, Prof. Rob Collins, and Prof. Chris Ferekides, for providing critical research samples needed for this dissertation and for proof reading the manuscripts.
- Salvatore DeSando, for being an awesome friend. I have thoroughly enjoyed all our interactions.
- Pamela Martin, Minjee Kang, Elham Mohimi, Nicole Johnson, and Kara Kearney, for the numerous enjoyable conversations.
- Mauro Sardela, Doug Jeffers, Kathy Walsh, and Steve Burdin, for helping me on numerous occasions and making me feel welcome in MRL.

- Michelle Malloch, Sandra Helregel, Allison Sutton, Debbie Kludge, Jay Menacher, Susan Lighty, and Chris Johns, for being helpful office staff and helping me navigate the University bureaucracy.
- Russel, our building custodian, for reminding me on several occasions that I am not the only one working at 4 am in the building.

TABLE OF CONTENTS

CHAPTER 1: INTRODUCTION.....	1
1.1 Motivation.....	1
1.2 Thesis Statement.....	2
1.3 Thesis Summary.....	2
1.4 References.....	6
CHAPTER 2: BACKGROUND.....	8
2.1 Thin Film CdTe Photovoltaics.....	8
2.2 CdCl ₂ Anneal Treatment for CdTe Photovoltaics.....	10
2.3 Photoluminescence Spectroscopy of CdTe.....	10
2.4 Micro-scale Electronic Properties of CdTe.....	11
2.5 Near-Field Microscopy and Microwave Microscopy	13
2.6 Scanning Microwave Impedance Microscopy.....	15
2.7 Conductive Atomic Force Microscopy.....	15
2.8 Figures.....	16
2.9 References.....	21
CHAPTER 3: EXPERIMENTAL METHODS.....	26
3.1 CdTe Solar Cell Fabrication.....	26
3.2 Photoluminescence Spectroscopy.....	27
3.3 Scanning Microwave Impedance Microscopy.....	28
3.4 Conductive Atomic Force Microscopy.....	31
3.5 Figures.....	32
3.6 References.....	36
CHAPTER 4: DEFECT LEVELS IN THE MACROSCOPIC BAND STRUCTURE.....	38
4.1 Introduction.....	38
4.2 Results.....	38
4.3 Discussion.....	43
4.4 Conclusions.....	46
4.5 Figures.....	48
4.6 References.....	54
CHAPTER 5: RELATIVE MAJORITY CARRIER CONCENTRATION DISTRIBUTION AT THE MICROSCALE.....	57
5.1 Introduction.....	57
5.2 Anticipated Effects of the CdCl ₂ Annealing Process.....	57
5.3 Results.....	58
5.4 Discussion.....	62
5.5 Conclusions.....	63
5.6 Figures.....	65
5.7 References.....	71

CHAPTER 6: MICROSCALE ELECTRONIC CONDUCTIVITY.....	73
6.1 Introduction.....	73
6.2 Results.....	73
6.3 Discussion.....	76
6.4 Conclusions.....	79
6.5 Figures.....	80
6.6 References.....	86
CHAPTER 7: CONCLUSIONS.....	87
7.1 Conclusions.....	87
7.2 Suggested Optimal Device Structure.....	88
7.3 Figures.....	89
7.4 Reference.....	91

CHAPTER 1

INTRODUCTION

1.1 Motivation

Solar cells are likely to become a major player in the energy sector for a number of reasons. Cutting back significantly on production of pollution is vital to ensuring that the earth is able to sustain life. The use of fossil fuels, especially coal, as an energy source has significant drawbacks, particularly in the lasting effects of the pollution it generates. Moving toward alternate sources of electricity that do not produce pollution is critical. Solar energy harvesting technologies provide a clean and renewable option for supplying electricity for households or industrial use.

Thin films of a-Si, CdTe, and Cu(In,Ga)Se₂ and related I-III-VI₂ compounds have been of great interest to both the research and commercial solar cell communities because of their many advantageous properties over bulk crystalline technologies. Due to their high absorption coefficients ($> 10^4 \text{ cm}^{-1}$) [1], only 1-4 μm of the material are needed to absorb the incoming radiation, as opposed to crystalline silicon where tens of microns are required to obtain similar results. This leads to a decrease in the material needed for the thin film devices, which translates to lower costs and processing time. These materials are ideal for deposition on flexible, lightweight substrates. CdTe photovoltaic technology is economically competitive and commercially viable, and its champion device boasts a champion power conversion efficiency $>22\%$ [2], [3].

It is well known that single crystal silicon solar cells far outperform their multi-crystalline counterparts, whose grain boundaries getter impurities and trap carriers, promoting recombination. In contrast, single crystal CdTe devices have never been shown to produce as efficient devices as those made from polycrystalline CdTe [4]. This is in addition to the fact that single crystal devices often are grown on CdTe bulk crystals [5], [6] or GaAs [7], both of which are expensive substrates that increase the cost of device fabrication. There have been several investigations that have attempted to answer the puzzling question of the superior performance of the polycrystalline CdTe solar cells [4], [8]–[11]. Some of these, often conflicting, studies conclude that the electronic structure of the grain boundaries is the key to understanding the superior performance

[11]–[15]. The disagreement is primarily because analysis of the electronic properties of grain boundaries is challenging since interaction volumes probed by conventional characterization techniques span multiple grains. Individual grain boundary properties have been investigated via electron beam induced current (EBIC) [11], [14]–[16]; combinations of scanning capacitance microscopy (SCM), conductive atomic force microscopy (C-AFM), and scanning Kelvin probe force microscopy [4], [17], [18]; and near-field optical beam induced current (OBIC) [14], [19]. While these are great characterization techniques, they suffer from resolution limitations or sample topography-induced measurement artifacts that preclude precise measurements of local grain boundary properties that exist on much smaller length scales of 50-100 nm or less. Understanding the effect of grain boundaries is exacerbated by the changes that result from CdCl_2 anneal treatment that improves device performance. There are only a few studies that have compared CdTe films without and with the CdCl_2 treatment.

The purpose of this work is to study the macro- and micro-scale electronic properties of polycrystalline CdTe solar cells using established and emerging techniques based on optical spectroscopy and scanning probe microscopy (SPM) methods. Device-quality CdTe thin films grown by various techniques, with and without the CdCl_2 treatment, were analyzed in order to ascertain the properties of these films as a function of growth methodologies and CdCl_2 annealing treatment.

1.2 Thesis Statement

By analysis of the electronic properties of device-quality polycrystalline CdTe films grown using rf-sputtering and closed space sublimation (CSS) (processes that yield up to 13% and 16% efficient devices, respectively) at the macro and micro scale the effects of growth methodologies, device processing treatments, and external sample illumination on the electronic behavior can be understood. Their effects on the performance of a completed device can then be derived.

1.3 Thesis Summary

The relevant background information for this work is presented in **Chapter 2**. This includes information about CdTe photovoltaics, electronic properties of

polycrystalline CdTe thin films, and optical and SPM-based characterization of CdTe films. The experimental methods are detailed in **Chapter 3**. This includes the CdTe fabrication methods used in this work. This is followed by a discussion of the various methods that were used to characterize the optical and electronic properties of the CdTe films. A detailed description of the experimental setup and analysis conditions are given for each set of experiments.

Chapter 4 describes the macro scale electronic band structure measurements via photoluminescence spectroscopy to characterize the defect levels and the associated radiative carrier recombination mechanisms in rf-sputtered polycrystalline CdTe films. Different interfaces of the CdTe were analyzed and the results were compared. Optical transitions have been identified and studied as a function of sample temperature and laser excitation power. Significant sub-gap transitions were observed prior to deposition of the Cu-containing back contact. These transitions were compared with those from the spectroscopic studies on single crystal CdTe and CSS-grown polycrystalline CdTe films.

Chapter 5 describes the nanoscale distribution of majority carriers on exposed CdTe film surfaces using scanning microwave impedance microscopy (sMIM), an emerging SPM-based technique. A set of CdTe films, grown using rf-sputtering and CSS, with and without CdCl₂ treatment, were analyzed to study the effects of growth methodologies and the CdCl₂ anneal treatment on the electronic properties of the grains and the grain boundaries. In addition, sMIM measurements were performed with and without external sample illumination using a white light source in order to study the effect of illumination on the nanoscale charge carrier distribution. It was found that the CdCl₂ treatment induces compensation of the grain boundary p-doping of an otherwise p-doped CdTe film. This leads to downward band-bending along the grain boundary, which promotes charge carrier segregation and aids the photovoltaic effect.

Chapter 6 discusses characterization of the nanoscale electronic conductivity of the CdTe films, with and without CdCl₂ treatment, using conductive atomic force microscopy (C-AFM). This measured the current flow/charge transport pathways and provided information about charge transport to the front/back contacts. After the CdCl₂

treatment the CdTe shows enhanced current conduction along the grain boundary areas, an effect not observed in the non-CdCl₂ treated samples. This was concluded to show the conduction of electrons along the grain boundaries in the CdCl₂ treated sample.

This thesis ends with **Chapter 7**, which lists the conclusions arrived at from the above work, proposes ideal device structures for achieving improved device efficiencies, and suggests routes for continuation of this work in the future.

The results contained in this dissertation are also published in the following works:

Chapter 4: [P1] **M. Tuteja**, P. Koirala, J. Soares, R. Collins, and A. Rockett, “Low temperature photoluminescence spectroscopy studies on sputter deposited CdS/CdTe junctions and solar cells,” *Journal of Materials Research*, vol. 31, no. 02, pp. 186–194, 2016.

Chapter 5: [P2] **M. Tuteja**, P. Koirala, S. MacLaren, R. Collins, and A. Rockett, “Direct observation of electrical properties of grain boundaries in sputter-deposited CdTe using scan-probe microwave reflectivity based capacitance measurements,” *Applied Physics Letters*, vol. 107, no. 14, p. 142106, Oct. 2015.

[P3] **M. Tuteja**, P. Koirala, V. Palekis, S. MacLaren, C. S. Ferekides, R. W. Collins, and A. A. Rockett, “Direct Observation of CdCl₂ Treatment Induced Grain Boundary Carrier Depletion in CdTe Solar Cells Using Scanning Probe Microwave Reflectivity Based Capacitance Measurements,” *J. Phys. Chem. C*, vol. 120, no. 13, pp. 7020–7024, Apr. 2016.

[P4] **M. Tuteja**, P. Koirala, V. Palekis, S. MacLaren, C. S. Ferekides, R. W. Collins, and A. A. Rockett, “Measuring relative carrier concentrations at the nanoscale using scanning microwave impedance microscopy: The case of CdTe solar cells,” *Conference Record of the 43rd IEEE PVSC*, 2016.

Chapter 6: [P5] **M. Tuteja**, A. Mei, V. Palekis, A. Hall, S. MacLaren, C.S. Ferekides, and A.A. Rockett, “CdCl₂ Treatment-Induced Enhanced Conductivity in CdTe Solar

Cells Observed Using Conductive-Atomic Force Microscopy,” *submitted to J. Phys. Chem. Lett.* (October 2016).

In addition to the work outlined in this thesis, I have contributed to other projects that have resulted in the following publication:

[P6] A. B. Mei, **M. Tuteja**, D. G. Sangiovanni, R. T. Haasch, A. Rockett, L. Hultman, I. Petrov, and J. E. Greene, “Growth, nanostructure, and optical properties of epitaxial $\text{VN}_x/\text{MgO}(001)$ ($0.80 \leq x \leq 1.00$) layers deposited by reactive magnetron sputtering,” *J. Mater. Chem. C*, vol. 4, no. 34, pp. 7924–7938, Aug. 2016.

Some text and figures in Chapters 3-6 are taken from the publications mentioned above. In all cases, adequate permissions were obtained from the publishers to reproduce the material.

1.4 References

- [1] N. Kavcar, “Study of the sub-bandgap absorption and the optical transitions in CuInSe₂ polycrystalline thin films,” *Sol. Energy Mater. Sol. Cells*, vol. 52, no. 1–2, pp. 183–195, Mar. 1998.
- [2] Press Release, “First Solar achieves yet another cell conversion efficiency world record.” 23-Feb-2016.
- [3] M. A. Green, K. Emery, Y. Hishikawa, W. Warta, and E. D. Dunlop, “Solar cell efficiency tables (version 48),” *Prog. Photovolt. Res. Appl.*, vol. 24, no. 7, pp. 905–913, Jul. 2016.
- [4] I. Visoly-Fisher, S. R. Cohen, A. Ruzin, and D. Cahen, “How Polycrystalline Devices Can Outperform Single-Crystal Ones: Thin Film CdTe/CdS Solar Cells,” *Adv. Mater.*, vol. 16, no. 11, pp. 879–883, Jun. 2004.
- [5] J. M. Burst *et al.*, “CdTe solar cells with open-circuit voltage breaking the 1 V barrier,” *Nat. Energy*, vol. 1, no. 3, p. 16015, Feb. 2016.
- [6] P.-Y. Su, R. Dahal, G.-C. Wang, S. Zhang, T.-M. Lu, and I. B. Bhat, “Single-Crystal CdTe Homojunction Structures for Solar Cell Applications,” *J. Electron. Mater.*, pp. 1–6, May 2015.
- [7] P.-Y. Su, C. Lee, G.-C. Wang, T.-M. Lu, and I. B. Bhat, “CdTe/ZnTe/GaAs Heterostructures for Single-Crystal CdTe Solar Cells,” *J. Electron. Mater.*, vol. 43, no. 8, pp. 2895–2900, May 2014.
- [8] I. Visoly-Fisher, S. R. Cohen, and D. Cahen, “Direct evidence for grain-boundary depletion in polycrystalline CdTe from nanoscale-resolved measurements,” *Appl. Phys. Lett.*, vol. 82, no. 4, pp. 556–558, Jan. 2003.
- [9] I. Visoly-Fisher, S. R. Cohen, K. Gartsman, A. Ruzin, and D. Cahen, “Understanding the Beneficial Role of Grain Boundaries in Polycrystalline Solar Cells from Single-Grain-Boundary Scanning Probe Microscopy,” *Adv. Funct. Mater.*, vol. 16, no. 5, pp. 649–660, Mar. 2006.
- [10] P. Sutter, E. Sutter, and T. R. Ohno, “High-resolution mapping of nonuniform carrier transport at contacts to polycrystalline CdTe/CdS solar cells,” *Appl. Phys. Lett.*, vol. 84, no. 12, pp. 2100–2102, Mar. 2004.

- [11] C. Li *et al.*, “Grain-Boundary-Enhanced Carrier Collection in CdTe Solar Cells,” *Phys. Rev. Lett.*, vol. 112, no. 15, p. 156103, Apr. 2014.
- [12] L. M. Woods, G. Y. Robinson, and D. H. Levi, “The effects of CdCl₂ on CdTe electrical properties using a new theory for grain-boundary conduction,” in *Conference Record of the Twenty-Eighth IEEE Photovoltaic Specialists Conference, 2000*, 2000, pp. 603–606.
- [13] L. M. Woods, D. H. Levi, V. Kaydanov, G. Y. Robinson, and R. K. Ahrenkiel, “Electrical characterization of etched grain-boundary properties from as-processed px-CdTe-based solar cells,” in *AIP Conference Proceedings*, 1999, vol. 462, pp. 499–504.
- [14] S. A. Galloway, P. R. Edwards, and K. Durose, “Characterisation of thin film CdS/CdTe solar cells using electron and optical beam induced current,” *Sol. Energy Mater. Sol. Cells*, vol. 57, no. 1, pp. 61–74, Feb. 1999.
- [15] P. R. Edwards, S. A. Galloway, and K. Durose, “EBIC and luminescence mapping of CdTe/CdS solar cells,” *Thin Solid Films*, vol. 361–362, pp. 364–370, Feb. 2000.
- [16] J. D. Poplawsky *et al.*, “Direct Imaging of Cl- and Cu-Induced Short-Circuit Efficiency Changes in CdTe Solar Cells,” *Adv. Energy Mater.*, vol. 4, no. 15, p. 1400454, Oct. 2014.
- [17] I. Visoly-Fisher, S. R. Cohen, and D. Cahen, “Direct evidence for grain-boundary depletion in polycrystalline CdTe from nanoscale-resolved measurements,” *Appl. Phys. Lett.*, vol. 82, no. 4, pp. 556–558, Jan. 2003.
- [18] W. S. M. Brooks, S. J. C. Irvine, and D. M. Taylor, “Scanning Kelvin probe measurements on As-doped CdTe solar cells,” *Semicond. Sci. Technol.*, vol. 28, no. 10, p. 105024, 2013.
- [19] S. Smith, P. Zhang, T. Gessert, and A. Mascarenhas, “Near-field optical beam-induced currents in CdTe/CdS solar cells: Direct measurement of enhanced photoresponse at grain boundaries,” *Appl. Phys. Lett.*, vol. 85, no. 17, pp. 3854–3856, Oct. 2004.

CHAPTER 2

BACKGROUND

2.1 Thin Film CdTe Photovoltaics

Thin film CdTe solar cells are at the heart of an increasingly important technology for solar energy production, which has had the largest share in the US of thin film module shipments since 2006. CdTe thin film modules have demonstrated their robustness via long-term stability, competitive performance, and hence continue to be attractive for production-scale capital investments. This section reviews the status of CdTe thin film solar cells, with emphasis on the properties that make CdTe a favorable material for use in photovoltaics for terrestrial applications.

Analysis of the dependence of ideal solar cell conversion efficiencies on energy bandgap (E_G) shows that CdTe is an excellent match to our sun. The direct optical bandgap of CdTe, a group II-VI semiconductor, is nearly optimally matched to the solar spectrum for photovoltaic energy conversion [1]. With a direct bandgap, E_G , of approximately 1.5 eV at room temperature, and a high coefficient of optical absorption ($>10^4 \text{ cm}^{-1}$), CdTe is capable of delivering high quantum yields from the ultraviolet down to the CdTe bandgap ($\lambda \approx 825 \text{ nm}$). The high coefficient of absorption translates to 99% absorption of AM1.5 photons above 1.5 eV in energy within a few microns of CdTe. The theoretically computed solar cell efficiencies versus the bandgap, and the optical absorption coefficient versus the energy for CdTe and other selected photovoltaic materials are compared in Figure 2.1.

Most high efficiency CdTe solar cells have a *superstrate* structure, where transparent conducting oxide (TCO) and CdS layers are grown on a transparent substrate (usually glass) followed by a CdTe film and a back contact. The alternative *substrate* configuration where the CdTe is deposited onto a conductive substrate, followed by deposition of the CdS and TCO layers, has not yet attained very high conversion efficiencies, possibly because of lower CdS/CdTe junction quality.. A cross-sectional schematic of a *superstrate* CdTe solar cell is presented in Figure 2.2.

Most CdTe solar cells employ an n-type CdS window layer adjacent to the CdTe

film. The processing possibilities for depositing a good-quality CdS layer are varied and include chemical bath deposition, sputter deposition, and other forms of physical vapor deposition. The choice of deposition process for CdS is typically driven by compatibility with the other processes in a production line. While it is desirable to keep the CdS layer as thin as possible to transmit the largest amount of short-wavelength photons (< 520 nm), thereby increasing the short wavelength quantum efficiency and hence short-circuit current, ultra-thin CdS films can potentially lead to introduction of shunt resistances that affect device performance. Numerous methods have been used to deposit the typically intrinsically p-type CdTe film. These have been reviewed in detail in the literature [2]–[5]. In the present work the CdTe films in the solar cell samples have been grown using close-spaced sublimation (CSS) and rf-sputtering. A CSS-like process is thought to be used in manufacture of the most common commercial CdTe modules. A brief description of these two processes is provided next.

CSS: To evaporate CdTe films onto substrates at temperatures above 400°C , re-evaporation of Cd and Te from the growing CdTe surface is a significant problem. This can be mitigated by depositing at higher total pressures, $\sim(1\text{--}10)$ Torr. At higher pressures the mass transfer from the source to the substrate becomes diffusion-limited, so the source and substrate are brought into close proximity. For CSS, the CdTe source material is supported in a holder having a similar surface area as the substrate. A thermally-insulating spacer enables thermal isolation of the source and the substrate so that a temperature differential can be sustained throughout the process. The deposition is typically done in an ambient of nonreactive gas such as N_2 , Ar, or He. As-deposited CSS films deposited above 550°C exhibit nearly random orientation and a normal grain size distribution with a mean grain size that is comparable to film thickness. The CSS process can also achieve growth rates $>1\text{ }\mu\text{m}/\text{min}$. A schematic of CSS growth process for CdTe is presented in Figure 2.3 (a).

Rf-sputtering: CdTe films have also been deposited by radio-frequency (rf) magnetron sputtering from compound targets, typically by Ar. Mass transfer of Cd and Te occurs via ablation of the CdTe target by Ar^+ ions and is followed by their diffusion to the substrate and condensation. Typically, sputter deposition is carried out at a substrate

temperature less than 300° C and at pressures of ~10 mTorr. The CdTe films, 2-μm-thick, deposited at ~200° C exhibit a mean grain diameter of ~300 nm and nearly random orientation. A schematic of rf-sputtering process for CdTe growth is presented in Figure 2.3 (b).

2.2 CdCl₂ Anneal Treatment for CdTe Photovoltaics

It has been empirically shown that the growth process for CdTe is less critical than the post-deposition processing of the films in order to achieve high-efficiency solar cells, although process does matter somewhat. The most important post-deposition processing step involves exposing the CdS/CdTe structure to CdCl₂ at elevated temperature. This process is often referred as “CdCl₂ annealing”. It is typically done at 350° – 450°C for 15-30 mins, depending on the thickness of the CdTe film. The treatment leads to improved open circuit voltage, short circuit current, and fill factor [6], [7]. Atomic force microscopy, scanning electron microscopy, x-ray diffraction, and time-resolved photoluminescence measurements [7]–[9] have demonstrated that CdCl₂ annealing induces recrystallization of the CdTe films and promotes grain growth, which lead to enhanced minority carrier lifetimes. In addition, CdCl₂ annealing introduces Cl into the CdTe film, which has significant effects on the electronic properties of CdTe and on the finished device performance.

2.3 Photoluminescence Spectroscopy of CdTe

CdTe has been a technologically relevant material not only for its applications in the photovoltaic industry but also because its alloys are used in x-ray, gamma ray, and infra-red detectors[10], [11]. Hence, there is a large body of literature devoted to investigating the electronic and optical properties of CdTe crystals. Despite this rich literature, spectroscopic characterization of photovoltaic device quality CdTe films is limited. This section will present an overview of the work that has been done to analyze the optical properties, and electronic band structure and the defect levels of CdTe films for photovoltaic applications using photoluminescence (PL) spectroscopy.

PL is a technique to probe states in the energy gap of semiconductors and hence

to study the possible carrier trapping and recombination routes. PL involves exciting electrons in a semiconductor by illumination with a laser of energy higher than the band gap. The photo-excited carriers relax to their ground states by radiative or non-radiative processes. The radiative transitions are accompanied by emission of photons. These are collected and analyzed. The dependence of the luminescence intensity and energy distribution on the incident laser intensity, wavelength, and sample temperature, one can predict the types of states involved in the emissive transitions [12].

Okamoto et al. found emission bands that were proposed to result from cadmium vacancy (V_{Cd})-Cl defect complexes and neutral acceptor bound excitons due to Cu in finished solar cell samples [13], [14]. Cu is introduced, usually as a component of the back contact, and acts to enhance p-type doping of the CdTe and improve the ohmic behavior of back contacts [15]. Vatavu et al. have investigated the effect of Cu and O incorporation on the luminescence properties of CdS/CdTe junctions [16]. Taguchi et al. investigated the band-edge and donor-acceptor transitions in single crystal CdTe [17]. A comparison of PL emissions from single crystal and polycrystalline CdTe is presented in Ref. [18]. Still, unambiguous assignment of various peaks observed in the PL spectra of these films and devices remains challenging. Due to the presence of various recombination centers in the polycrystalline material, the emission lines are broadened and overlap, which makes their accurate identification difficult. However, it can be concluded from these investigations that the optical (and electronic) properties of CdS/CdTe heterojunction devices are affected by various defect-mediated recombinations that are responsible for reducing the effective charge separation. These defect states have been attributed to V_{Cd} [13], complexes consisting of V_{Cd} and donor impurities such as Cl ($V_{Cd}-Cl_{Te}$) [19], Cu on Cd sites (Cu_{Cd}) [16] and donor-acceptor (DA) complexes [17].

2.4 Micro-scale Electronic Properties of CdTe

Measurements of single grain boundary properties on a real device structure after all the device-processing treatments provide technologically relevant information than analyses on model systems. Studies of real devices requires mapping the electronic properties at a spatial resolution better than ~ 100 nm. Electron beam induced current

(EBIC) has been used to map the nanoscale current collection efficiency of polycrystalline CdTe films [20]–[23]. After the CdCl₂ treatment and Cu introduction the current collection efficiency of the CdTe films was shown to be greatly enhanced, particularly along the grain boundaries [20], [21]. Scanning capacitance microscopy (SCM) has been used to demonstrate the existence of a carrier depleted/compensated p-doped region along the grain boundaries in CdTe [24]–[26]. Scanning Kelvin probe microscopy (SKPM) has also been used to determine that the local surface work function of the CdTe film is slightly lower along the grain boundaries than for the grain bulk because of the reduced hole density along the grain boundaries [25]. Finally, optical beam induced current (OBIC) has been utilized to investigate the electronic properties of CdTe films [23], [27], [28]. In the recent years several theoretical studies have also focused on analyzing the properties of single grain boundaries in CdTe [21], [29], [30]. For a review of the recent progresses on characterization of grain boundaries in CdTe the readers are directed to [31].

Although the works mentioned above have all investigated polycrystalline CdTe films, they have arrived at a variety of conclusions. Some studies show that the presence of Cl, an n-dopant for CdTe causes local doping along grain boundary areas (type inversion and carrier depletion) and results in p-doped CdTe grains separated by n-type or depleted p-type grain boundaries [21], [24], [26]. Another set of studies describe a stronger p-doping immediately next to the grain boundaries based on in-plane electrical characterization of the front (interface with CdS) surface of “lift-off” CdTe films [32], [33]. This results in an energy barrier to the flow of minority carriers just before the grain boundary. A third model supports the existence of enhanced p-doping at the grain boundaries as compared to the grain bulk by using EBIC and OBIC measurements [22], [23]. In these results the resulting upward band bending at the grain/grain-boundary interface effectively acts as an electron reflector. A summary of these reports is presented in Figure 2.4, where various proposed energy band diagrams from each of these reports are provided.

This lack of consensus is a result of two factors. There are the inherent resolution limitations of some of these experimental methods. EBIC and OBIC are great techniques

for measuring local minority carrier current collection from materials but suffer from electron scattering, secondary electron generation, carrier diffusion, and optical diffraction limitations. Thus, it is likely that the EBIC and OBIC responses measured a combination of grain and grain boundary properties. SKPM is a well-established technique for measuring local work functions of samples but is extremely sensitive to surface topography (as in the polycrystalline CdTe films), which induces measurement artifacts that need to be accounted and corrected for [34], [35]. SCM is a powerful technique to measure relative carrier concentrations in semiconductors but it has not been extensively used for characterizing CdTe solar cells, presumably due to poor signal and topography problems. The second concern is variation of sample behaviors for materials grown using different methods and subjected to varied treatments. I am not aware of comparative studies of samples grown by different methods and as a function of various device-processing steps.

2.5 Near-Field Microscopy and Microwave Microscopy

Reliable characterization of nanoscale electronic properties is possible through near-field microwave microscopy, an emerging technique that has attracted considerable interest in the last decade. Most microscopy techniques rely on interaction of matter with electromagnetic fields in the far field. Such measurements are resolution limited due to the Rayleigh diffraction limit or Abbe barrier, which instructs that $\Delta x = \lambda/2(NA)$, where Δx is the spatial resolution, λ is the wavelength of the radiation, and NA is the numerical aperture of the lens used. This limits the resolution to 400-800 nm for visible light. This is overcome by using near-field microscopy, where the radiation source or detector or both are placed close to the object (with respect to the wavelength of the radiation being used). The resolution limitation in this case is determined by the size of the detector or the source, which is smaller than the wavelength of the radiation, and can be smaller than the diffraction limit [36]–[39].

Microwave microscopy is a sub-field of near-field microscopy, which employs microwaves for imaging. There are several advantages of choosing microscope frequencies in the microwave regime. For example, the near field response at this

frequency is particularly sensitive to the electron density and dielectric properties of the sample. These can be de-convoluted from the reflected power in a tuned microwave transmission line where the tuning is modified by the microwave interaction with the sample in the near field. The initial demonstration of sub-wavelength resolution microscopy at microwave wavelengths was conducted by Ash et al. [40]. A longer history for microwave microscopy can be found in Kalinin and Gruverman [41]. As with other near-field microscopes, microwave microscopes consist of a small antenna with diameter, $D, < \lambda$. A microwave microscope consists of the scanning microwave probe (the antenna), a scanning platform, a mechanism to bring the antenna in close proximity to the sample, and microwave electronics to detect the response signal. Hence, it is advantageous to implement the microwave microscope on a conventional SPM.

Since the length scales of interaction, determined by the probe size, are much smaller than the wavelength of the radiation ($\lambda = 10$ cm at 3 GHz), one can represent the interaction using an equivalent circuit without the need for keeping track of the spatially dependent terms. The reflected signal for microwave microscopy can be defined as:

$$S_{11} = (Z_L - Z_o)/(Z_L + Z_o) \quad (2.1)$$

where Z_o is the characteristic impedance of the microwave transmission line, 50 Ω . Z_L is the load impedance and is related to the tip-sample interaction impedance. This in turn depends on the complex dielectric response of the materials being analyzed. The microwaves interact with the sample in a classical manner, owing to low energy of microwave radiations (1.2×10^{-5} eV at 3 GHz), and thus cannot excite inter-band transitions. This simplifies the data interpretation. Since the microwaves capacitively couple with the sample, there is little or no need for sample preparation and the results are not strongly dependent on the surface chemistry, as opposed to other techniques such as conductive AFM and SKPM. Microwave microscopy measures properties resulting from the collective response of electrons in the materials, and is different from scanning tunneling microscopy that measures the local density of states with atomic resolution.

2.6 Scanning Microwave Impedance Microscopy

Scanning microwave impedance microscopy (sMIM) is a specialized form of microwave microscopy. As is shown in Figure 2.5, when the MIM probe scans the sample and encounters variations in electronic properties, the changes in the tip-sample interaction, ΔZ_{tip} , are detected by the MIM electronics. A detailed description of MIM electronics can be found in [42]–[44]. Two orthogonal MIM outputs are proportional to the real and imaginary sample admittance, $(\Delta Z_{\text{tip}})^{-1}$, therefore this technique is called Microwave Impedance Microscopy. These two outputs relate to the resistive and capacitive interactions between the tip and the sample. The spatial resolution is dependent on the antenna or tip size (R) and on the skin depth in the sample. The electric field of the microwaves can penetrate farther into materials with lower ϵ and hence the spatial resolution (Δx) is poorer ($\Delta x > R$). The signal and the resolution also depend on the tip-sample contact area as greater contact area correlates to greater capacitance.

2.7 Conductive Atomic Force Microscopy

Conductive atomic force microscopy (C-AFM) measures current variations from femto- to microamps as a conductive probe is scanned in contact mode across a sample. For a given tip-sample bias voltage the resistance of the sample can be determined with variations on a scale of individual pixels in an AFM scan. C-AFM employs an AFM cantilever, which is either coated with a conductive coating or is entirely made out of a conductive material. A schematic of C-AFM instrumentation is shown in Figure 2.6. C-AFM can simultaneously map the topography and current, which enables the correlation of sample topography with electrical conductivity.

2.8 Figures

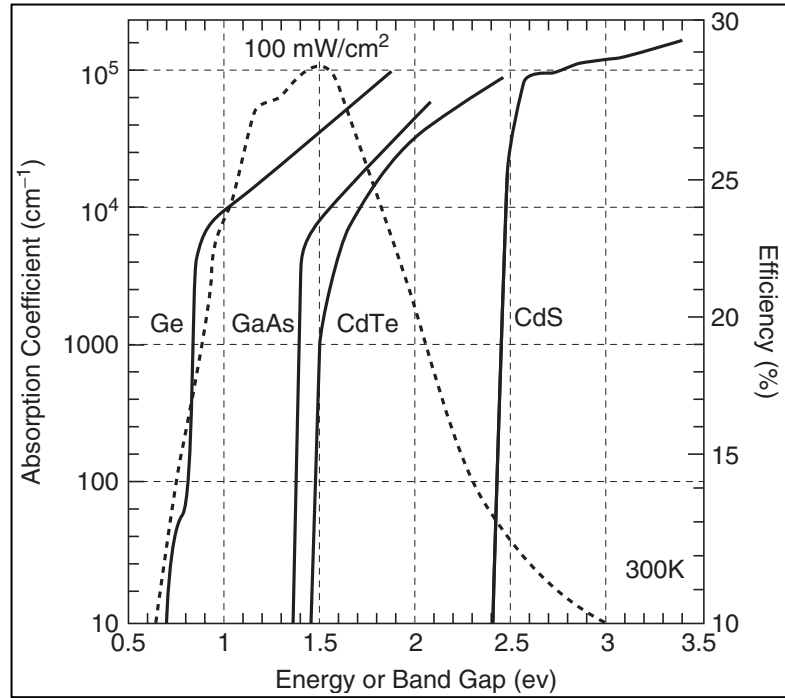


Figure 2.1: Theoretical solar cell efficiency (dotted) for AM1.5 spectral irradiance versus bandgap and absorption coefficient (solid) versus energy for various semiconductor materials. Image taken, with permission, from [45].

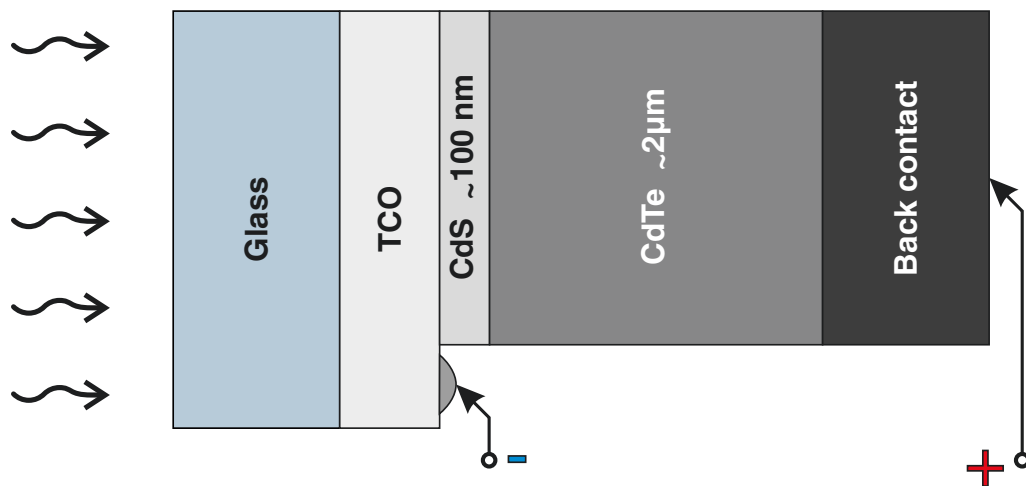


Figure 2.2: A schematic of a CdTe solar cell in the *superstrate* configuration. Image taken, with permission, from [46].

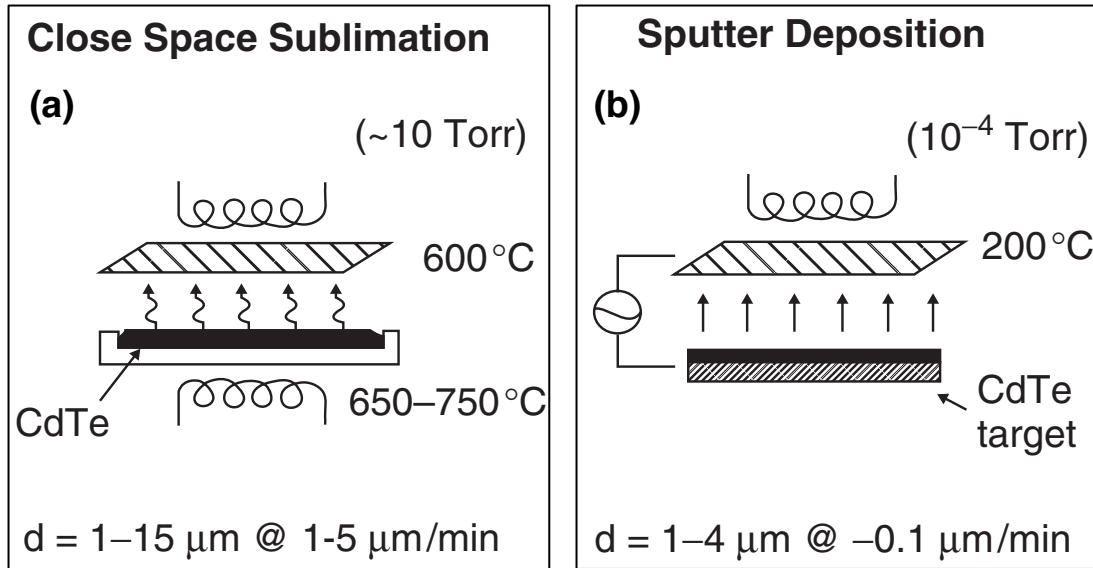


Figure 2.3: Schematic of (a) Close-Spaced Sublimation, and (b) rf-sputtering processes for growth of CdTe. Image taken, with permission, from [45].

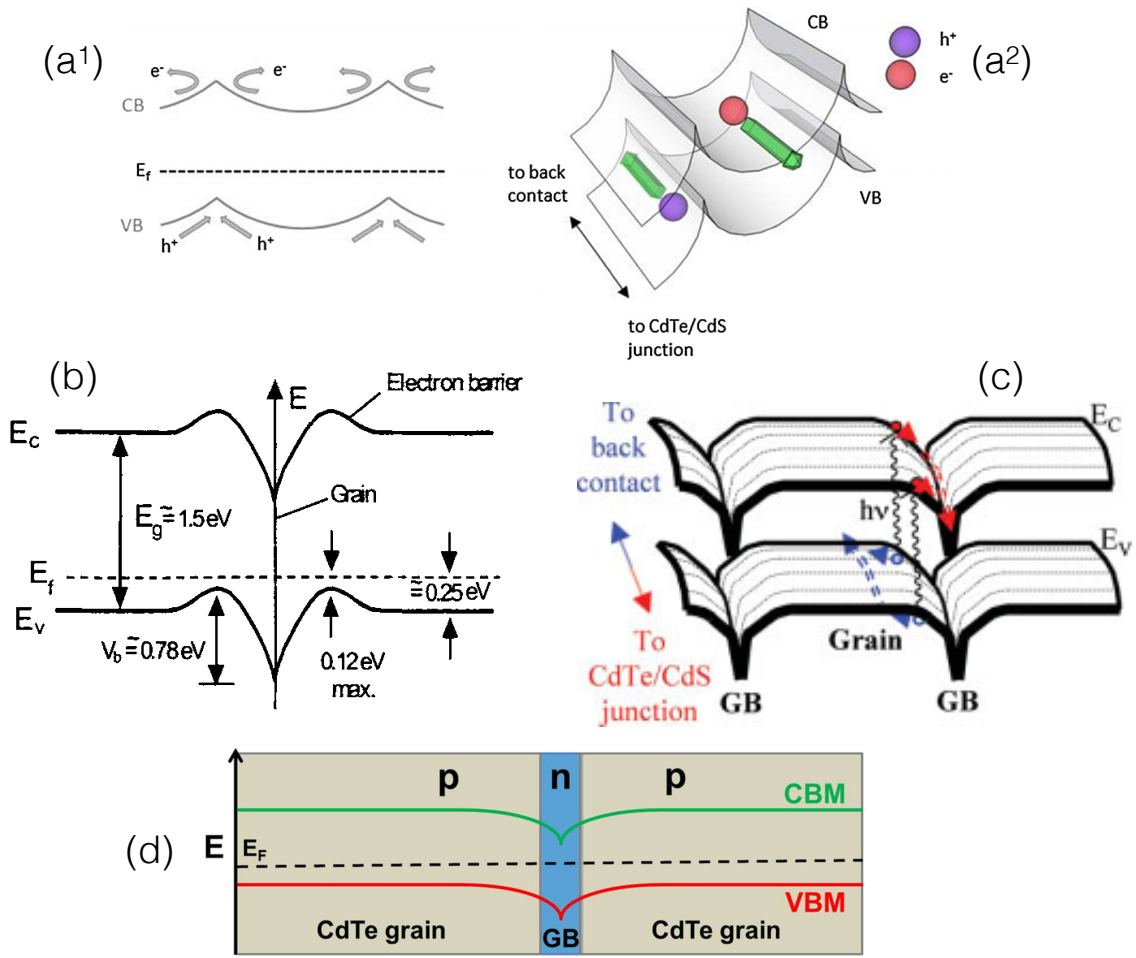


Figure 2.4: Various predicted grain boundary band bending models showing (a¹), (a²) grain boundary p-carrier accumulation, (b) near boundary p-carrier accumulation, (c) grain boundary p-carrier depletion, and (d) grain boundary carrier-type inversion. Images taken, with permission, from [21], [24], [33], [47].

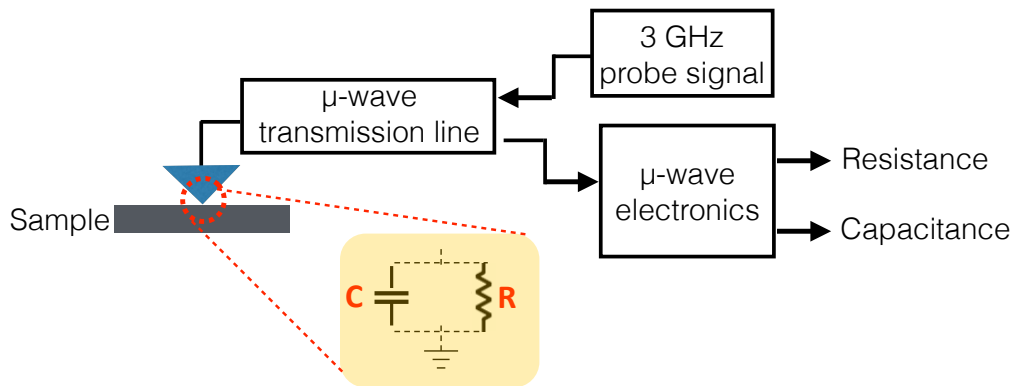


Figure 2.5: A cartoon schematic of MIM and its various parts along with a lumped circuit model.

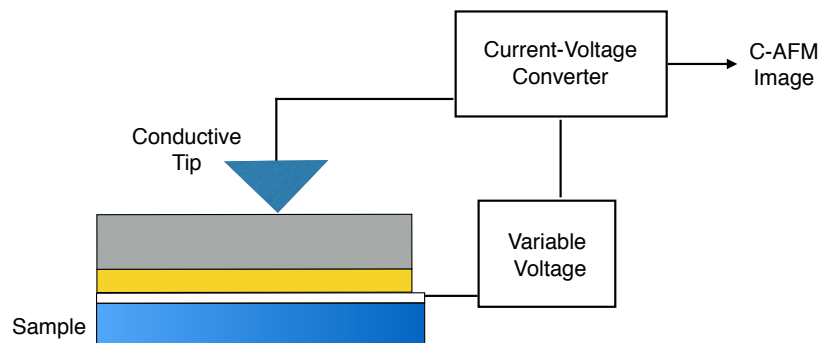


Figure 2.6: Schematic of a Conductive atomic force microscopy (C-AFM) setup.

2.9 References

- [1] J. J. Loferski, "Theoretical Considerations Governing the Choice of the Optimum Semiconductor for Photovoltaic Solar Energy Conversion," *J. Appl. Phys.*, vol. 27, no. 7, pp. 777–784, Jul. 1956.
- [2] D. BONNET, "THE CdTe THIN FILM SOLAR CELL - AN OVERVIEW," *Int. J. Sol. Energy*, vol. 12, no. 1–4, pp. 1–14, Jan. 1992.
- [3] T. L. Chu and S. S. Chu, "Recent progress in thin-film cadmium telluride solar cells," *Prog. Photovolt. Res. Appl.*, vol. 1, no. 1, pp. 31–42, Jan. 1993.
- [4] R. W. Birkmire and E. Eser, "POLYCRYSTALLINE THIN FILM SOLAR CELLS: Present Status and Future Potential," *Annu. Rev. Mater. Sci.*, vol. 27, no. 1, pp. 625–653, 1997.
- [5] D. Bonnet and P. Meyers, "Cadmium-telluride—Material for thin film solar cells," *J. Mater. Res.*, vol. 13, no. 10, pp. 2740–2753, Oct. 1998.
- [6] C. S. Ferekides, U. Balasubramanian, R. Mamazza, V. Viswanathan, H. Zhao, and D. L. Morel, "CdTe thin film solar cells: device and technology issues," *Sol. Energy*, vol. 77, no. 6, pp. 823–830, Dec. 2004.
- [7] B. E. McCandless, I. Youm, and R. W. Birkmire, "Optimization of vapor post-deposition processing for evaporated CdS/CdTe solar cells," *Prog. Photovolt. Res. Appl.*, vol. 7, no. 1, pp. 21–30, Jan. 1999.
- [8] H. R. Moutinho, M. M. Al-Jassim, D. H. Levi, P. C. Dippo, and L. L. Kazmerski, "Effects of CdCl₂ treatment on the recrystallization and electro-optical properties of CdTe thin films," *J. Vac. Sci. Technol. A*, vol. 16, no. 3, pp. 1251–1257, May 1998.
- [9] H. R. Moutinho, F. S. Hasoon, F. Abulfotuh, and L. L. Kazmerski, "Investigation of polycrystalline CdTe thin films deposited by physical vapor deposition, close-spaced sublimation, and sputtering," *J. Vac. Sci. Technol. A*, vol. 13, no. 6, pp. 2877–2883, Nov. 1995.
- [10] Y. Eisen and A. Shor, "CdTe and CdZnTe materials for room-temperature X-ray and gamma ray detectors," *J. Cryst. Growth*, vol. 184, pp. 1302–1312, Feb. 1998.
- [11] A. Rogalski, "HgCdTe infrared detector material: history, status and outlook," *Rep. Prog. Phys.*, vol. 68, no. 10, p. 2267, 2005.

- [12] N. C. Giles-Taylor, R. N. Bicknell, D. K. Blanks, T. H. Myers, and J. F. Schetzina, "Photoluminescence of CdTe: A comparison of bulk and epitaxial material," *J. Vac. Sci. Technol. A*, vol. 3, no. 1, pp. 76–82, Jan. 1985.
- [13] T. Okamoto, A. Yamada, and M. Konagai, "Optical and electrical characterizations of highly efficient CdTe thin film solar cells," *Thin Solid Films*, vol. 387, no. 1–2, pp. 6–10, May 2001.
- [14] T. Okamoto, A. Yamada, and M. Konagai, "Optical and electrical characterizations of highly efficient CdTe thin film solar cells prepared by close-spaced sublimation," *J. Cryst. Growth*, vol. 214–215, pp. 1148–1151, Jun. 2000.
- [15] H. C. Chou, A. Rohatgi, E. W. Thomas, S. Kamra, and A. K. Bhat, "Effects of Cu on CdTe / CdS Heterojunction Solar Cells with Au/Cu Contacts," *J. Electrochem. Soc.*, vol. 142, no. 1, pp. 254–259, Jan. 1995.
- [16] S. Vataavu, H. Zhao, I. Caraman, P. Gaşin, and C. Ferekides, "The copper influence on the PL spectra of CdTe thin film as a component of the CdS/CdTe heterojunction," *Thin Solid Films*, vol. 517, no. 7, pp. 2195–2201, Feb. 2009.
- [17] T. Taguchi, J. Shirafuji, and Y. Inuishi, "Edge and Donor-Acceptor Pair Emissions in Cadmium Telluride," *Jpn. J. Appl. Phys.*, vol. 12, no. 10, pp. 1558–1566, 1973.
- [18] D. Grecu and A. D. Compaan, "Photoluminescence study of Cu diffusion and electromigration in CdTe," *Appl. Phys. Lett.*, vol. 75, no. 3, pp. 361–363, Jul. 1999.
- [19] D. . Halliday, J. . Eggleston, and K. Durose, "A photoluminescence study of polycrystalline thin-film CdTe/CdS solar cells," *J. Cryst. Growth*, vol. 186, no. 4, pp. 543–549, Mar. 1998.
- [20] J. D. Poplawsky *et al.*, "Direct Imaging of Cl- and Cu-Induced Short-Circuit Efficiency Changes in CdTe Solar Cells," *Adv. Energy Mater.*, vol. 4, no. 15, p. 1400454, Oct. 2014.
- [21] C. Li *et al.*, "Grain-Boundary-Enhanced Carrier Collection in CdTe Solar Cells," *Phys. Rev. Lett.*, vol. 112, no. 15, p. 156103, Apr. 2014.
- [22] P. R. Edwards, S. A. Galloway, and K. Durose, "EBIC and luminescence mapping of CdTe/CdS solar cells," *Thin Solid Films*, vol. 361–362, pp. 364–370, Feb. 2000.

- [23] S. A. Galloway, P. R. Edwards, and K. Durose, "Characterisation of thin film CdS/CdTe solar cells using electron and optical beam induced current," *Sol. Energy Mater. Sol. Cells*, vol. 57, no. 1, pp. 61–74, Feb. 1999.
- [24] I. Visoly-Fisher, S. R. Cohen, A. Ruzin, and D. Cahen, "How Polycrystalline Devices Can Outperform Single-Crystal Ones: Thin Film CdTe/CdS Solar Cells," *Adv. Mater.*, vol. 16, no. 11, pp. 879–883, Jun. 2004.
- [25] I. Visoly-Fisher, S. R. Cohen, and D. Cahen, "Direct evidence for grain-boundary depletion in polycrystalline CdTe from nanoscale-resolved measurements," *Appl. Phys. Lett.*, vol. 82, no. 4, pp. 556–558, Jan. 2003.
- [26] I. Visoly-Fisher, S. R. Cohen, K. Gartsman, A. Ruzin, and D. Cahen, "Understanding the Beneficial Role of Grain Boundaries in Polycrystalline Solar Cells from Single-Grain-Boundary Scanning Probe Microscopy," *Adv. Funct. Mater.*, vol. 16, no. 5, pp. 649–660, Mar. 2006.
- [27] S. Smith, P. Zhang, T. Gessert, and A. Mascarenhas, "Near-field optical beam-induced currents in CdTe/CdS solar cells: Direct measurement of enhanced photoresponse at grain boundaries," *Appl. Phys. Lett.*, vol. 85, no. 17, pp. 3854–3856, Oct. 2004.
- [28] M. S. Leite, M. Abashin, H. J. Lezec, A. Gianfrancesco, A. A. Talin, and N. B. Zhitenev, "Nanoscale Imaging of Photocurrent and Efficiency in CdTe Solar Cells," *ACS Nano*, vol. 8, no. 11, pp. 11883–11890, Nov. 2014.
- [29] L. Zhang, J. L. F. Da Silva, J. Li, Y. Yan, T. A. Gessert, and S.-H. Wei, "Effect of Copassivation of Cl and Cu on CdTe Grain Boundaries," *Phys. Rev. Lett.*, vol. 101, no. 15, p. 155501, Oct. 2008.
- [30] Y. Yan *et al.*, "Physics of grain boundaries in polycrystalline photovoltaic semiconductors," *J. Appl. Phys.*, vol. 117, no. 11, p. 112807, Mar. 2015.
- [31] J. D. Major, "Grain boundaries in CdTe thin film solar cells: a review," *Semicond. Sci. Technol.*, vol. 31, no. 9, p. 93001, 2016.
- [32] L. M. Woods, G. Y. Robinson, and D. H. Levi, "The effects of CdCl₂ on CdTe electrical properties using a new theory for grain-boundary conduction," in *Conference Record of the Twenty-Eighth IEEE Photovoltaic Specialists Conference, 2000*, 2000, pp. 603–606.

- [33] L. M. Woods, D. H. Levi, V. Kaydanov, G. Y. Robinson, and R. K. Ahrenkiel, "Electrical characterization of etched grain-boundary properties from as-processed px-CdTe-based solar cells," in *AIP Conference Proceedings*, 1999, vol. 462, pp. 499–504.
- [34] A. Efimov and S. R. Cohen, "Simulation and correction of geometric distortions in scanning Kelvin probe microscopy," *J. Vac. Sci. Technol. A*, vol. 18, no. 4, pp. 1051–1055, Jul. 2000.
- [35] S. Barbet, M. Popoff, H. Diesinger, D. Deresmes, D. Théron, and T. Mélin, "Cross-talk artefacts in Kelvin probe force microscopy imaging: A comprehensive study," *J. Appl. Phys.*, vol. 115, no. 14, p. 144313, Apr. 2014.
- [36] E. Betzig, "Principles and Applications of Near-Field Scanning Optical Microscopy (NSOM)," in *Near Field Optics*, D. W. Pohl and D. Courjon, Eds. Springer Netherlands, 1993, pp. 7–15.
- [37] D. W. Pohl, "Some Remarks on the History of Near-Field Optics," in *Near Field Optics*, D. W. Pohl and D. Courjon, Eds. Springer Netherlands, 1993, pp. 1–5.
- [38] "History of Near-field Optics," in *Near-Field Microscopy and Near-Field Optics*, PUBLISHED BY IMPERIAL COLLEGE PRESS AND DISTRIBUTED BY WORLD SCIENTIFIC PUBLISHING CO., 2003, pp. 1–15.
- [39] D. Courjon, *Near-Field Microscopy and Near-Field Optics*. PUBLISHED BY IMPERIAL COLLEGE PRESS AND DISTRIBUTED BY WORLD SCIENTIFIC PUBLISHING CO., 2003.
- [40] E. A. Ash and G. Nicholls, "Super-resolution Aperture Scanning Microscope," *Nature*, vol. 237, no. 5357, pp. 510–512, Jun. 1972.
- [41] S. V. Kalinin and A. Gruverman, *Scanning Probe Microscopy: Electrical and Electromechanical Phenomena at the Nanoscale*. Springer Science & Business Media, 2007.
- [42] K. Lai, W. Kundhikanjana, M. A. Kelly, and Z.-X. Shen, "Nanoscale microwave microscopy using shielded cantilever probes," *Appl. Nanosci.*, vol. 1, no. 1, pp. 13–18, May 2011.

- [43] K. Lai, W. Kundhikanjana, M. Kelly, and Z. X. Shen, "Modeling and characterization of a cantilever-based near-field scanning microwave impedance microscope," *Rev. Sci. Instrum.*, vol. 79, no. 6, p. 63703, Jun. 2008.
- [44] W. Kundhikanjana, *Imaging nanoscale electronic inhomogeneity with microwave impedance microscopy*. 2013.
- [45] B. E. McCandless and J. R. Sites, "Cadmium Telluride Solar Cells," in *Handbook of Photovoltaic Science and Engineering*, A. Luque and S. Hegedus, Eds. John Wiley & Sons, Ltd, 2011, pp. 600–641.
- [46] M. Bokalič and M. Topič, "CdTe Solar Cells," in *Spatially Resolved Characterization in Thin-Film Photovoltaics*, Springer International Publishing, 2015, pp. 53–65.
- [47] W. S. M. Brooks, S. J. C. Irvine, and D. M. Taylor, "Scanning Kelvin probe measurements on As-doped CdTe solar cells," *Semicond. Sci. Technol.*, vol. 28, no. 10, p. 105024, 2013.

CHAPTER 3

EXPERIMENTAL METHODS

3.1 CdTe Solar Cell Fabrication

The polycrystalline CdTe films used in the present work were grown using radio frequency sputtering (rf-sputtering) and close spaced sublimation (CSS) processes. These processes have been described in some detail in Section 2.1. The specifics of the growth parameters are described below:

Rf-sputtering: These samples were grown at the University of Toledo on NSG-Pilkington TEC-15 glass substrates, which are soda lime glass coated with a tri-layer of $\text{SnO}_2/\text{SiO}_2/\text{SnO}_2:\text{F}$. The CdS and CdTe were sequentially deposited on these substrates by magnetron sputtering at a substrate temperature of 250°C , an rf power of 200 W, and an Ar pressure of 15/10 mTorr for CdS/CdTe depositions. The CdS and CdTe thicknesses are 120 nm and 2200 nm, respectively, as monitored *in-situ* using real time spectroscopic ellipsometry. Following this process some samples were removed from the fabrication line in order to investigate the properties of the as-deposited CdTe films (see Chapter 5). Next, some samples were subjected to the CdCl_2 anneal treatment by applying a saturated aqueous solution of CdCl_2 to the CdTe film surface and by annealing in dry air for 30 min at 387°C . Another set of samples was removed from the fabrication line at this step in order to study the properties of the CdTe film and CdTe/CdS junction after the CdCl_2 treatment (see Chapters 4 and 5). The remaining samples were further over-deposited by Cu/Au bilayer contacts of 3/30 nm thicknesses and subsequently annealed at 150°C in air for 45 min. These samples were used to study the effect of Cu incorporation on the CdS/CdTe junction luminescence properties (see Chapter 4). Additional details of the deposition process may be found in the references [1], [2]; however, some growth and device processing parameters have been adjusted as described here. These samples have an area of 1 cm x 1 cm. The completed device (after CdCl_2 anneal and Cu/Au deposition) used for this study has an open circuit voltage (V_{OC}) of $\sim 0.8\text{ V}$, a short circuit current (J_{SC}) of $\sim 22\text{ mA/cm}^2$, and an efficiency of $\sim 12\%-13\%$. Higher efficiencies up to 14% have been achieved with this process using optimized ZnO:Al coated glass substrates [3].

CSS: The CSS grown samples were fabricated on Corning EagleXG glass at the University of South Florida. Indium tin oxide deposited by sputtering was used as the transparent conducting oxide (TCO) front contact. CdS and CdTe were then deposited by chemical bath deposition and CSS, respectively. During CSS growth, the substrate temperatures were in the range of 550-600°C and source temperatures in the 650-680°C range. A set of samples were taken out at this stage and the others were subjected to CdCl₂ deposition by evaporation followed by annealing in He and O₂ ambient (20% partial pressure of O₂) at 400°C for 30 min. These two sets of samples were used to study the effects of the CdCl₂ anneal treatment on the microstructural electronic properties of CdTe films (see Chapter 5). Additional details of the growth process can be found in Ref. [4]. Devices fabricated using this process (after CdCl₂ annealing and back contact deposition) regularly exhibit $V_{oc} \sim (0.80-0.85) \text{ mV}$, $J_{sc} \sim (20-23) \text{ mA/cm}^2$, fill factor $\sim (70-75)\%$ and efficiency $\sim (11-15)\%$.

3.2 Photoluminescence Spectroscopy

The Photoluminescence (PL) studies were carried out at the University of Illinois. A schematic of the extended PL setup in the Laser and Spectroscopy Facility at the University of Illinois is shown in Figure 3.1. The samples were mounted on a temperature-controlled vacuum cryostage and illuminated using a 532 nm Nd:YAG laser with a peak power of less than 50 mW. The maximum average power delivered to the sample was $\sim 11 \text{ mW}$. The laser spot size was 0.2 mm^2 in area, corresponding to a power density of 5.5 W/cm^2 . For this wavelength an estimated $\sim 6\%$ of the intensity was absorbed in the CdS for measurements through the glass side of the sample and 50% of the intensity was absorbed in the CdTe in the first 100 nm of the material based on absorption coefficients published in [5], ignoring the grading of the heterojunction. The excitation power was varied using an adjustable neutral density filter. A Princeton Instruments grating-based monochromator (Spectra-Pro 300i) coupled with a Si CCD detector (PIXIS 100) was used for signal detection. The luminescence spectra were corrected to account for any spectral dependence of the collection setup in the range of the measurement wavelengths. The instrumental response curve used for this correction was determined using a calibrated light source from Labsphere, Inc. The sample was

cooled to 82 K in a Kadel Engineering Corp. dewar and reheated using a resistive heater. The typical range of measurement temperatures was 82–295 K, regulated using a LakeShore cryotronics 330 autotune temperature controller. PL spectra were obtained by exciting the sample from the glass side to probe the CdS/CdTe junction for two samples (with and without the Cu-containing back contact) and from the CdTe surface (for sample without the back contact) side to probe the CdTe film properties.

3.3 Scanning Microwave Impedance Microscopy

sMIM measurements presented here were performed using an Asylum Research MFP-3D AFM with a sMIM addition produced by Prime Nano Inc., which also supplied the micro-fabricated shielded cantilevers. The instrument uses a low power (0.1-1 mW) rf signal at ~ 3 GHz to probe sample properties. After proper calibration, using a purely capacitive (dielectric) sample made of Al_2O_3 dots on top of SiO_2/Si , the capacitive and resistive channels are isolated, mapped spatially, and displayed independently. The AFM system was housed in a lightproof enclosure such that there was no unintentional light source apart from the AFM tracking laser illuminating the sample. The AFM tracking laser wavelength is ~ 850 nm (1.45 eV), which is slightly lower in energy than the band gap of CdTe (1.45-1.53 eV, depending on film stress) [2], [4], [6], thus no appreciable number of photo-carriers were generated by that laser. Measurements were also made with the illuminator lamp (white light) switched on and shining (blanket illumination) on the surface of the CdTe film being analyzed so that the effect of light exposure on the sMIM measurements can be observed.

To avoid the problems associated with the creation of a Schottky barrier at the interface of the metal sMIM tip and the semiconductor (CdTe) sample, a thin layer (5-10 nm) of insulating oxide (Al_2O_3) was grown by atomic layer deposition on the surface of CdTe prior to sMIM analyses in order to facilitate the creation of a nanoscale metal-oxide-semiconductor (MOS) structure at the tip-sample interface to enhance the capacitive tip-sample interaction. Since the frequency of the capacitance probe signal is ~ 3 GHz, the *high frequency* capacitance-voltage behavior of the MOS structure is obtained in the sMIM capacitance channel [7], [8]. In this regime, for a p-type

semiconductor and sufficiently large positive DC tip bias the MIM capacitance (MIM-C) channel measures a lower capacitance value because of carrier depletion in the semiconductor induced by the DC bias. Under a negative tip bias, hole accumulation occurs and MIM-C channel measures a higher capacitance. For the capacitance behavior of an n-type semiconductor MIS structure under a voltage bias, the trends are reversed. There are two modes of operation of the MIM instrument that utilize the capacitance of this MOS structure to determine the local properties of the sample area being scanned by the sMIM probe. These two modes are as follows:

MIM with DC voltage bias applied to tip (Capacitance measurement)

In this mode of measurement a DC voltage bias is applied to the tip and this voltage bias creates a nanoscale depletion/accumulation region in the semiconductor sample directly below the tip. The capacitive response of the MOS structure is picked up by the MIM setup in the MIM-C. The measured capacitance response is comprised of the capacitances of the oxide and the semiconductor space charge layer connected in series. The capacitance of the MOS structure, for a given thickness of the oxide layer, depends on the carrier concentration of the semiconductor being scanned and the voltage bias applied to the tip. This information is depicted in Figure 3.2. For only a DC bias (V_{dc}) applied to the tip, the capacitance response of the sample at V_{dc} is probed. Hence, in principle, by performing multiple scans while changing V_{dc} for each scan, one can acquire a C-V map of the sample area being scanned. As shown in Figure 3.2(d) for a given oxide thickness, tip-sample contact area, and DC voltage bias applied to the sMIM tip (Gate), the capacitance response is highest for the sample with the highest carrier concentration. Alternately, for all the above quantities constant if an inhomogeneous sample is scanned then the highest capacitance will be measured from the sample area that has the highest carrier concentration. Thus, using this method (relative) carrier concentrations on a semiconductor sample can be measured at a spatial resolution chiefly determined by the tip size ($\sim 30\text{-}50$ nm). However, (as described in Chapter 5) this method is very prone to topography-related measurement artifacts caused due to changes in tip-sample contact area as the tip scans a rough sample [such as polycrystalline CdTe films with RMS roughness $\sim (100\text{-}200)$ nm as in the present case]. Since a majority of the

investigations based on sMIM have been carried out on smooth/polished samples, this method of MIM measurement has been chiefly employed in the literature [9]–[11].

Lock-in based MIM (Differential Capacitance measurement)

In order to obtain reliable data, which is free of sample topography artifacts alternate measurement schema are needed. This work presents the first report of lock-in measurement based MIM and demonstrates that this measurement is devoid of sample topography artifacts. A schematic of this measurement setup with the tip voltage signal is presented in Figure 3.3. When a combination of a low-frequency AC (ΔV) and a DC voltage bias (V_{dc}) is applied to the sMIM tip then it modulates the output capacitance response (ΔC) of the MOS structure at the frequency of the input AC bias. The amplitude of the output ΔC signal depends on the steepness of the capacitance-voltage (C-V) curve, which increases as the carrier concentration decreases, as shown in Figure 3.2(d). The phase difference between the input ΔV signal and the output ΔC signal depends on the dopant type in the semiconductor sample. By using a lock-in measurement (demodulating capacitance response at frequency of input AC bias) one can measure both the amplitude of the ΔC signal and the relative phase difference between ΔC and ΔV signals, which provide information about relative carrier concentration and dopant type of the local sample area being scanned. This process is depicted via a schematic in Figure 3.4 and a phase difference of $\sim \pi$ is expected in the lock-in phase measurement output when scanning a p-doped sample vs. n-doped sample.

Alternately, this measurement can be visualized in the following manner. For a combination of dc and ac biases applied to the tip and a lock-in measurement at the ac bias frequency, the differential capacitance (dC/dV) signal, i.e. the slope of the C-V curve around V_{dc} is probed. The magnitude of the dC/dV signal ($|dC/dV|$) resulting from a given change in tip voltage, due to the time varying ac bias, is a function of the carrier concentration of the semiconductor. The phase of the dC/dV signal (θ_c) is indicative of the type of dopant in the sample. Hence, the relative carrier concentration and type can be measured by spatially mapping the dC/dV amplitude and phase signal, respectively [8], [12]. In this configuration, our measurement is similar to *open loop* scanning capacitance

microscopy (SCM) imaging, but in SCM the bias is conventionally applied to the sample as opposed to the tip, as in our study. The shielded cantilever probe design used in sMIM also greatly reduces parasitic tip-sample coupling that leads to environmental noise pickup [13], hence yielding results superior to SCM.

3.4 Conductive Atomic Force Microscopy

Conductive-atomic force microscopy (C-AFM) measurements were performed on the surfaces of the CdTe films at the University of Illinois using an Asylum Research MFP-3D AFM with commercially available solid-Platinum cantilevers from Rocky Mountain Nanotechnology, LLC. C-AFM utilizes a conductive probe in an AFM instrument. The typical radius of curvature of the tip is 20 nm. The AFM system was housed in a lightproof enclosure such that there was no unintentional light source apart from the AFM tracking laser illuminating the sample. The AFM tracking laser wavelength is ~ 850 nm (1.45 eV), which is slightly lower in energy than the band gap of CdTe, thus no appreciable number of photo-carriers were generated by that laser.

A voltage bias was applied between the tip and the sample, and the conductive probe was rastered across the sample in contact mode. During each scan the current flowing between the tip and the sample was measured at each scan pixel, enabling generation of a nanoscale-resolution map of electrical current through the sample. In all of the experiments reported in this thesis, the tip was grounded and the voltage bias was applied to the TCO layer underlying the junction. Measurements have also been made with the illuminator lamp (white light) switched on and shining on the surface of the CdTe film being analyzed so that the effect of light exposure on the C-AFM measurements can be observed.

3.5 Figures

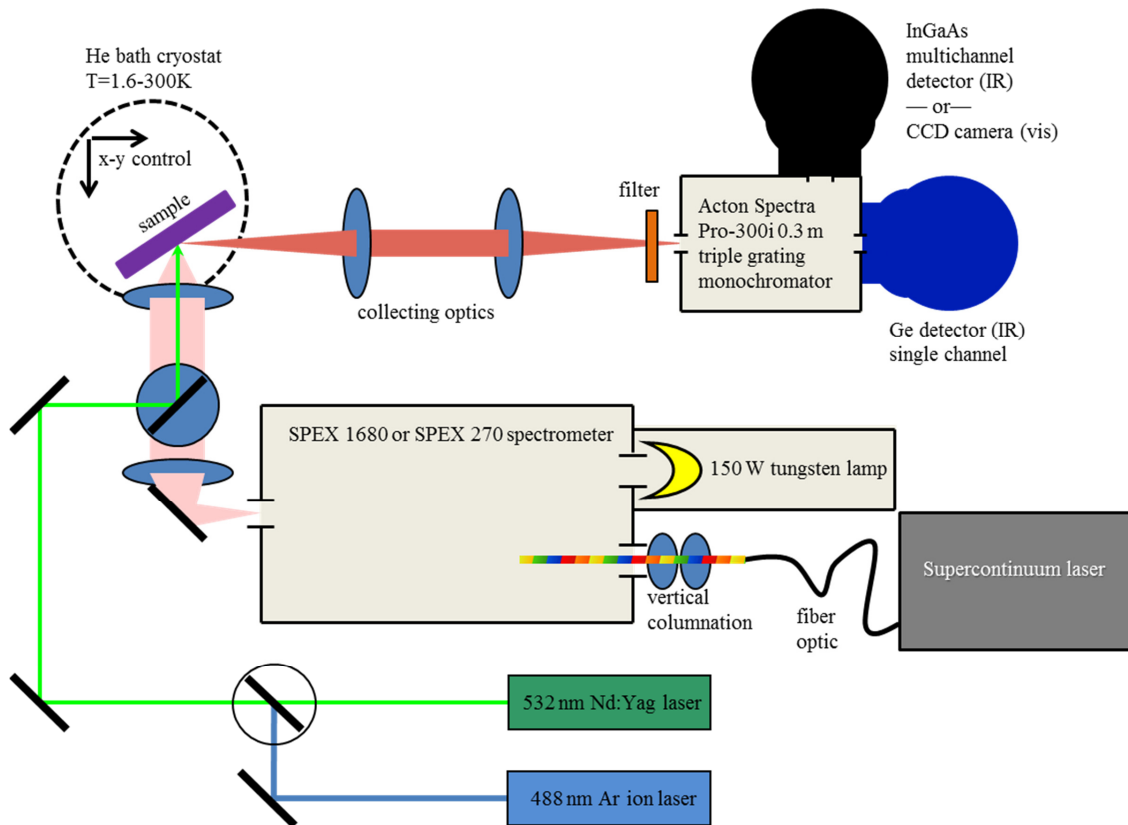


Figure 3.1: A schematic of the extended PL setup at University of Illinois. Image taken, with permission, from [14].

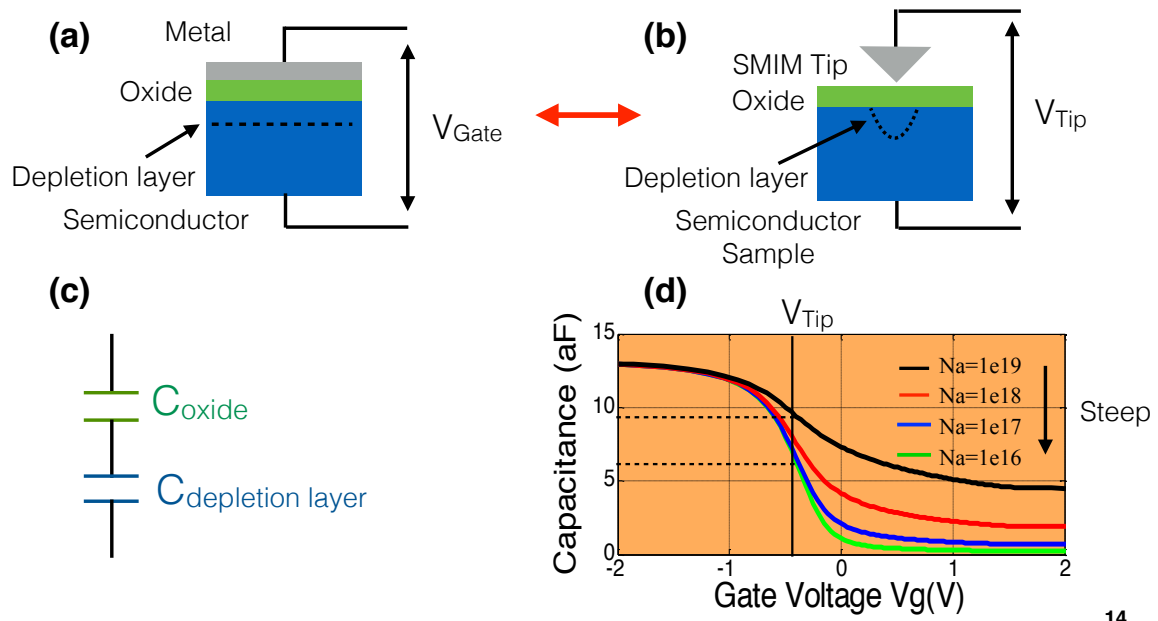


Figure 3.2: Schematic of a (a) MOS capacitor, and (b) nanoscale MOS capacitor formed by MIM probe scanning a semiconductor sample. (c) Constituent capacitances that make up the capacitance of the MOS structure, and (d) Calculated 1D MOS capacitance vs. gate voltage bias for Si sample for various acceptor-doping levels. Image (d) provided by Stuart Friedman of Prime Nano Inc.

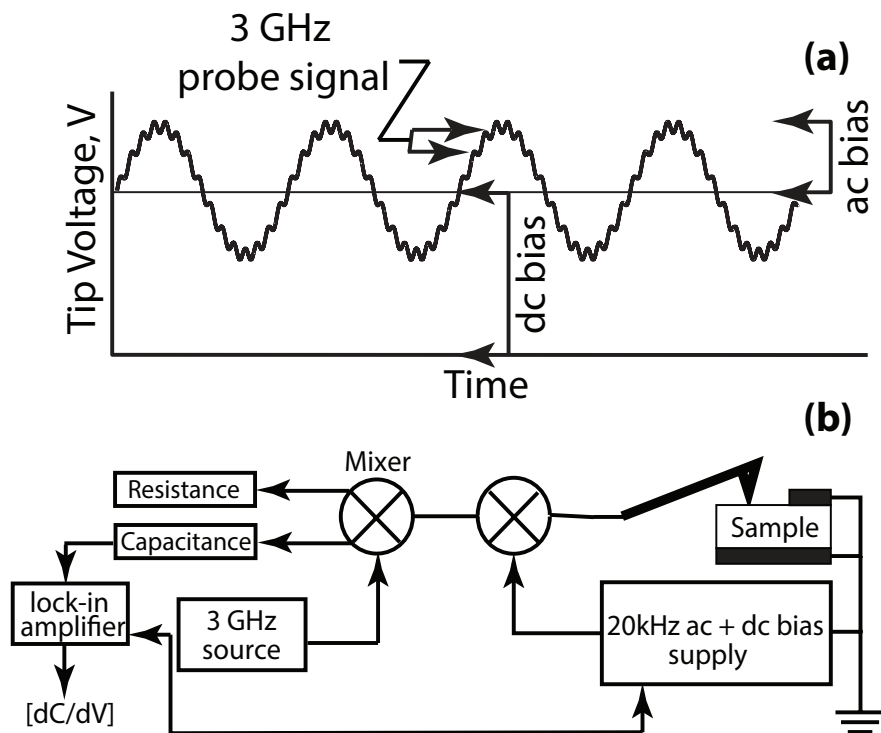


Figure 3.3: A schematic of (a) tip voltage showing the 3GHz probe signal superposed on top of a combination of DC and AC voltage biases, and (b) the experimental setup showing AC+DC bias applied to sMIM probe and a lock-in used to demodulate the output capacitance response. AC bias frequency can vary between (20-200) KHz. Image taken, with permission, from [15].

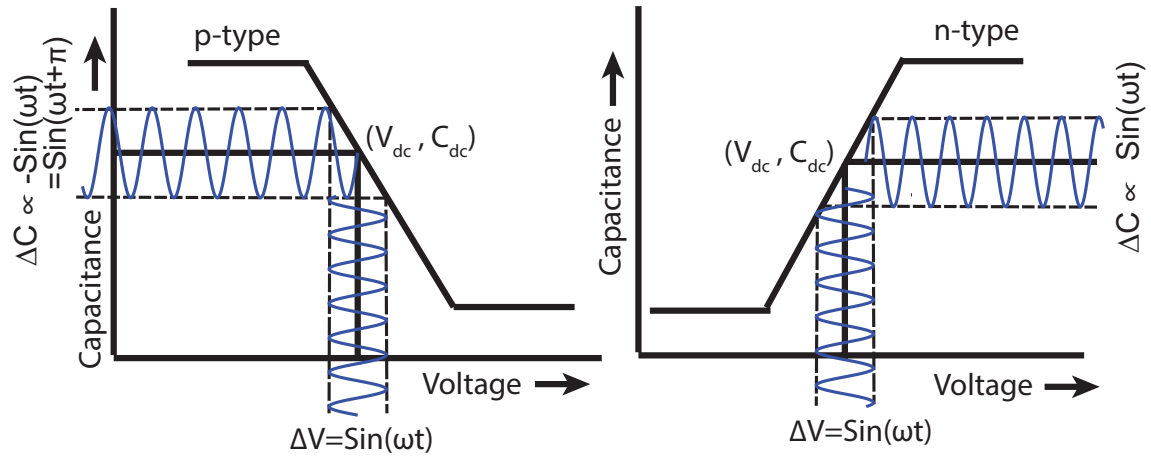


Figure 3.4: A schematic depicting the lock-in MIM measurement where a combination of AC (ΔV) and DC bias is applied to the sMIM tip. C-V curves for n-type and p-type are shown with the modulated capacitance signal (ΔC) and the resultant phase difference between the ΔC and ΔV signals and its dependence on dopant type.

3.6 References

- [1] M. Shao *et al.*, “Radio-frequency-magnetron-sputtered CdS/CdTe solar cells on soda-lime glass,” *Appl. Phys. Lett.*, vol. 69, no. 20, pp. 3045–3047, Nov. 1996.
- [2] P. Koirala *et al.*, “Mapping spectroscopic ellipsometry of CdTe solar cells for property-performance correlations,” in *Photovoltaic Specialist Conference (PVSC), 2014 IEEE 40th*, 2014, pp. 0674–0679.
- [3] A. Gupta and A. D. Compaan, “All-sputtered 14%CdS/CdTe thin-film solar cell with ZnO:Al transparent conducting oxide,” *Appl. Phys. Lett.*, vol. 85, no. 4, pp. 684–686, Jul. 2004.
- [4] C. S. Ferekides *et al.*, “High efficiency CSS CdTe solar cells,” *Thin Solid Films*, vol. 361–362, pp. 520–526, Feb. 2000.
- [5] M. A. Green, A. Ho-Baillie, and H. J. Snaith, “The emergence of perovskite solar cells,” *Nat. Photonics*, vol. 8, no. 7, pp. 506–514, Jul. 2014.
- [6] M. A. Green, “Radiative efficiency of state-of-the-art photovoltaic cells,” *Prog. Photovolt. Res. Appl.*, vol. 20, no. 4, pp. 472–476, Jun. 2012.
- [7] D. Neamen, “Semiconductor Physics and Devices,” in *Semiconductor Physics and Devices*, Fourth Edition., McGraw Hill Publisher, 2007, pp. 377–384.
- [8] C. C. Williams, “Two-Dimensional Dopant Profiling by Scanning Capacitance Microscopy,” *Annu. Rev. Mater. Sci.*, vol. 29, no. 1, pp. 471–504, 1999.
- [9] K. Lai *et al.*, “Nanoscale Electronic Inhomogeneity in In₂Se₃ Nanoribbons Revealed by Microwave Impedance Microscopy,” *Nano Lett.*, vol. 9, no. 3, pp. 1265–1269, Mar. 2009.
- [10] K. Lai, W. Kundhikanjana, M. A. Kelly, Z.-X. Shen, J. Shabani, and M. Shayegan, “Imaging of Coulomb-Driven Quantum Hall Edge States,” *Phys. Rev. Lett.*, vol. 107, no. 17, p. 176809, Oct. 2011.
- [11] W. Kundhikanjana, K. Lai, H. Wang, H. Dai, M. A. Kelly, and Z. Shen, “Hierarchy of Electronic Properties of Chemically Derived and Pristine Graphene Probed by Microwave Imaging,” *Nano Lett.*, vol. 9, no. 11, pp. 3762–3765, Nov. 2009.
- [12] P. D. Wolf, R. Stephenson, T. Trenkler, T. Clarysse, T. Hantschel, and W. Vandervorst, “Status and review of two-dimensional carrier and dopant profiling

using scanning probe microscopy,” *J. Vac. Sci. Technol. B*, vol. 18, no. 1, pp. 361–368, Jan. 2000.

- [13] K. Lai, W. Kundhikanjana, M. Kelly, and Z. X. Shen, “Modeling and characterization of a cantilever-based near-field scanning microwave impedance microscope,” *Rev. Sci. Instrum.*, vol. 79, no. 6, p. 63703, Jun. 2008.
- [14] D. Hebert, “Optical characterization of copper indium gallium diselenide thin films,” Dec-2012. [Online]. Available: <http://hdl.handle.net/2142/42271>.
- [15] M. Tuteja, P. Koirala, S. MacLaren, R. Collins, and A. Rockett, “Direct observation of electrical properties of grain boundaries in sputter-deposited CdTe using scan-probe microwave reflectivity based capacitance measurements,” *Appl. Phys. Lett.*, vol. 107, no. 14, p. 142106, Oct. 2015.

CHAPTER 4

DEFECT LEVELS IN THE MACROSCOPIC BAND STRUCTURE

4.1 Introduction

In this chapter the defect-assisted optical transitions in the electronic band structure of polycrystalline rf-sputtered CdTe films are analyzed and compared to the electronic band structure of single crystal and CSS-grown CdTe in order to study carrier recombination pathways that affect photovoltaic performance of these films. Photoluminescence (PL) spectroscopy is used to study the radiative recombination in the energy band of rf-sputter deposited CdS/CdTe film structures as a function of laser excitation power and sample temperature. Findings from this work include the effect of Cu incorporation on the CdS/CdTe junction spectra, similarities between CdTe film spectra for these samples and for the films deposited by CSS, and identification of origins of sub-gap recombination peaks appearing in the spectra.

4.2 Results

PL spectra are obtained from two CdS/CdTe structure samples. The first sample is the CdCl₂ annealed CdS/CdTe sample and it is referred to as Sample A in this study. The second sample is the completed CdTe device structure with a CdCl₂ annealed CdS/CdTe structure and a Cu/Au bilayer back contact. This sample is referred to as Sample B in this study. In the following the details of the PL spectra are provided.

4.2.1 Excitation from the CdTe surface (Sample A)

The PL spectra obtained at various temperatures by exciting the CdTe side of the CdCl₂-treated, uncontacted CdS/CdTe junction sample are shown in Figure 4.1(a). These data represent the back ~100 nm of the CdTe which are easily within a minority carrier diffusion length of the back surface. The excitation power used was ~0.7 mW. Figure 4.1(b) shows the PL spectra obtained at 82 K at excitation powers from 0.02 to 1.55 mW. Taken together, the data in Figures 1 show that the Sample A PL spectrum consists of two prominent bands centered at ~1.42 eV and ~1.55 eV for temperatures up to 120 K. The 1.42 eV sub-bandgap transition is dominant at low excitation powers up to ~0.7 mW

[as seen from Figure 4.1(b)] and the near band gap 1.55 eV transition band becomes dominant at higher excitation powers and higher temperatures. The 1.55 eV band has a distinct shoulder near 1.58 eV in 82 K spectrum, which dominates the PL spectra for temperatures greater than 160 K and less than some temperature between 180 and 295 K.

In order to calculate the relative intensities of various emission processes to identify their origins, the spectra were peaks fit as follows. The 1.42 eV transition in 82 K spectra, as shown in Figure 4.1(a), was fit with an exponentially modified Gaussian function [1], [2] to accommodate the asymmetric peak shape; the peak at 1.55 eV was fit with a Lorentzian function; and the shoulder at 1.58 eV was fit with a Gaussian function. Figure 4.2(a) shows the variations of the 1.42 eV and 1.55 eV band integrated luminescence as a function of excitation power at 82 K. The intensity data for both are well described by

$$I_{PL} = C I_L^k \quad (4.1)$$

where I_{PL} is the measured luminescence, I_L is the incident laser power and C is a constant. For the 82 K spectra, the values of k obtained from the curve fit are 0.6 ± 0.1 and 1.9 ± 0.3 for the 1.42 eV and 1.55 eV transitions, respectively. The errors in k values are determined per a 95% confidence interval. According to Schmidt et al. [3], donor-acceptor (DA) and free-to-bound (FB) transitions have $k < 1$ and excitonic (X) transitions have $1 < k < 2$. This suggests the 1.42 eV and 1.55 eV emissions are DA/FB and X transitions, respectively. Similar k values were obtained upon analysis of the luminescence at other temperatures in the range of 82-140 K.

It can be observed from Figure 4.1(a) that the 1.42 eV transition luminescence is quenched as the measurement temperature is increased from 82 K to 295 K. The thermal quenching of this luminescence [shown in Figure 4.2(b)] was used to calculate the activation energy for this process. The functional relationship between the integrated luminescence, $I(T)$, and temperature (T) for the FB transition was modeled by:

$$I(T) = \frac{A}{1 + BT^{3/2}e^{\Delta E/k_B T}} \quad (4.2)$$

where ΔE represents the ionization energy of the bound state to the valence/conduction band contributing to the FB transitions. Similarly, temperature dependence of DA transition was modeled by:

$$I(T) = \frac{A}{1 + BT^{3/2}e^{\Delta E_1/k_B T} + CT^{3/2}e^{\Delta E_2/k_B T}} \quad (4.3)$$

where, ΔE_1 and ΔE_2 represent the ionization energies of the donor and acceptor states respectively. It is worth noting that a multiplication prefactor of $T^{3/2}$ is used before the exponential terms in equations (4.2) and (4.3), to indicate thermal depopulation of the bound states into the conduction/valence band edges [4]. The $T^{3/2}$ prefactor denotes the temperature dependence of effective density of states at the band edges and is absent in case of depopulation into another defect level. A suitable temperature fit for the 1.42 eV peak luminescence obtained by using equation (4.2), as shown in Figure 4.2(b) gives $\Delta E = 100 \pm 14$ and 97 ± 4 meV at excitation powers of ~ 0.5 and ~ 0.9 mW, respectively. These data when fit with equation (4.3) yield an error scale of over 100 meV. Thus, it is likely that the sub-gap peak observed is a FB transition involving a bound state with ionization energy of ~ 100 meV.

The sharp peak at 1.55 meV is likely an X transition based on the arguments per equation (4.1), presented above. The fact that the peak position for this transition remains nearly fixed at 1.55 eV (at 82 K) as the excitation power is increased, as shown in Figure 4.1(b), confirms the assignment to an excitonic transition. The slight red shift observed for this peak with higher excitation powers is likely due to local sample heating by the laser beam. A temperature dependent quenching behavior for the X transition was observed and was modeled using equation (4.2). In this case, ΔE corresponds to the exciton binding energy. This fit, as shown in Figure 4.2(b) at ~ 0.9 mW yields an exciton binding energy of 25 ± 8 meV, which is similar to thermal energy of ~ 26 meV at 295 K. This supports our observation of the excitonic peaks in 295 K spectra obtained using higher excitation powers (> 1.5 mW at 295 K). A very simple calculation of free exciton

binding energy (E_x) using hydrogenic model for Coulomb attraction between electron and holes gives:

$$E_x = m_r e^4 / 2(4\pi\epsilon_r\epsilon_o\hbar)^2 \quad (4.4)$$

where $m_r^{-1} = m_e^{-1} + m_h^{-1}$, $m_{e/h}$ is the electron/hole effective mass, $\epsilon_r\epsilon_o$ is the product of the dielectric constant of CdTe and the vacuum permittivity. Plugging $m_e=0.11$ [5], $m_h=0.8$ [6] and $\epsilon_r=10.31$ [7], a value of $E_x = 12.3$ meV is obtained for CdTe. This value of E_x differs by more than a factor of two from the experimentally obtained exciton binding energy of 25 ± 8 meV. This is a strong indication that the exciton is bound to an impurity and thus its binding energy increases due to the contribution from the impurity state.

Upon analyzing the variation of the peak position of the 1.58 eV transition, seen in Figure 4.1(a), as a function of temperature at ~ 0.7 mW excitation power, a temperature coefficient of $-(3.5\pm 0.5) \times 10^{-4}$ eV/K is obtained. This value is close to the value of -3.0×10^{-4} eV/K, as found by Camassel et al. [8], for the temperature coefficient describing the band gap variation in CdTe. Thus, the change in position of the 1.58eV transition corresponds well with the expected band edge variation with temperature. Also, the energy difference between the X emission and the band edge peak remains constant at ~ 30 meV as the excitation power or temperature are varied, as seen from Figures 1. This also confirms the assignment of this transition pair to X and a band edge transition as the X emission follows the band edge transition as the temperature is varied, until the X emission is no longer observed.

4.2.2 Excitation from CdS/CdTe junction (Sample A)

The PL spectra obtained by 0.9 mW laser excitation from the glass side to probe CdS/CdTe junction (Sample A) at various temperatures are shown in Figure 4.3(a). A plot of spectra obtained at 82 K for various excitation powers on the same sample is shown in Figure 4.3(b). Those spectra show a broad emission band between 1.3-1.4 eV region and a peak at 1.55 eV, similar to the case of CdTe PL [Figure 4.1(b)] as measured from the CdTe film side. The spectra are dominated by the broad emission in the 1.3-1.4

eV region at lower excitation powers up to ~ 0.3 mW and the sharp 1.55 eV peak at higher excitation powers at 82 K, as can be seen from Figure 4.3(b).

Figure 4.4(a) shows the integrated luminescence of the two transitions in the 1.3-1.4 eV region and at 1.55 eV as a function of excitation power at 82 K. These are calculated by fitting the 1.3-1.4 eV transition and 1.55 eV transition with an exponentially modified Gaussian and a Voigt curve, respectively. The straight lines are fits to the data as per equation (4.1). From this, $k = 0.76 \pm 0.04$ and 2.6 ± 0.2 is obtained for these two transitions at 82 K, respectively. The error estimates are based on 95% confidence intervals. As in the case of Figure 4.1(a), the k value indicates that the broad peak in the 1.3-1.4 eV region in Figure 4.3(a) is a result of DA/FB recombination. However, $k=2.6$ is greater than the limit for excitonic recombination [3]. Presumably, multiple power-dependent processes are influencing this behavior resulting in the stronger dependence on np product (light intensity) than expected. However, the position of the 1.55 eV peak in the 82 K spectra remains fixed as the excitation power is varied, as seen from Figure 4.3(b). This is a clear signature that at least one of the involved processes is an excitonic emission.

An analysis similar to Section 4.2.1 shows that the broad 1.3-1.4 eV peak in 82 K spectra is a FB transition rather than a DA recombination. Using equation (4.3) to fit this peak at 0.5 mW excitation power delivered two activation energies of nearly the same value as when fit with equation (4.2), and the confidence intervals for the same were very large. Using equation (4.2) and following the same process as in Figure 4.2(b), the activation energy for the quenching of this transition is found to be 100 ± 25 meV at ~ 0.5 mW excitation power. Activation energies of 130 ± 45 meV and 90 ± 20 meV were obtained upon fitting the luminescence of the sub-bandgap peak at 0.9 mW and 0.77 mW respectively. These data and the corresponding fits are shown in Figure 4.4(b). Activation energies for the near band-edge peak at 1.55 eV in the 82 K spectra could not be determined using equation (4.2) or (4.3).

4.2.3 Excitation from CdS/CdTe junction (Sample B)

Figure 4.5(a) shows the CdS/CdTe heterojunction PL spectra as obtained by exciting the sample with Cu-containing back contacts (Sample B) from the glass side for

~0.5 mW excitation at various temperatures, as listed in the figure. This is different from the study in Figures 1 and 3 in that Cu has been introduced from the back contact. The 82 K spectra consist of a broad sub-bandgap emission with a peak at 1.41 eV and a sharper peak centered around 1.56 eV. Figure 4.5(b) is a plot of PL spectra, similar to those of Figures 1(b), 3(b), for various excitation powers as obtained from the CdS/CdTe heterojunction at 82 K. It is clear that for nearly all temperatures and excitation powers the near band gap peak at ~1.56 eV in 82 K spectra is the dominant transition. Thus, due to Cu incorporation, the sub-bandgap emission is suppressed and can be observed only up to 120 K, as seen in Figure 4.5(a). The 1.58 eV shoulder at 82 K is less evident than in the case of sample A. Only at temperatures above 180 K when the emission is broad, there is a possible contribution from the 1.58 eV emission peak.

Figure 4.6 shows the variation of the 1.41 eV sub-gap and ~1.56 eV integrated peak luminescence (in 82 K spectra) with respect to excitation power. As per equation (4.1) the values of k are found to be 0.90 ± 0.12 and 1.9 ± 0.3 for the two transitions, respectively. The error estimates are based on 95% confidence intervals. Thus, it can be concluded, as in other measurements, that the sub-gap transition is likely a DA/FB transition and the ~1.56 eV transition is an X transition [3]. The claim that 1.56 eV transition is X is also supported by the fixed energy position of this peak as the excitation power is increased as in Figure 4.5(b). The activation energy value for DA/FB transition could not be determined due to the weaker luminescence of this transition and the associated rapid temperature decay.

4.3 Discussion

The temperature dependent PL spectra obtained at a fixed excitation power from the back ~100 nm of the CdTe, and the first ~100 nm of the CdTe near the CdS/CdTe interface, including the graded region of the junction, (with and without back contacts) are shown in Figures 4.1(a), 4.3(a) and 4.5(a), respectively. The absence of a significant shift in the near band edge emission in Figures 3 and 5 relative to Figures 1 suggests that the emission near the junction is not representative of the graded material. The low temperature sputtering growth (as compared to CSS) is likely to result in less intermixing and inter-diffusion of CdS and CdTe, resulting in reduced formation of a lower band gap

alloy $\text{CdS}_x\text{Te}_{1-x}$ along the junction. Some amount of band gap grading along the junction is possible, however, the existence of a built-in electric field in the depletion region near the junction would separate the photo-generated carriers out and hence reduce the avenues available for recombination representing the graded band gap along the junction. This effect also leads to enhanced non-radiative recombination of the carriers outside the depletion region as the radiative recombination rate depends on the np-product, which is reduced due to carrier separation. Hence, the band-edge luminescence (1.58 eV peak in the 82 K spectra from CdTe film) is suppressed in the CdS/CdTe junction spectra.

The near band edge emissions from the bare CdS/CdTe junction excited from both, the film and the substrate sides [Figures 4.1(b) and 4.3(b)] have a peak centered at 1.55 eV. This peak corresponds to a bound excitonic emission as shown in Section 4.2.1, which indicates that both of these peaks are due to excitons bound to the same impurity/defect. Near band edge acceptor bound excitons have been observed in PL spectra of CdTe [8,24,25] and the dominant acceptor in CdTe is thought to be the $\text{V}_{\text{Cd}}\text{-Cl}_{\text{Te}}$ defect complex. When Cu is introduced via the back contact, the luminescence properties of the CdS/CdTe junction are affected. The X peak now moves to 1.56 eV from 1.55 eV as expected if this peak is an acceptor bound excitonic emission, since after the introduction of Cu, Cu_{Cd} is the primary acceptor [9] and the corresponding emission has a higher energy than exciton bound to $\text{Cl}_{\text{Te}}\text{-V}_{\text{Cd}}$ defect complex [10], [11].

On comparing the PL from CdS/CdTe junctions before and after the introduction of Cu as a function of excitation power [Figures 4.3(b) and 4.5(b)], it is seen that the sub-bandgap transitions are suppressed near the heterojunction upon addition of Cu even though the Cu is added at the back surface of the device. Upon annealing, Cu deposited on the surface of the CdTe is incorporated as Cu interstitials (Cu_i) [12], a fast diffusing donor species that interacts with V_{Cd} to form a $\text{Cu}_i\text{-V}_{\text{Cd}}$ acceptor complex, Cu on V_{Cd} (Cu_{Cd}) acceptors and $\text{Cu}_{\text{Cd}}\text{-Cu}_i$ neutral complexes [13]. It is likely that the interaction of Cu_i with V_{Cd} to form Cu_{Cd} or $\text{Cu}_i\text{-V}_{\text{Cd}}$ disrupts the $\text{Cl}_{\text{Te}}\text{-V}_{\text{Cd}}$ acceptor complex and hence strongly attenuates the sub-band gap transition that is observed in PL from samples without Cu incorporation [Figures 4.1(a) and 4.3(a)], which is a result of transitions involving the $\text{V}_{\text{Cd}}\text{-Cl}_{\text{Te}}$ complex. According to Romero et al. [14], Cu_{Cd} acceptors are

recombination centers of much higher efficiency than any other defect complex involving Cu. It is likely that the remaining sub-bandgap transition, as seen in Figure 4.5(a) at low temperatures (< 120 K), is due to a transition involving Cu_{Cd} .

On comparison of Figures 4.1(b), 4.3(b), and 4.5(b), it is noticed that there is a transition excitation power where the PL emission changes from being dominated by the sub-band gap transitions to near band edge X transitions. This is observed at ~ 0.7 , ~ 0.3 mW in the case of Figures 4.1(b) and 4.3(b), respectively. However, in Figure 4.5(b) the X peak is dominant at nearly all excitation powers due to the quenching of sub-gap recombination. One possible reason for this change in the dominant luminescence with excitation power could be larger carrier lifetimes for the FB than the X transitions. As the carrier generation rate is increased by increasing the excitation power, the rate of recombination via the sub-bandgap transitions is not sufficient to recombine all of the generated carriers and the near band edge emissions result. However, further work in this direction is needed before any conclusive statement can be made.

All of the observed spectra share a similar overall shape. The two characteristic emissions in all PL spectra are the sub-band gap DA/FB emissions and the near band edge excitonic emissions. These are observed in the 1.3-1.4 eV region and near 1.55 eV respectively. Previous studies on the luminescence properties of CdTe [15]–[17] and device quality CdS/CdTe heterojunctions [14], [18], [19] have reported similar peaks. For instance, a 1.42 eV peak in the CdTe PL spectrum has been associated with a transition involving $\text{Cl}_{\text{Te}}\text{-V}_{\text{Cd}}$ defect complex [20]. An acceptor binding energy of 120 meV has been calculated for the $\text{Cl}_{\text{Te}}\text{-V}_{\text{Cd}}$ defect complex [21]. In Sections 4.2.1 and 4.2.2, it was shown that these transitions correspond to a FB transition, whose temperature dependent quenching behavior was modeled closely by using equation (4.2). Thus, the low energy transitions observed in Figures 4.1(a) and 4.3(a) are FB transition with a bound state with activation energy of ~ 100 meV as obtained from the fits. However, a determination of activation energy for the low energy sub-band gap peak was not possible for Sample B [Figure 4.5(b)], due to the rapid thermal decay of this peak. In addition, near band edge excitonic emissions have also been observed and associated with acceptor bound excitons

[10], [22], [23]. These similarities between the PL spectra obtained and those observed by others serve to show that the sputtered CdTe-based devices have comparable electronic structure to those deposited using other methods, including the popular CSS growth. In addition, several peaks in the PL spectra observed here have origins that are same as those in single crystal CdTe samples.

4.4 Conclusions

Low temperature PL spectra from sputter-deposited CdTe surfaces and CdS/CdTe junctions, and their line shape and temperature quenching behavior reveal that the dominant emission peaks primarily arise from FB/DA and bound exciton recombinations. A detailed analysis of temperature and excitation power dependence of the PL spectra revealed the most prominent efficiency limiting defects in these films. In the case of PL from CdCl₂ treated CdTe film (without the inclusion of Cu), it was possible to associate the sub-gap luminescence peak to a FB transition involving a bound state with ionization energy of ~100 meV. The acceptor level for the FB emission in this case was concluded to be Cl_{Te}-V_{Cd} complex. Upon Cu incorporation, the DA transition is suppressed, probably due to Cu occupying V_{Cd} sites. The residual sub-bandgap transition is possibly due to Cu_{Cd} acceptors. The observed transitions are summarized in Figure 4.7 in the form of an energy diagram depicting various defect levels and their corresponding emissions. A shift in the dominant luminescence from sub-bandgap to near band edge transitions as a function of increasing laser excitation power was observed. In addition, the near band gap emission in the CdS/CdTe spectra (Sample A) was concluded to be a convolution of multiple radiative recombination transitions. Further work is required to ascertain the reason for the above-mentioned peak shift and to analyze the constituent radiative transitions responsible for the anomalous k-value for the near band gap peak in the CdS/CdTe junction spectra (Sample A).

The similarities between the PL spectra of polycrystalline (rf-sputtered and CSS-grown) and single crystal CdTe samples indicate that a probe into the macro-scale electronic behavior of the polycrystalline samples might not hold the key to explaining the unique behavior of solar cells based on polycrystalline CdTe. Thus in the following

chapters in this thesis, the micro-scale electronic behavior of polycrystalline CdTe samples have been analyzed.

4.5 Figures

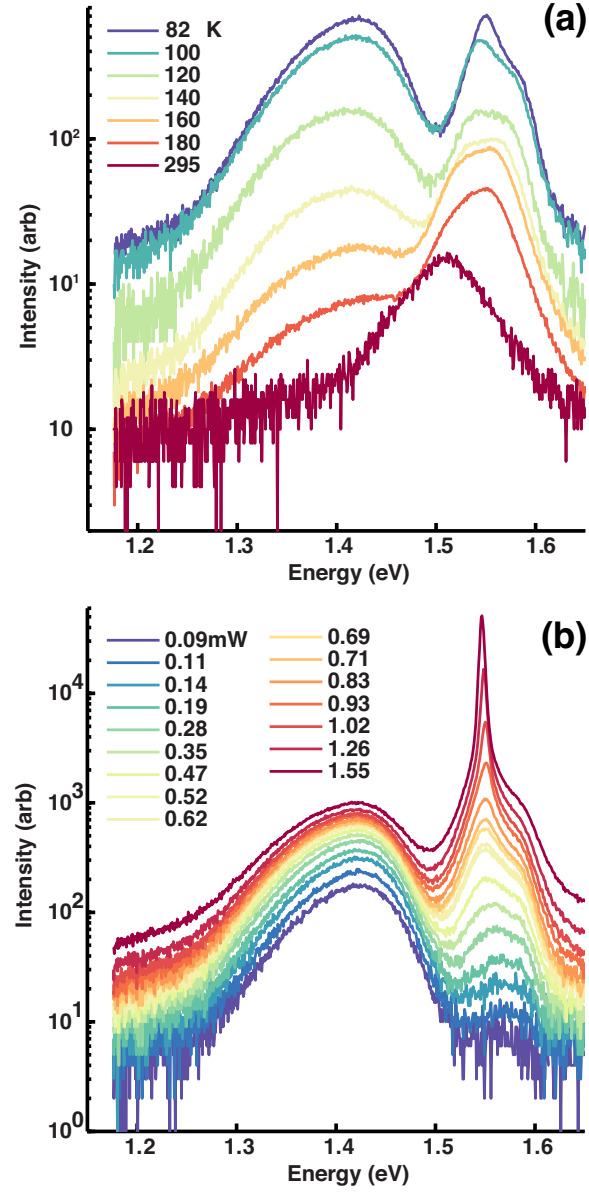


Fig. 4.1: PL spectra obtained by exciting CdTe surface (Sample A) at (a) ~ 0.7 mW laser excitation power as a function of measurement temperature and (b) 82 K as a function of laser excitation power. Image taken, with permission, from [24].

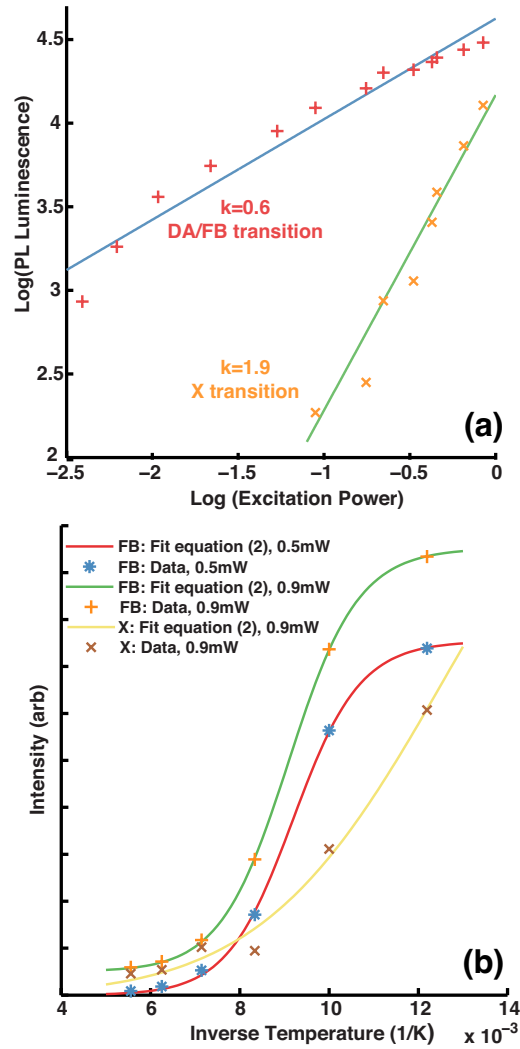


Figure 4.2. Plot of (a) DA/FB and X emission luminescence vs. excitation power and (b) FB and X luminescence vs. inverse temperature from the CdTe PL spectra (sample A). The excitation power levels are as indicated. Solid lines represent least squares fit to data as per equation (4.1) and (4.2) in (a) and (b), respectively. Data points are experimentally observed. Image taken, with permission, from [24].

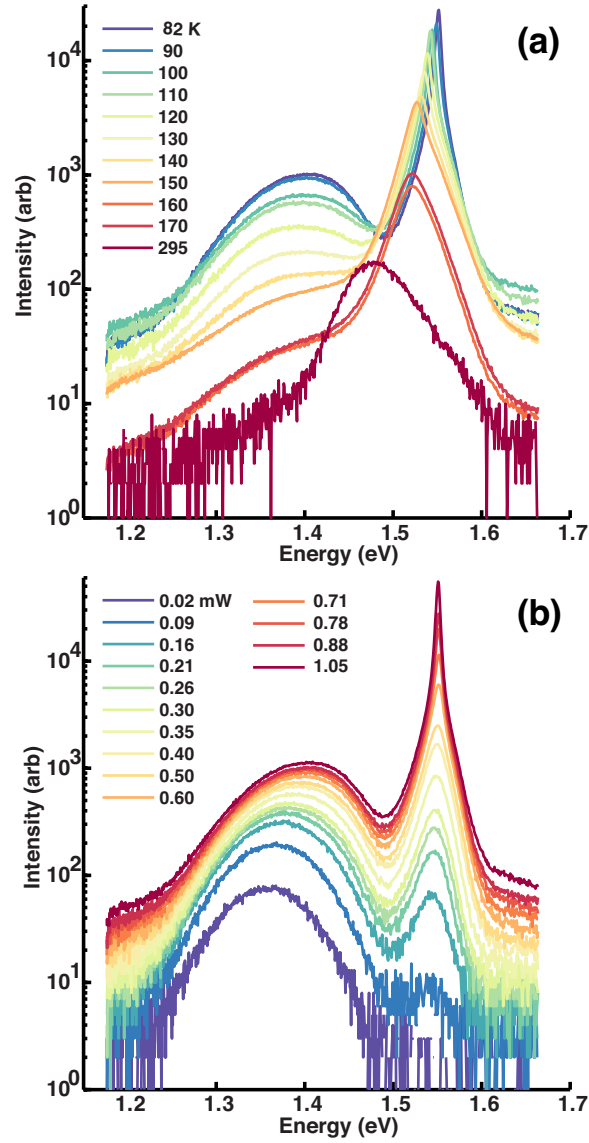


Figure 4.3: PL spectra obtained by exciting the CdS/CdTe junction (Sample A) from the glass side at (a) ~ 0.9 mW laser excitation power as a function of measurement temperature and (b) 82 K as a function of laser excitation power. Image taken, with permission, from [24].

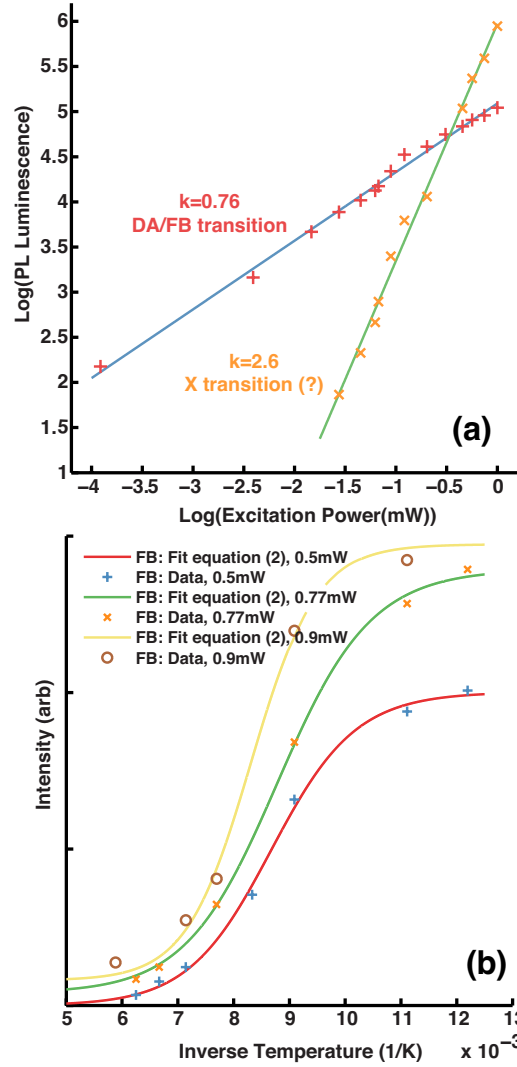


Figure 4.4: Plot of (a) DA/FB and X emission luminescence vs. excitation power and (b) FB luminescence vs. inverse temperature from the CdS/CdTe junction PL spectra (Sample A). The excitation powers used are indicated. Solid lines represent least squares fit to data as per equation (4.1) and (4.2) in (a) and (b), respectively. Symbols represent experimental data. Image taken, with permission, from [24].

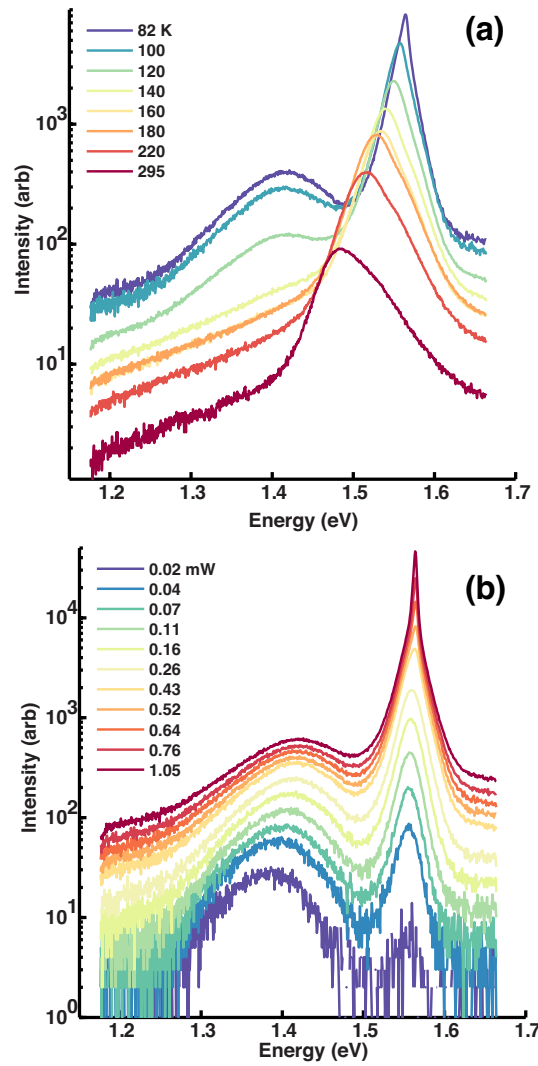


Figure 4.5: PL spectra obtained by exciting the CdS/CdTe junction from the glass side for Sample B (with Cu) at (a) 0.5 mW laser excitation power as a function of measurement temperature and (b) 82 K as a function of laser excitation power. Image taken, with permission, from [24].

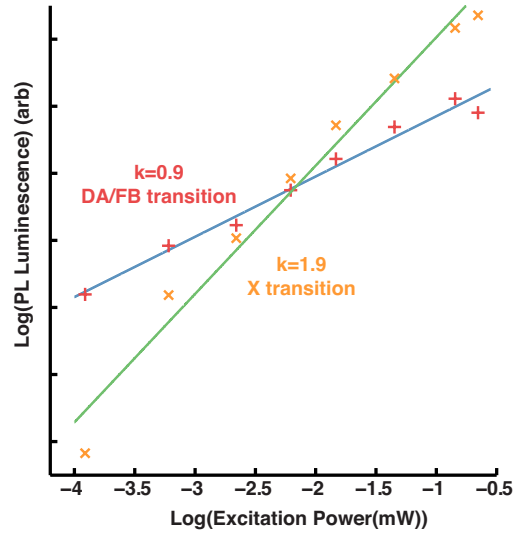


Figure 4.6: Plot of DA/FB and X emission luminescence vs. excitation power for the CdS/CdTe junction PL from Sample B (with Cu). Straight lines are least squares fit to data as per equation (4.1). Image taken, with permission, from [24].

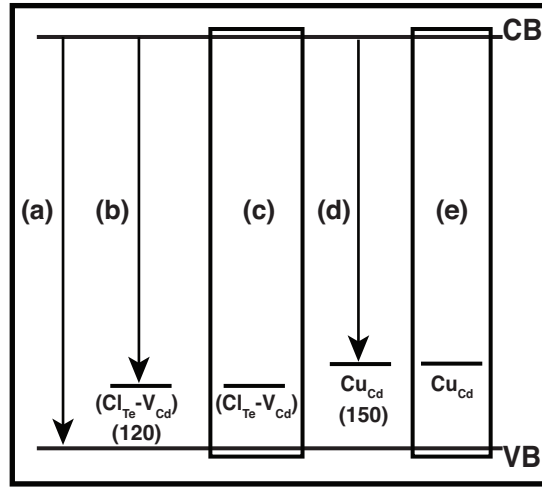


Figure 4.7: A suggested energy band diagram showing various defect levels and possible transitions that lead to the observed PL spectra. (a) Band to band recombination; (b) FB transition involving $(Cl_{Te}-V_{Cd})$ acceptor; (c) $(Cl_{Te}-V_{Cd})$ acceptor bound exciton; (d) DA/FB transition involving Cu_{Cd} acceptor; and (e) Cu_{Cd} acceptor bound exciton. The binding energy values (indicated in parenthesis) are taken from references [9], [21]. Image taken, with permission, from [24].

4.6 References

- [1] R. E. Pauls and L. B. Rogers, "Band broadening studies using parameters for an exponentially modified Gaussian," *Anal. Chem.*, vol. 49, no. 4, pp. 625–628, Apr. 1977.
- [2] W. W. Yau, "Characterizing skewed chromatographic band broadening," *Anal. Chem.*, vol. 49, no. 3, pp. 395–398, Mar. 1977.
- [3] T. Schmidt, K. Lischka, and W. Zulehner, "Excitation-power dependence of the near-band-edge photoluminescence of semiconductors," *Phys. Rev. B*, vol. 45, no. 16, pp. 8989–8994, Apr. 1992.
- [4] J. Krustok, H. Collan, and K. Hjelt, "Does the low-temperature Arrhenius plot of the photoluminescence intensity in CdTe point towards an erroneous activation energy?," *J. Appl. Phys.*, vol. 81, no. 3, pp. 1442–1445, Feb. 1997.
- [5] D. T. F. Marple, "Effective Electron Mass in CdTe," *Phys. Rev.*, vol. 129, no. 6, pp. 2466–2470, Mar. 1963.
- [6] M. A. Berding, "Native defects in CdTe," *Phys. Rev. B*, vol. 60, no. 12, pp. 8943–8950, Sep. 1999.
- [7] I. Strzalkowski, S. Joshi, and C. R. Crowell, "Dielectric constant and its temperature dependence for GaAs, CdTe, and ZnSe," *Appl. Phys. Lett.*, vol. 28, no. 6, pp. 350–352, Mar. 1976.
- [8] J. Camassel, D. Auvergne, H. Mathieu, R. Triboulet, and Y. Marfaing, "Temperature dependance of the fundamental absorption edge in CdTe," *Solid State Commun.*, vol. 13, no. 1, pp. 63–68, Jul. 1973.
- [9] J. P. Laurenti, G. Bastide, M. Rouzeyre, and R. Triboulet, "Localized defects in p-CdTe:Cu doped by copper incorporation during Bridgman growth," *Solid State Commun.*, vol. 67, no. 12, pp. 1127–1130, Sep. 1988.
- [10] K. M. James, J. L. Merz, and C. E. Jones, "Luminescence study of copper-implanted and rapid-thermal-annealed cadmium telluride," *J. Vac. Sci. Technol. A*, vol. 6, no. 4, pp. 2664–2669, Jul. 1988.
- [11] T. Okamoto, A. Yamada, and M. Konagai, "Optical and electrical characterizations of highly efficient CdTe thin film solar cells," *Thin Solid Films*, vol. 387, no. 1–2, pp. 6–10, May 2001.

- [12] K. K. Chin, T. A. Gessert, and S.-H. Wei, "The roles of CU impurity states in CdTe thin film solar cells," in *2010 35th IEEE Photovoltaic Specialists Conference (PVSC)*, 2010, pp. 001915–001918.
- [13] G. Zoth, F. G. Ridel, and W. Schröter, "Pairing between Fast Diffusing Donors and Shallow Acceptors in p-CdTe," *Phys. Status Solidi B*, vol. 172, no. 1, pp. 187–192, 1992.
- [14] M. J. Romero, D. S. Albin, M. M. Al-Jassim, X. Wu, H. R. Moutinho, and R. G. Dhere, "Cathodoluminescence of Cu diffusion in CdTe thin films for CdTe/CdS solar cells," *Appl. Phys. Lett.*, vol. 81, no. 16, pp. 2962–2964, Oct. 2002.
- [15] D. . Halliday, J. . Eggleston, and K. Durose, "A photoluminescence study of polycrystalline thin-film CdTe/CdS solar cells," *J. Cryst. Growth*, vol. 186, no. 4, pp. 543–549, Mar. 1998.
- [16] T. Taguchi, J. Shirafuji, and Y. Inuishi, "Edge and Donor-Acceptor Pair Emissions in Cadmium Telluride," *Jpn. J. Appl. Phys.*, vol. 12, no. 10, pp. 1558–1566, 1973.
- [17] S. Vatavu *et al.*, "Photoluminescence studies of CdTe films and junctions," *Thin Solid Films*, vol. 515, no. 15, pp. 6107–6111, May 2007.
- [18] S. Vatavu, H. Zhao, I. Caraman, P. Gaşin, and C. Ferekides, "The copper influence on the PL spectra of CdTe thin film as a component of the CdS/CdTe heterojunction," *Thin Solid Films*, vol. 517, no. 7, pp. 2195–2201, Feb. 2009.
- [19] D. Grecu and A. D. Compaan, "Photoluminescence study of Cu diffusion and electromigration in CdTe," *Appl. Phys. Lett.*, vol. 75, no. 3, pp. 361–363, Jul. 1999.
- [20] T. Okamoto, Y. Matsuzaki, N. Amin, A. Yamada, and M. Konagai, "Characterization of Highly Efficient CdTe Thin Film Solar Cells by Low-Temperature Photoluminescence," *Jpn. J. Appl. Phys.*, vol. 37, no. Part 1, No. 7A, pp. 3894–3899, 1998.
- [21] D. M. Hofmann, P. Omling, H. G. Grimmeiss, B. K. Meyer, K. W. Benz, and D. Sinerius, "Identification of the chlorine A center in CdTe," *Phys. Rev. B*, vol. 45, no. 11, pp. 6247–6250, Mar. 1992.
- [22] J. Aguilar-Hernandez, G. Contreras-Puente, H. Flores-Llamas, H. Yee-Madeira, and O. Zelaya-Angel, "The temperature-dependence of the energy band gap of CSVT-

grown CdTe films determined by photoluminescence,” *J. Phys. Appl. Phys.*, vol. 28, no. 7, p. 1517, Jul. 1995.

- [23] J. Aguilar-Hernández, G. Contreras-Puente, J. M. Figueroa-Estrada, and O. Zelaya-Angel, “Photoluminescence Studies of Semiconducting Polycrystalline CdTe Films,” *Jpn. J. Appl. Phys.*, vol. 33, no. Part 1, No.1A, pp. 37–41, 1994.
- [24] M. Tuteja, P. Koirala, J. Soares, R. Collins, and A. Rockett, “Low temperature photoluminescence spectroscopy studies on sputter deposited CdS/CdTe junctions and solar cells,” *J. Mater. Res.*, vol. 31, no. 2, pp. 186–194, 2016.

CHAPTER 5

RELATIVE MAJORITY CARRIER CONCENTRATION DISTRIBUTION AT THE MICROSCALE

5.1 Introduction

The objective of this chapter is to study the microscale majority carrier concentration distribution on the surface of the CdTe film in Glass/TCO/CdS/CdTe samples. The CdTe is p-doped and the analysis presented reveals the microscale concentration variation of holes on the surface of CdTe. Scanning microwave impedance microscopy (sMIM) is used to accomplish this work and the measurements are performed on unfinished CdTe solar cells (Glass/TCO/CdS/CdTe) fabricated via rf-sputtering and close-spaced sublimation (CSS) methods. It is anticipated that the CdCl₂ anneal process, an integral part of the CdTe solar cell manufacture process that boosts the cell performance by a factor of two or more, affects the carrier concentration at the grain boundaries and this study provides the first direct observation of microscale effects of the CdCl₂ annealing process on the electronic properties of the CdTe films used in photovoltaic devices.

5.2 Anticipated Effects of the CdCl₂ Annealing Process

Cl acts as an n-type dopant in CdTe [1] and upon CdCl₂ anneal, Cl incorporated in CdTe segregates along the grain boundaries, as shown by electron energy loss spectroscopy [1]–[3], secondary ion mass spectrometry [4], atom probe tomography [5], and auger electron spectroscopy [6] measurements. The presence of Cl, an n-dopant for CdTe, at grain boundaries should result in local doping type inversion/carrier depletion, resulting in p-doped CdTe grains separated by n-type/depleted p-type grain boundaries [1], [7]. This local doping type inversion/carrier depletion is thought to result in a downward band bending along the grain-grain boundary interface, which will promote photo-generated charge carrier segregation [1]. The above-mentioned thinking is quite prevalent in the community, however, there are several other possibilities that have been proposed in several works over the past few years. These have already been discussed in some detail in Section 2.4. Despite all studies suggesting a majority carrier concentration

change along the grain boundaries in CdTe films there has not been a study that directly demonstrates this change upon the CdCl₂ anneal treatment.

5.3 Results

5.3.1 Modes of Operation of sMIM

As discussed earlier, the sMIM instrument is an add-on to a conventional atomic force microscopy (AFM) setup. Hence, there are more than one modes of operation for the sMIM instrument that are possible, similar to the AFM instruments. The sMIM instrument can be operated in both contact and tapping modes of operation of the sMIM tip but the contact mode is by far the most popular mode of operation due to enhanced signal collection and ease of data interpretation [8]–[11]. However, conventional contact and tapping mode imaging using sMIM is prone to influence of sample topography-induced artifacts that are often stronger than the actual signals. This issue is described in detail in Section 5.3.1.1. Unfortunately the literature on sMIM, until now, has focused on analysis of smooth/flat samples (< 10 nm RMS roughness) and the case of avoiding sample topography artifacts in the measurement has not been adequately addressed. In the present work, it has been demonstrated for the first time that contact mode differential capacitance (dC/dV) measurements using the sMIM instrument are capable of analyzing rough samples and overcoming the sample topography-induced measurement artifacts. This will be described in Section 5.3.1.2.

5.3.1.1 MIM with DC Bias Applied to the Tip (Capacitance Measurement)

A general overview of this measurement setup is provided in Section 3.3. The details of this measurement as applied to the polycrystalline CdTe films are provided here. The data was obtained by performing the MIM analysis in contact mode scanning on the sample with a DC bias applied to the MIM probe. The results are shown in Figures 5.1. Figure 5.1(a) shows the sample topography information for the CdCl₂ annealed CSS deposited CdTe sample along with the MIM capacitance data [Figure 5.1(c)], which is simultaneously collected. Upon comparison, it is clear that areas of local minima in sample topography are also the areas of higher MIM capacitance. This is further emphasized by Figure 5.1(d) where line scans on the topography and capacitance images

are presented along the dashed line in Figures 5.1(a)-(c). It can be seen that at areas of lower sample topography (indicated by arrows), a much higher MIM capacitance signal is observed, regardless of the DC voltage bias applied to the tip. One can see from the deflection (derivative of topography) image in Figure 5.1(b) that these areas indicated by arrows in Figure 5.1(d) are also the areas that correspond to the grain boundary regions. This strong correlation between the sample topography and the MIM capacitance is because of an effect described in Figure 5.2. As the MIM probe scans a sample with rough topography and comes across an area with a local depression in topography the apparent tip-sample interaction increases because the sidewalls of the tip also interact with the sample in addition to the tip apex, which is conventionally the only part of the tip that interacts with the sample (on a smooth sample). This increase in the tip-sample interaction leads to an enhanced MIM signal being collected by the MIM electronics, which manifests itself as a higher capacitance signal being measured along the areas of depression in the sample topography.

Hence, it is clear from Figures 5.1 and 5.2 that any carrier concentration difference, if present, between the grains and the grain boundaries in CSS grown CdTe due to the CdCl_2 anneal treatment (as mentioned in Section 5.2) is completely overshadowed by the effect of the sample topography on the MIM signal. Similar behavior is observed upon the analysis of sputter-deposited CdTe samples by this technique. This necessitates an alternate mode of MIM measurement that yields results that are not overpowered by sample topography-induced artifacts.

5.3.1.2 Lock-in MIM Measurement (Differential Capacitance)

dC/dV measurements were performed in contact mode, with the conductive sMIM tip and the oxide coated sample effectively forming a metal-oxide-semiconductor (MOS) structure. The transparent contact (TCO layer) of each of the samples was electrically grounded and a DC bias and/or an AC bias ($< 300 \text{ KHz}$) were applied to the tip. The frequency of the ac bias is chosen to maximize the differential capacitance (dC/dV) signal. All AC bias voltage amplitudes given below are half of the peak-to-peak signal values, thus a 1 V ac bias refers to sweeping the signal by $\pm 1 \text{ V}$. The capacitance change caused by the ac bias was measured using a lock-in amplifier. A schematic of the

experimental setup and the tip signal used to perform the measurements has been presented in Figure 3.4. The first order of business here is to demonstrate the topography invariance of the signal acquired using this measurement configuration.

Figure 5.3 (a) shows the simultaneously acquired dC/dV amplitude ($|dC/dV|$) signal overlaid on the 3D AFM topography obtained from a $CdCl_2$ annealed CdTe sample grown using rf-sputtering. The image was acquired with -2V DC bias and a 1V AC amplitude bias at 20kHz applied to the tip (applied AC and DC voltages thus sweeping from -1 to -3V) and a lock-in was used to measure the dC/dV signal. It is seen from Figure 5.3(a) that several areas corresponding to the grain boundaries have much higher $|dC/dV|$ signal than the grain bulk. Higher $|dC/dV|$ signal corresponds to a steeper C-V curve, which is a result of lower local carrier concentration [12]. Hence, Figure 5.3(a) shows that the grain boundaries in $CdCl_2$ annealed sputter-deposited CdTe sample exhibit a lower carrier concentration than the grain bulk. Further, the corresponding dC/dV phase (θ_c) image exhibited a phase variation of at most 29° across the image, which is much less than a phase flip of $\sim 180^\circ$ observed in the case of a p-type vs. an n-type semiconductor. This information is shown in Figures 5.4 and indicates that the grain boundaries are depleted p-type, relative to the p-type grain interiors, rather than inverted (n-type). The topographical invariant nature of this measurement is revealed by Figure 5.3(b), where it is seen that the $|dC/dV|$ signal from the same area is washed out when the tip DC bias is changed to +2V, keeping all other experimental parameters the same. This confirms that the $|dC/dV|$ signal is not a topographical artifact.

5.3.2 Effect of $CdCl_2$ Treatment

To demonstrate the effect of $CdCl_2$ treatment on the microstructural electronic properties of the polycrystalline CdS/CdTe films, sMIM analysis was performed on these samples, grown by rf-sputtering and close-spaced sublimation (CSS), with- and without the $CdCl_2$ treatment. The data for CSS samples was acquired with a 1 V amplitude AC and no DC bias applied to the sMIM tip (applied voltage thus sweeping from -1 to +1 V) and a lock-in amplifier was used to measure the dC/dV signal. For rf-sputtered CdTe films 1.5 V AC and -2 V DC biases were applied to the tip to obtain the dC/dV signal. In all measurements presented here, the combination of AC and DC bias was chosen to

maximize the dC/dV signal. The difference in bias values did not affect the qualitative behavior of the results.

Figures 5.5 (a)-(d) show the simultaneously acquired $|dC/dV|$ and AFM topography signals overlaid for the as-deposited and $CdCl_2$ annealed CdTe samples grown using rf-sputtering [Figures 5.5 (a), 5.5(b)] and CSS [Figures 5.5(c), 5.5(d)]. Although the actual $|dC/dV|$ signal ranges for Figures 5.5 (a)-(d) are slightly different, they have been put on the same color scale to enable easy comparison. Figures 5.6 (a)-(d) show the simultaneously acquired dC/dV phase angle, θ_c , signal overlaid on the AFM topography for the as-deposited and $CdCl_2$ annealed CdTe samples, grown using rf-sputtering and CSS. Similar to $|dC/dV|$ in Figures 5.5 (a)-(d), the θ_c signals in Figures 5.6 (a)-(d) are plotted on the same scale for all samples.

It is seen from Figures 5.5 (b) and 5.5 (d) that several areas in the $CdCl_2$ annealed CdTe samples corresponding to the grain boundaries have much higher $|dC/dV|$ signals than the grain bulk. Higher $|dC/dV|$ signal corresponds to a steeper C-V curve, which is a result of lower local carrier concentration [12]. Hence, Figures 5.5 (b) and 5.5 (d) show that the grain boundaries in $CdCl_2$ annealed CdTe, grown using both rf-sputtering and CSS, exhibit a lower majority carrier concentration than the grain bulk. Further, the corresponding θ_c images, shown in Figures 5.6 (b) and 5.6 (d), for the $CdCl_2$ annealed samples exhibit at most a phase variation of only 16° and 17° , respectively throughout the scan area. Although the phase signal is slightly lower along the grain boundaries as compared to the grains, a 16° or 17° phase difference is not indicative of a dopant-type inversion as dopant-type inversion warrants a phase flip of $\sim 180^\circ$ (π). This follows directly from the mirror image like nature of the C-V curves for the n- and p-doped semiconductor samples along the capacitance axis.

Figures 5.5 (a) and 5.5 (c) show the $|dC/dV|$ signals obtained from rf-sputtered and CSS-grown CdTe films, respectively, without $CdCl_2$ annealing. The CSS-grown samples, with and without $CdCl_2$ anneal treatment, share similar RMS surface roughness values of 145 nm and 163 nm, respectively but as can be seen from Figures 5.5 (c) and 5.5 (d), the grain boundaries in the CSS grown CdTe films do not exhibit reduced carrier concentrations (higher $|dC/dV|$ signal) in the non- $CdCl_2$ annealed sample. Similarly, grain

boundary carrier concentration reduction is not observed in rf-sputter deposited CdTe sample without the CdCl₂ annealing, as can be seen from Figure 5.5 (a). This reduced majority carrier concentration along the grain boundaries in the CdCl₂ treated samples coupled with the lack of dopant-type inversion between the grains and the grain boundaries implies that the grain boundaries are less p-doped as compared to the grain bulk. This leads to a downward bend bending along the grain-grain boundary interface, as shown described in Figure 5.7.

5.3.3 Evidence of photo-generated carrier separation

Figure 5.8 (a) shows the $|dC/dV|$ image of an area of the sputter-deposited and CdCl₂ annealed sample, obtained using a 2V AC amplitude bias (to obtain higher signal to noise ratio) at 20kHz, with no DC bias or sample illumination. Figure 5.8 (b) shows the $|dC/dV|$ image of the same area with blanket sample illumination using a broadband white light source. Upon comparison of the $|dC/dV|$ signals between Figures 5.8 (a) and 5.8 (b), it can be seen that when the sample is illuminated with light, the regions around some of the grain boundaries become brighter and the grains become slightly darker. This is evident from Figure 5.8 (c), which is a result of subtraction of Figure 5.8 (a) from Figure 5.8 (b). In Figure 5.8 (c), some of the grain boundaries exhibit a higher and grains exhibit a lower $|dC/dV|$ signal. The dC/dV phase images (not shown here), both with and without sample illumination, exhibited no observable features along grain boundaries with a maximum phase variation of 17° across the image. This suggests that upon illumination the carrier depletion around the grain boundaries increases (less p-type) as a result of collection of photo-generated electrons, while the bulk grains become slightly more p-type as a result of photo-generated hole accumulation. Hence, the photo-carrier separation can be directly observed between the grains and grain boundaries, due to the band ending effect shown in Figure 5.7.

5.4 Discussion

The observation of lower carrier concentration along grain boundaries in both rf-sputtered and CSS-grown CdTe films after CdCl₂ annealing points to p-doping compensation due to incorporation of Cl, a donor impurity in CdTe. Further, this gives

one explanation for the universally beneficial effect of CdCl_2 treatment on the efficiencies of polycrystalline CdTe solar cells as the carrier depletion induces band bending along the grain boundary-grain interface. This promotes photo-generated charge carrier separation as electrons segregate along the grain boundaries and holes remain in the grain bulk, as shown in Section 5.3.3.

A second explanation of the benefit of CdCl_2 treatment is recrystallization of CdTe grains, hence increasing open-circuit voltage and grain size. This can be most directly observed by comparing Figures 5.5 (a) and 5.5 (b), where it can be seen that CdTe grain size in sputter deposited films increases dramatically upon CdCl_2 annealing. The grain coarsening also leads to a significant increase in surface roughness for the sputter deposited film upon CdCl_2 annealing. The two effects of grain size increase and roughening do not occur, however, for the CSS deposited CdTe. It has been shown that the grain boundaries in CdTe provide low resistance paths for electrons to travel to the front contact [13], which indicates that it is better for CdTe devices to have large columnar grains with grain boundaries running throughout the thickness of the CdTe layer such that the photocurrent does not cross grain boundaries to reach a contact.

It is also evident from Figures 5.6 and 5.8 that not all grain boundaries show similar brightness in $|dC/dV|$ images. This suggests that not all grain boundaries are depleted by equal amounts and hence do not share common electrical properties. Similarly, neither do all grains share the same $|dC/dV|$ signal, suggesting that there is a variation of carrier concentration from one grain to another. Further, there is a gradual decrease in the carrier concentration from the center of the grain to the areas near the grain boundaries. These effects are best observed in Figure 5.8. This suggests that grains of a certain crystallographic orientation/size and the associated grain boundaries are more electrically active than others.

5.5 Conclusions

In conclusion, it is shown that even though the topography dominates the sMIM capacitance measurements on the surface of polycrystalline CdTe, one can still employ dC/dV measurements to determine the electronic properties and associated relative carrier

density at grain boundaries with respect to the grain bulk. Evidence of carrier concentration reduction along the grain boundaries was found in CdCl_2 annealed CdTe films deposited by both sputtering and CSS. This effect was absent in samples that have not been CdCl_2 annealed. Hence, the hypothesis of grain boundary carrier depletion in CdTe caused by CdCl_2 annealing likely due to Cl incorporation is validated. This creates band bending along grain-grain boundary interface, which facilitates photo-generated carrier separation. This separation has been observed by comparing the relative carrier concentrations with and without light exposure on the sample. Also, there is evidence that the crystallographic orientation/size of grains affects the electronic properties of the surrounding grain boundaries and their role in carrier separation. Thus, the work presented in this Chapter puts to rest all the speculations surrounding the nature of electronic properties (see Section 2.4) of the grain boundaries in CdTe films and their role in the photovoltaic action.

5.6 Figures

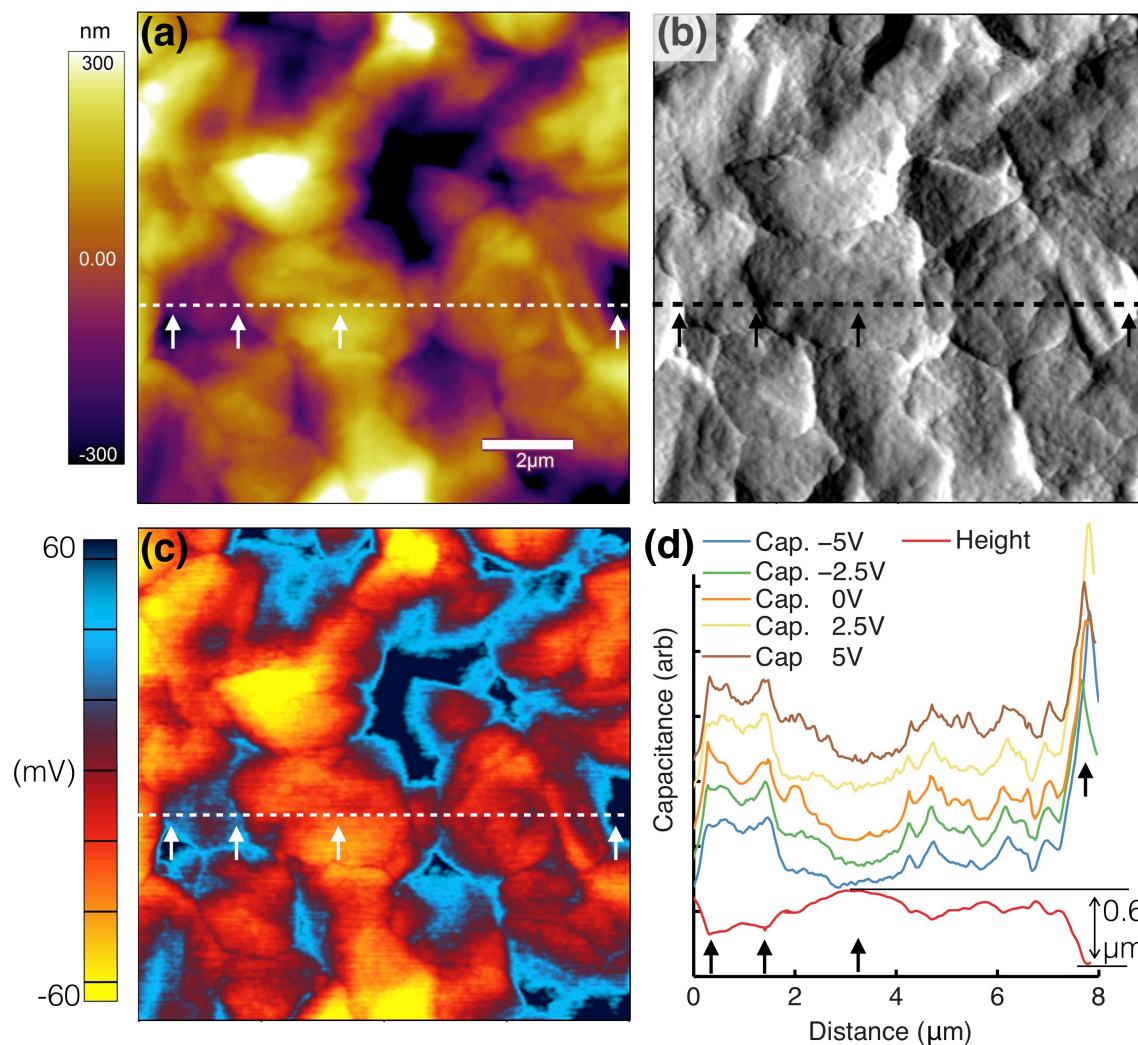


Figure 5.1: MIM imaging of CSS grown, CdCl_2 annealed CdTe sample with DC voltage applied to the tip. (a) Topography image, (b) Deflection (derivative of topography) image showing the enhanced microstructure of the CdTe film, (c) Simultaneously obtained capacitance data at 0V tip bias showing strong correlation with sample topography, and (d) Sample topography line scan along the dashed line shown in (a) along with the capacitance line scans at various tip voltages.

Note: The scale bar in (a) is common for all images. The capacitance data in (d) are deliberately put on a y-offset scale for clarity.

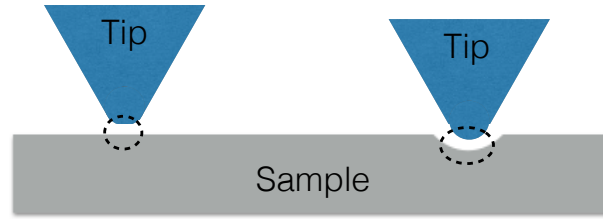


Figure 5.2: A cartoon showing the variation in tip-sample contact area as the MIM probe scans over a rough sample.

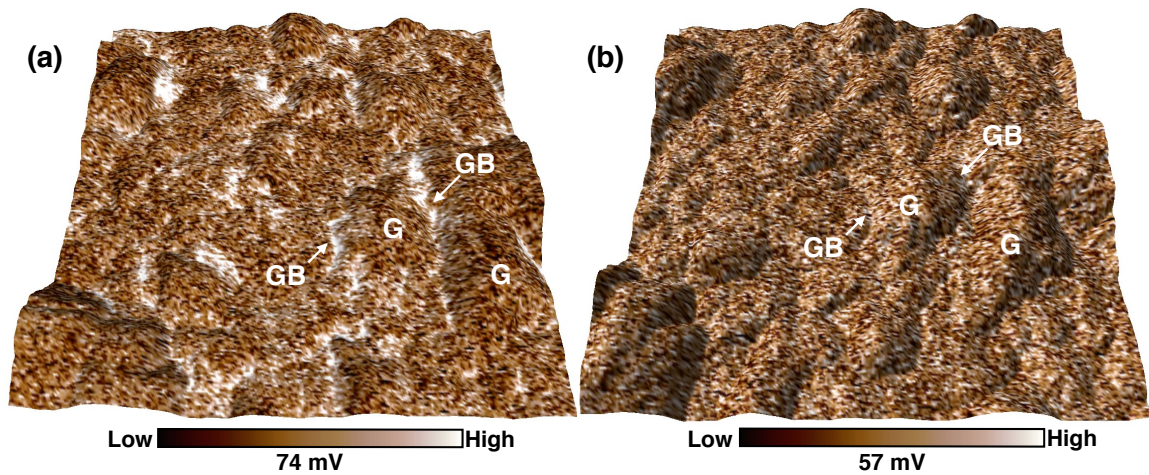


Figure 5.3 Lock-in MIM on CdCl_2 annealed, sputter-deposited CdTe sample. dC/dV amplitude signal obtained with (a) -2V and (b) +2V dc and 1V ac bias superposed on top of AFM topography. All scans are $5\text{ }\mu\text{m} \times 5\text{ }\mu\text{m}$ in area. rms roughness of the region is 140 nm. The contrast in the $|dC/dV|$ signal is washed out by changing the dc bias from -2V to +2V. Note: There is a lateral shift in image (a) and (b) due to sample drift in AFM. Corresponding grains (G) and grain boundaries (GB) are marked in both images. Image taken, with permission, from [14].

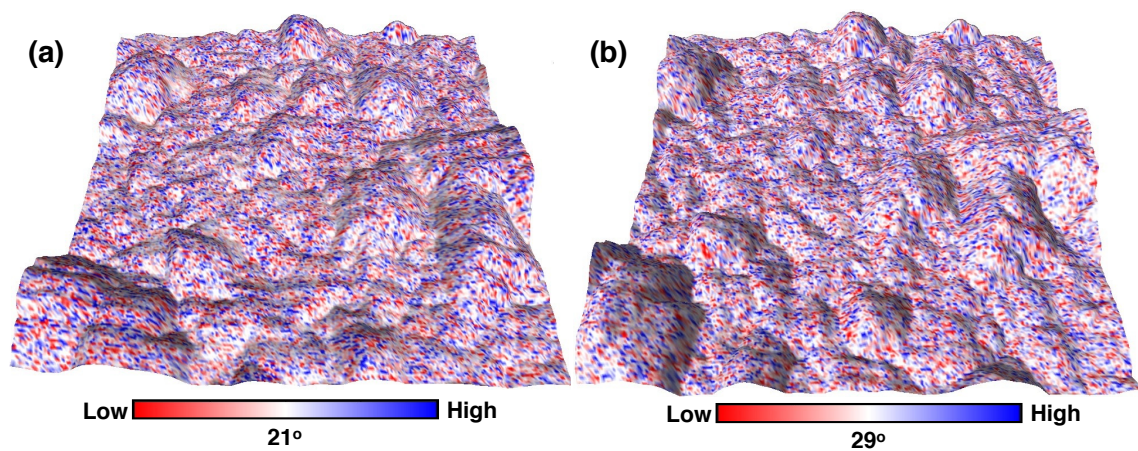


Figure 5.4: Corresponding dC/dV phase signal corresponding to (a) Figure 5.3(a) and (b) Figure 5.3(b) superposed on top of AFM topography. The phase signal corresponds to at most 29° phase variation in the scan area and has little correlation with $|dC/dV|$ data.

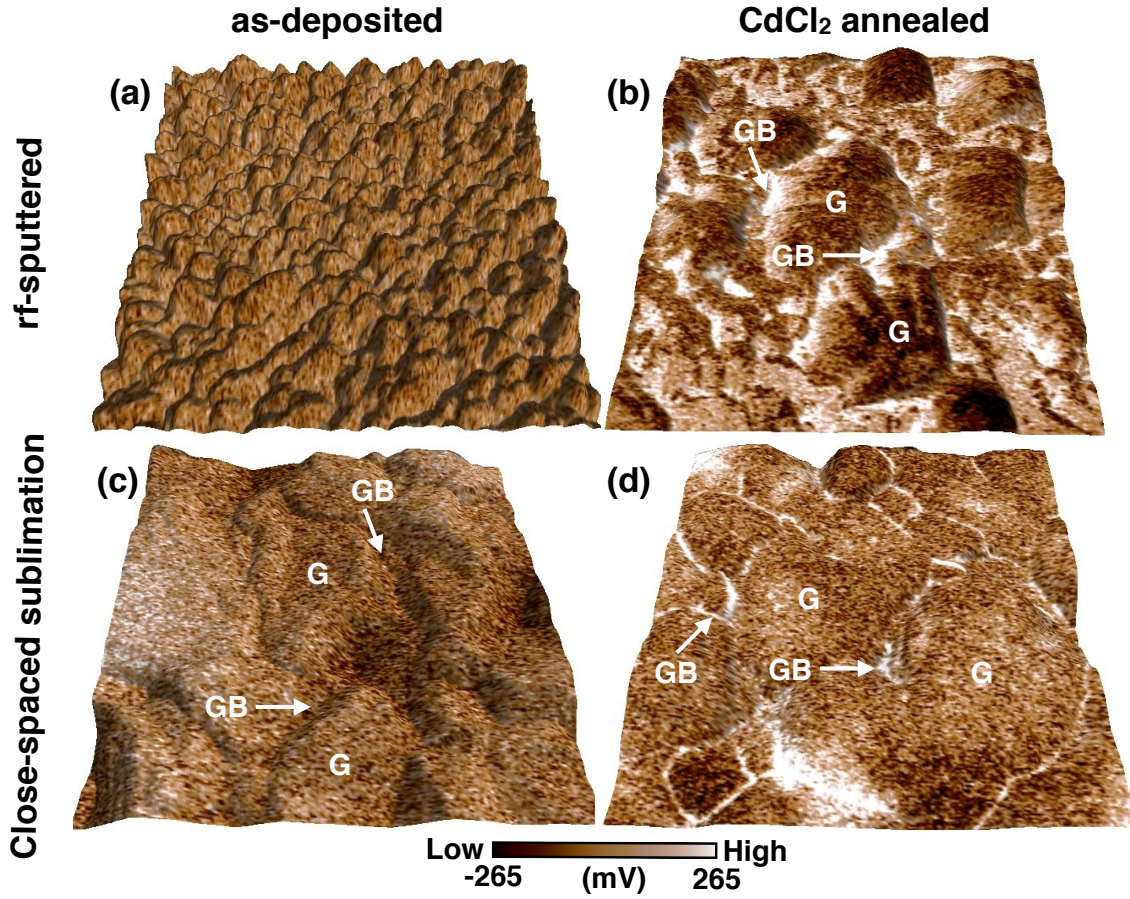


Figure 5.5: sMIM dC/dV amplitude data overlaid on AFM topographic images for the four samples studied. The signal qualitatively represents the hole concentrations, with high values representing low concentrations. The two CdCl₂ annealed samples show increased amplitude in the grain boundaries while the as-deposited samples do not. The scan areas are 5 μm x 5 μm . The RMS roughnesses are 27, 144, 163, and 145 nm for (a)-(d), respectively. Image taken, with permission, from [15].

Note: The color bar is common for all images and is centered at 0 mV. The actual variation from the center of the scale bar is ± 120 , ± 265 , ± 190 , and ± 240 mV for (a)-(d), respectively over the scan area. Sample grain (G) and grain boundary (GB) positions are marked.

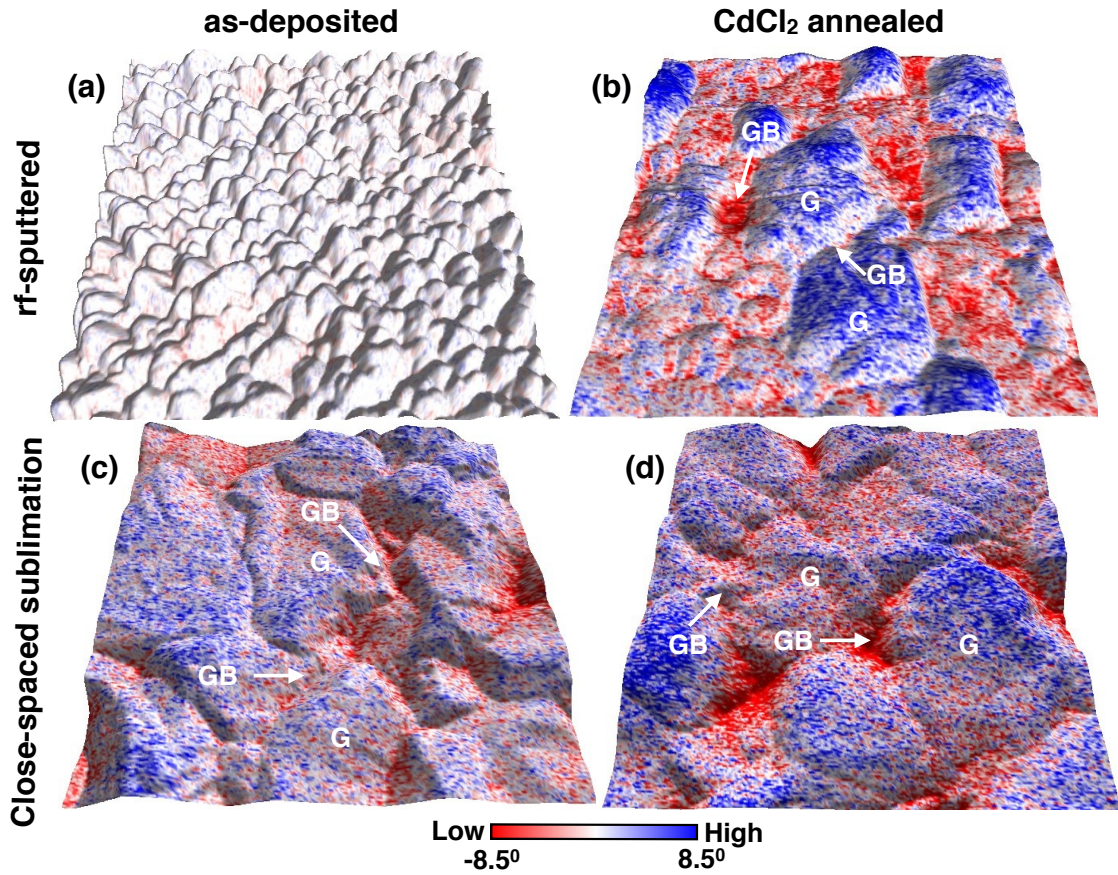


Figure 5.6: Corresponding sMIM dC/dV phase plots for Figure 5.4 overlaid on AFM topographic images for the four samples studied. For larger grains, the entire grain usually shows a slightly higher phase contrast compared to smaller grains. There is some correspondence with the amplitude data such that areas close to grain boundaries tend to show lower phase angles. However, the appearance of the phase plots is quite distinct from the amplitude plots. The as-deposited CSS film shows contrast in phase image but not in the amplitude plot. Image taken, with permission, from [15].

Note: The color bar is common for all images and is centered at 0°. The actual variation from the center of the scale bar is $\pm 2^\circ$, $\pm 8.5^\circ$, $\pm 6^\circ$, and $\pm 8^\circ$ for (a)-(d), respectively over the scan area. Sample grain (G) and grain boundary (GB) positions are marked.

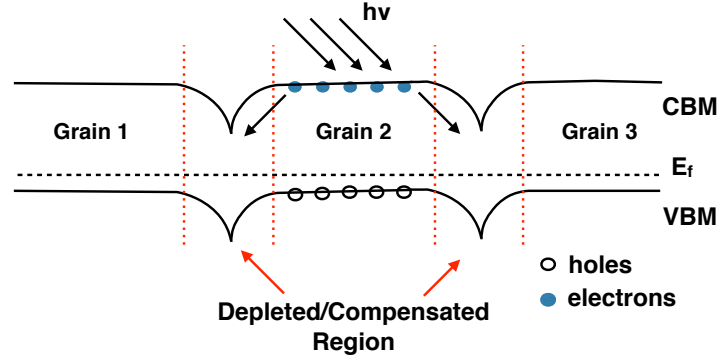


Figure 5.7: A cartoon diagram representing the p-doped CdTe grains separated by the relatively carrier depleted/compensated grain boundaries in polycrystalline CdTe, likely due to Cl segregation along grain boundaries. The band bending at the grain boundaries favors the separation of photo-generated electrons and holes. Image taken, with permission, from [15].

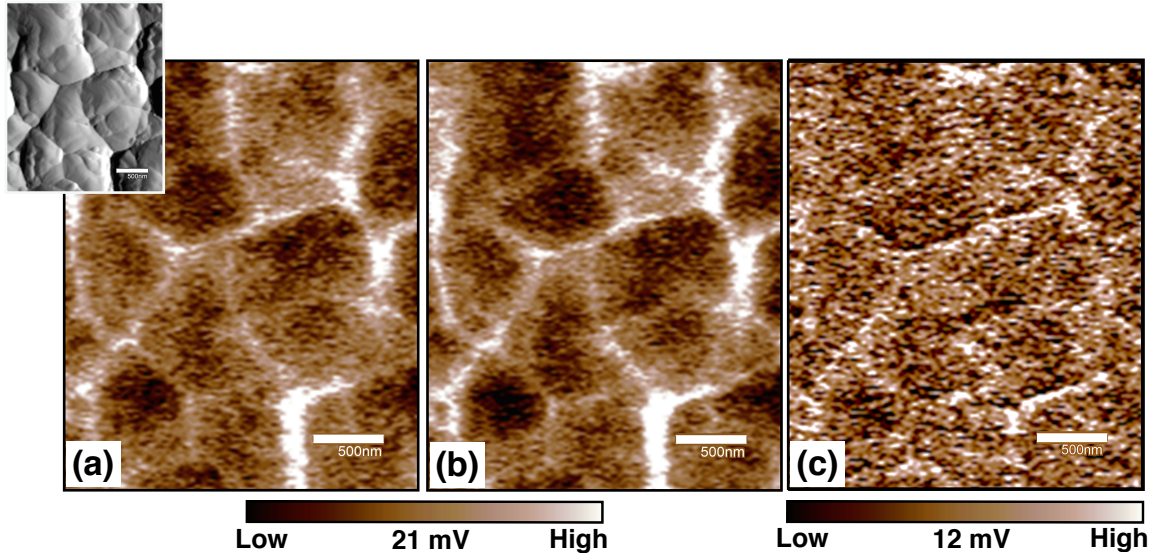


Figure 5.8: Analysis of sputter-deposited and CdCl₂ annealed sample. dC/dV amplitude signal image with 2V ac bias with (a) no sample illumination (b) sample illumination with white light. Notice the enhanced depletion around grain boundaries when sample is illuminated, as seen by the brighter signals along grain boundaries in (b). All scale bars are 500 nm. Color bar is common for (a) and (b). (c) is a result of subtraction of (a) from (b). Image taken, with permission, from [14].

Inset: Deflection (derivative of topography) image for the associated area. RMS roughness: 24 nm.

5.7 References

- [1] C. Li *et al.*, “Grain-Boundary-Enhanced Carrier Collection in CdTe Solar Cells,” *Phys. Rev. Lett.*, vol. 112, no. 15, p. 156103, Apr. 2014.
- [2] J. D. Poplawsky *et al.*, “Direct Imaging of Cl- and Cu-Induced Short-Circuit Efficiency Changes in CdTe Solar Cells,” *Adv. Energy Mater.*, vol. 4, no. 15, p. 1400454, Oct. 2014.
- [3] A. Abbas *et al.*, “The Effect of Cadmium Chloride Treatment on Close-Spaced Sublimated Cadmium Telluride Thin-Film Solar Cells,” *IEEE J. Photovolt.*, vol. 3, no. 4, pp. 1361–1366, Oct. 2013.
- [4] S. P. Harvey, G. Teeter, H. Moutinho, and M. M. Al-Jassim, “Direct evidence of enhanced chlorine segregation at grain boundaries in polycrystalline CdTe thin films via three-dimensional TOF-SIMS imaging,” *Prog. Photovolt. Res. Appl.*, vol. 23, no. 7, pp. 838–846, Jul. 2015.
- [5] D. j. Larson *et al.*, “Atom Probe Tomography Analysis of Grain Boundaries in CdTe,” *Microsc. Microanal.*, vol. 18, no. Supplement S2, pp. 928–929, Jul. 2012.
- [6] T. A. Gessert *et al.*, “Microscopic Analysis of Residuals on Polycrystalline CdTe Following Wet CdCl₂ Treatment,” in *Symposium H – II-IV Compound Semiconductor Photovoltaic Materials*, 2001, vol. 668.
- [7] I. Visoly-Fisher, S. R. Cohen, A. Ruzin, and D. Cahen, “How Polycrystalline Devices Can Outperform Single-Crystal Ones: Thin Film CdTe/CdS Solar Cells,” *Adv. Mater.*, vol. 16, no. 11, pp. 879–883, Jun. 2004.
- [8] W. Kundhikanjana, *Imaging nanoscale electronic inhomogeneity with microwave impedance microscopy*. 2013.
- [9] K. Lai, W. Kundhikanjana, M. A. Kelly, Z.-X. Shen, J. Shabani, and M. Shayegan, “Imaging of Coulomb-Driven Quantum Hall Edge States,” *Phys. Rev. Lett.*, vol. 107, no. 17, p. 176809, Oct. 2011.
- [10] Y. Liu, R. Ghosh, D. Wu, A. Ismach, R. Ruoff, and K. Lai, “Mesoscale Imperfections in MoS₂ Atomic Layers Grown by a Vapor Transport Technique,” *Nano Lett.*, vol. 14, no. 8, pp. 4682–4686, Aug. 2014.

- [11] K. Lai, W. Kundhikanjana, H. Peng, Y. Cui, M. A. Kelly, and Z. X. Shen, "Tapping mode microwave impedance microscopy," *Rev. Sci. Instrum.*, vol. 80, no. 4, p. 43707, Apr. 2009.
- [12] C. C. Williams, "Two-Dimensional Dopant Profiling by Scanning Capacitance Microscopy," *Annu. Rev. Mater. Sci.*, vol. 29, no. 1, pp. 471–504, 1999.
- [13] P. Sutter, E. Sutter, and T. R. Ohno, "High-resolution mapping of nonuniform carrier transport at contacts to polycrystalline CdTe/CdS solar cells," *Appl. Phys. Lett.*, vol. 84, no. 12, pp. 2100–2102, Mar. 2004.
- [14] M. Tuteja, P. Koirala, S. MacLaren, R. Collins, and A. Rockett, "Direct observation of electrical properties of grain boundaries in sputter-deposited CdTe using scan-probe microwave reflectivity based capacitance measurements," *Appl. Phys. Lett.*, vol. 107, no. 14, p. 142106, Oct. 2015.
- [15] M. Tuteja *et al.*, "Direct Observation of CdCl₂ Treatment Induced Grain Boundary Carrier Depletion in CdTe Solar Cells Using Scanning Probe Microwave Reflectivity Based Capacitance Measurements," *J. Phys. Chem. C*, vol. 120, no. 13, pp. 7020–7024, Apr. 2016.

CHAPTER 6

MICROSCALE ELECTRONIC CONDUCTIVITY

6.1 Introduction

In Chapter 5, it has been concluded that the CdCl_2 treatment results in majority carrier depletion/compensation at the grain boundaries of p-doped CdTe films, which aids carrier separation. The next step required for efficient device operation is the transport of these charge carriers to the appropriate contacts for extraction. The objective of this chapter is to study the microscale electrical conductivity of CdTe films, with emphasis on variation of conductivity from the grains to the grain boundaries in Glass/TCO/CdS/CdTe samples. The analysis is performed on the top surface of CdTe and current flow is measured across the CdTe film and into the TCO/CdS layers in order to study the properties of the CdTe film. Conductive atomic force microscopy (C-AFM), employing a conductive probe is used to study the nanoscale current conduction from the sample to the probe. This provides a direct observation of electronic conductivity of CdTe and the changes that occur in it during the CdCl_2 annealing process.

6.2 Results

Figures 6.1(a) and 6.1(b) show representative C-AFM current vs. sample voltage bias (I-V) plots along the grain bulk and the grain boundary regions for the as-deposited and CdCl_2 annealed CdTe samples, respectively. These curves have been obtained from sample locations as marked in Figures 6.3(a) and 6.4(a). It can be seen that it is only possible to pass relatively high currents through the CdTe samples, both CdCl_2 annealed and un-annealed, for relatively high (compared to device operating conditions) sample biases. Figures 6.2 show the semilog plots of the magnitude of current vs. sample voltage curves obtained at various grain and grain boundary locations from the as-deposited and CdCl_2 annealed CdTe samples. Analysis of the exponential dependence of current on voltage in Figures 6.2 show that even in the steepest sections of the curves the current increases too slowly with voltage to correspond to a normal diode behavior, even for a non-ideal diode. At higher voltages where the current is increasing only slowly with voltage the current appears to be limited by some series resistance, presumably in the

bulk of the material probed. It is important to note that in all curves presented in Figures 6.2 (and Figures 6.1) the transition from negative to positive current happens in the positive sample voltage regime (say, at a sample voltage V_0). This is not to be confused with a conventional photovoltaic effect. In these measurements for sample voltages $< V_0$, a small negative current (10s of pA) flows through the sample. This current is simply a result of a current offset that cannot be zeroed while performing the point I-V measurements in the C-AFM setup. Such small levels of current will not affect the results as presented in Figures 6.3 - 6.5 as the currents presented there are actual current flows through the sample and are much larger in magnitude than these small offset currents. It is also worth noting that because of the nature of the measurements, the accumulation of trapped charge in the sample can affect the current measurement. This can cause persistent changes in current or voltage that result in the hysteresis appearing in the curves plotted in Figures 6.1 and 6.2. This results in a slight shift in the “turn-on” voltage, V_0 , in the I-V spectra for the forward and reverse sweeps in the sample voltage. Also, this is potentially what leads to a current level difference of ~ 10 pA at negative sample voltages in the forward and reverse voltage sweep curves.

Figure 6.3(a) shows a deflection (derivative of topography) image for the as-deposited CdTe sample. It is assumed here that the grain boundaries are defined primarily by topography such that grains are delimited by the large consistent surface protrusions and the grain boundaries are the regions between these features. This is consistent with electron backscatter diffraction mapping measurements (not shown). The corresponding C-AFM current images acquired at +2V of sample bias on this as-deposited CdTe sample, without and with external illumination by the optical microscope light, are shown in Figures 6.3(b) and 6.3(c), respectively. Figure 6.3(d) is a superposition of areas of Figures 6.3(b) and 6.3(c), corresponding to the area indicated in Figure 6.3(a), after color-coding them red and green, respectively. The areas of Figure 6.3(d) that appear red indicate greater current in the dark, while areas that appear green indicate greater current under light. The areas that appear yellow in Figure 6.3(d) indicate areas of higher current flow in the sample regardless of the illumination. The green colored appearance of several areas corresponding to grains in Figure 6.3(d) indicates that external illumination of the sample results in current flow along areas of the grains that did not conduct well in

the absence of illumination [see also Figure 6.1(a)].

Figure 6.4(a) shows a deflection image for the CdCl₂ annealed CdTe sample. The corresponding C-AFM current images obtained at +2V sample bias, without and with external illumination, are shown in Figures 6.4(b) and 6.4(c), respectively. Figure 6.4(d) is a superposition of areas of Figures 6.4(b) and 6.4(c), corresponding to the area indicated in Figure 6.4(a), after color-coding them red and green, respectively. Figures 6.4(b) and 6.4(c) show some inter-grain current variations but most prominently reveal that the current conduction is much more uniform across all of the grains in the scan area as compared to the case for the as-deposited sample. The darker horizontal lines at the bottom of Figure 6.4(c) are scan artifacts which are likely a result of minor tip contamination during the repeated contact mode scans. Most grains in Figure 6.4(d) have a yellow appearance indicating that these correspond to areas of high C-AFM current flow in the sample regardless of external illumination. The absolute enhancement of the maximum C-AFM current in the treated sample is similar to that in the untreated sample, although the relative increase is smaller. As can be seen from Figure 6.4(d), several grain boundary areas are dark, which indicates that regardless of illumination there is little or no current flow along those grain boundaries in the reverse breakdown condition for the main junction. The fact that in Figures 6.4(b) and 6.4(c) the concave areas of the surface (along the grain boundaries) do not correlate with high current, rules out the possibility that sample topography artifacts (high current due to increased tip-sample contact area along the grain boundaries) dominate the C-AFM measurements.

The measurements have also been performed under more extreme bias conditions, which are far from the conventional operation conditions of a CdTe solar cell. Figures 6.5(a) and 6.5(b) show the dark C-AFM current map on the as-deposited CdTe sample along the scan area as shown in Figure 6.3(a) at sample bias conditions of +6V and -6V, respectively. Under +6V sample bias [Figure 6.5(a)] the current is uniformly distributed across the scan area with both the grains and the grain boundaries acting as current conduction paths. Under -6V sample bias [Figure 6.5(b)] the C-AFM currents observed are much lower due to the reverse biased Schottky contact at the CdTe/Pt junction. Figures 6.5(c) and 6.5(d) show the dark C-AFM current maps on the CdCl₂ annealed

CdTe sample along the scan area as shown in Figure 6.4(a) at sample bias conditions of -6V and +6V, respectively. Similar to the case of Figure 6.5(b), Figure 6.5(c) shows that a large part of the scan area has low levels of C-AFM current, due to reverse biased Schottky contact. Figure 6.5(d) shows the C-AFM current map for +6V sample bias, where the main junction is heavily reverse biased (as compared to operation conditions of the solar cell). It can be seen that under this measurement condition the largest C-AFM current flows along the grain boundary areas as compared with the grain interiors.

6.3 Discussion

The estimates of the valence band energy in CdTe (6eV, from vacuum level to valence band maximum) [1] and the work function of Pt (5.1-5.5 eV) [2] indicate that the creation of a high Schottky barrier between the CdTe film and the Pt-probe is expected. The p-n junction diode (CdS/CdTe) and the Schottky diode (CdTe/Pt) are oriented in opposite directions. Therefore one diode is always reverse biased and would be expected to determine the resistance of the device overall. This is indeed what is observed. With positive voltage applied to the sample, the back Schottky contact is forward biased and the reverse biased junction is the main diode. Thus, the behavior illustrated in Figure 6.1 for both samples is dominated by reverse breakdown in the main CdS/CdTe junction in the positive sample bias regime. This reverse current flowing through the p-n junction diode increases exponentially with voltage and is referred to as *pre-breakdown reverse current*. This has been a subject of many investigations in the past [3]–[6] and some studies have concluded that such reverse currents primarily arise due to material defects/imperfections in the case of polycrystalline solar cells [5], [6]. The current density in the light is much higher than in the dark for the untreated sample, even though the illumination is weak and no significant short circuit current is observed. When a Schottky contact is forward biased, it leads to a flow of majority carriers from the semiconductor into the metal [7]. For the p-doped CdTe, this means that the C-AFM current observed in the positive sample bias regime is normally composed of holes flowing from the CdTe layer into the Pt-tip. When the main CdS/CdTe junction is under sufficient reverse bias to be in a breakdown condition, it loses its rectifying characteristics and allows hole current to pass through the p-n junction relatively freely. The C-AFM current variations in

this case would normally be expected to represent the variation in microscale electrical conductivity of the CdTe film for the flow of the majority charge carriers (holes) from the p-n junction to the Schottky contact.

The CdTe layer is p-doped to a carrier concentration of (10^{14} - 10^{15} cm⁻³) [8] and it is likely that an incorporation of Cl along the grain boundaries results in formation of a narrow region of, at least, quasi-intrinsic CdTe. The Schottky diode is primarily a majority carrier device with a very small fraction of minority carrier injection current. However, at large forward voltage biases to the Schottky diode, a low acceptor doping in CdTe (for example in the grain boundaries) and a large Schottky barrier height for majority carrier flow, electron injection into CdTe along the grain boundaries can be expected to be more favorable than hole injection into the Pt-tip. These electrons would be collected spontaneously at the reverse-biased main junction to the grain boundary (assuming that the boundaries run through the thickness of the CdTe).

It is concluded that when the tip is positioned over the p-doped CdTe grains, the charge motion is holes into the tip from the grains at all positive sample biases and current is controlled by the main junction breakdown current. However, along the grain boundaries in the CdCl₂ annealed sample, electron injection from the Pt-tip into the CdTe is likely and increases as the positive voltage bias is increased. This current may be collected directly by the reverse-biased main junction. In the negative sample bias regime, the p-n junction is forward biased and current flow should occur by injection of electrons into the p-type CdTe by the p-n junction. This current is limited due to either electron collection by the sample tip or by recombination with the reverse hole current in the Schottky contact.

It can be seen from Figure 6.3(b) (for the as-deposited sample) that under positive sample bias conditions, in the absence of external illumination, the current flows from the TCO layer to the Pt-tip primarily along the grain interiors, presumably as holes. Further, there is large inhomogeneity in electrical conductivity from one grain to the other. This point is further illustrated by Figures 6.2 (a) and (b), both displaying high variability in the current levels and “turn-on” voltages (the positive voltages at which the current starts

to flow) among the various grains and the grain boundaries. It is also interesting to note the hysteresis in some of the I-V curves in Figures 6.1 and 6.2. This can be attributed to charge trapping in defects resulting from currents in the high sample bias regimes. The enhancement of the current in several grains [green areas in Figure 6.3(d)] demonstrates the photoconductivity effect, near the surface, of the CdTe film. Upon comparing Figures 6.1(a) and 6.1(b), and Figures 6.3(b) and 6.4(b) it can be seen that, in the +2V sample bias regime, the currents flowing through the CdTe film are a factor of ~ 8 greater after the CdCl₂ anneal treatment as compared with the as-deposited samples. This indicates that the electrical conductivity of the CdTe film has improved upon the CdCl₂ anneal treatment. By comparison of Figures 6.3(b) and 6.4(b) it can also be seen that after the CdCl₂ anneal treatment the current distribution along the grains in the sample becomes much more homogenous as compared to the as-deposited sample. This point is also illustrated by Figures 6.2(c) and 6.2(d), where the I-V curves collected at various grain and grain boundary locations on the CdCl₂ annealed sample are more well-behaved showing a more consistent “turn-on” voltage and resistance. Hence, the CdCl₂ treatment makes the electrical properties of the grains in the CdTe film more homogenous and increases their electrical conductivity for the flow of holes.

In Figures 6.4 (low bias) there is considerable variation in grain boundary conductivity relative to the surrounding grains including both significantly higher and significantly lower currents as shown in the Figure 6.6 where a line scan across part of the area in Figure 6.4(c) is shown and the topography and C-AFM currents are compared. This is consistent with our previous findings that not all grain boundaries show similar amounts of carrier depletion/compensation following CdCl₂ treatment [9], [10]. At higher +6V bias [Figure 6.5(d)] there is strong contrast between the grains and grain boundaries with several boundaries conducting much higher current. In this case the current flow along the grain boundaries is due to electron injection from the Pt-tip. A key point here is that the holes injected into the grain interiors by the p-n junction under reverse breakdown do not simply flow through the highly conductive grain boundaries. They are blocked from the grain boundaries by the junction between the more p-type grains and the less p-type or somewhat n-type Cl-doped grain boundaries. In all cases where the grain boundaries are conductive the adjacent grains do not appear to transfer holes to

those conductive channels over significant distances. Finally, some grain boundaries in Figure 6.5(d) are at similar current levels to the adjacent grains [one example marked by arrows in Figures 6.4(a) and 6.5(d)]. This further proves that the incorporation of Cl along the boundaries and the resultant doping effects are not uniform across all the grain boundaries. There is no major current contrast observed between the grains and the grain boundaries for the as-deposited sample at +6V bias, as shown in Figure 6.5(a).

6.4 Conclusions

The CdCl_2 treatment homogenizes and increases the electrical conductivity of CdTe films. Doping of the grain boundaries promotes charge separation, collection of electrons by the grain boundary, and their conduction to the front contact of the device. This is supported by the observation here of high current in the grain boundary under conditions where electrons are expected to be the dominant charge carrier. In the CdCl_2 annealed sample, the lack of conduction of holes injected into the grains through the grain boundaries to the back contact shows why recombination in the device operating as a photovoltaic does not occur at the grain boundaries. In the complete device the p-type doping of the back of the CdTe by the back contact prevents shunting through the conductive grain boundaries. Finally, the photoconductivity effect observed here shows that exposure of CdTe film to light leads to promotion of current flow in both the grains and grain boundaries.

6.5 Figures

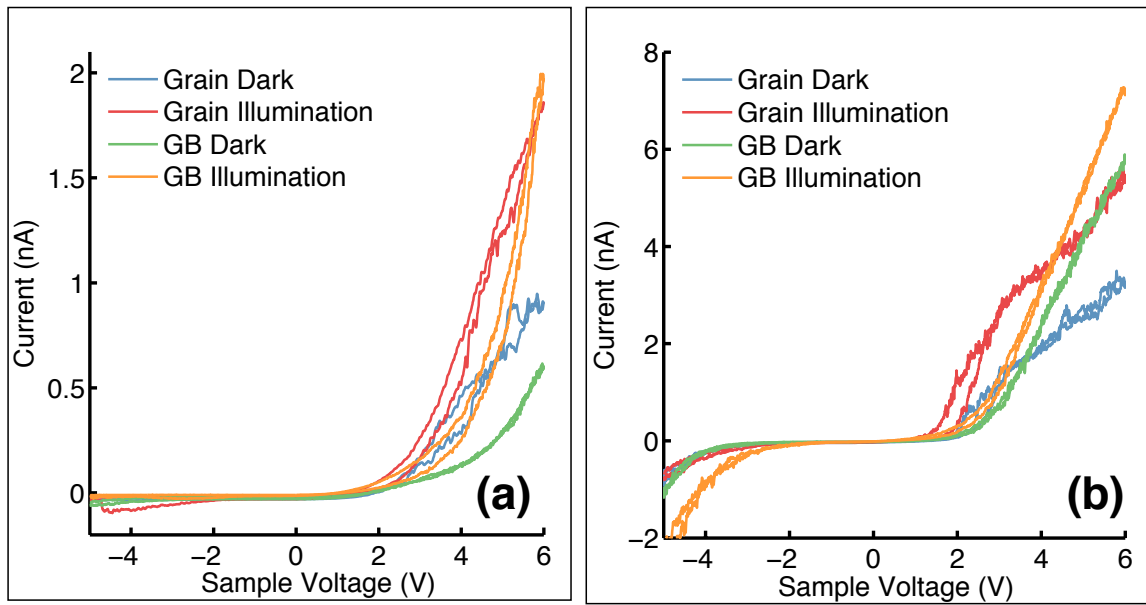


Figure 6.1: C-AFM current vs. sample bias curves for the (a) as-deposited and (b) CdCl_2 annealed CdTe sample. The data for grains and grain boundaries are taken at spots 1 and 2 as indicated in Figures 6.3(a) and 6.4(a), respectively.

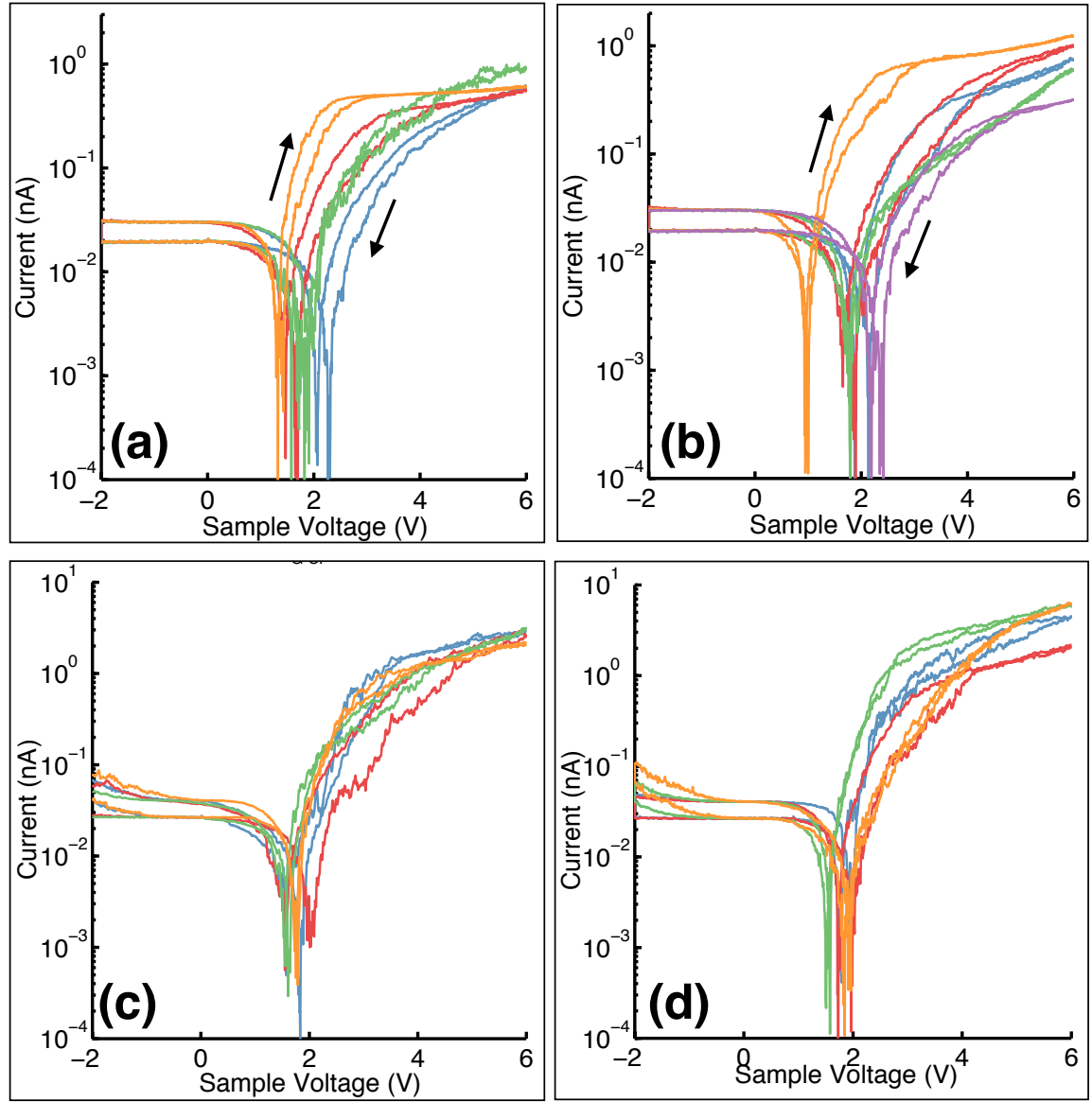


Figure 6.2: Semilog plots of dark magnitude of current-voltage curves measured at several grain [(a), (c)] and grain boundary [(b), (d)] positions on the as-deposited [(a), (b)] and CdCl_2 annealed [(c), (d)] samples. In each image, different colored curves represent measurements from different locations on the sample.

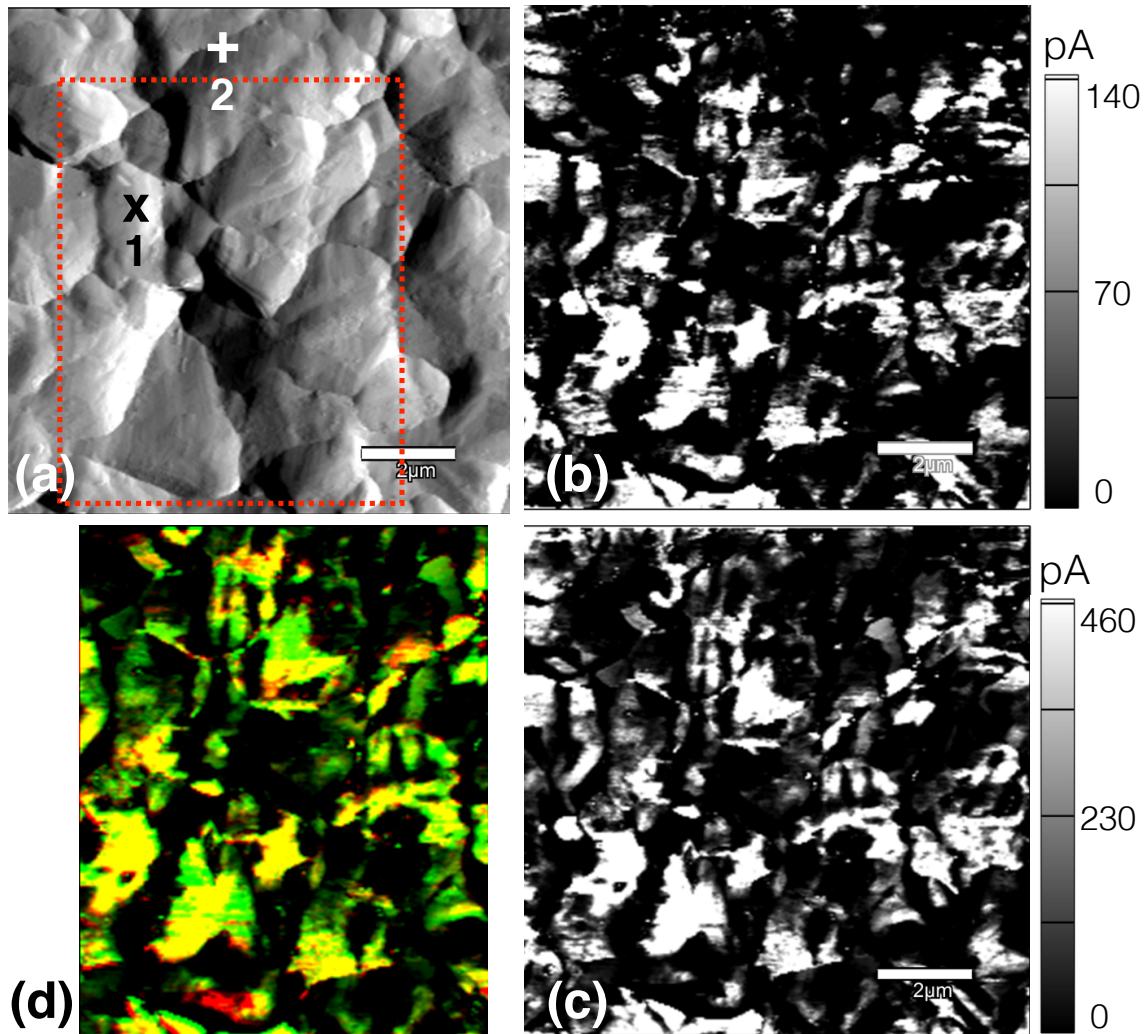


Figure 6.3: C-AFM analysis of an as-deposited CdTe sample. (a) Deflection (derivative of topography) image for the scan area to highlight the topographical features. C-AFM current maps of the sample in (b) the absence, and (c) the presence of weak external sample illumination. (d) Superposition of red color-coded image (b) with green color-coded image (c). Note: RMS roughness of the scan area is 165 nm. All images represent the same scan area and the scale bars represent 2 μm in length.

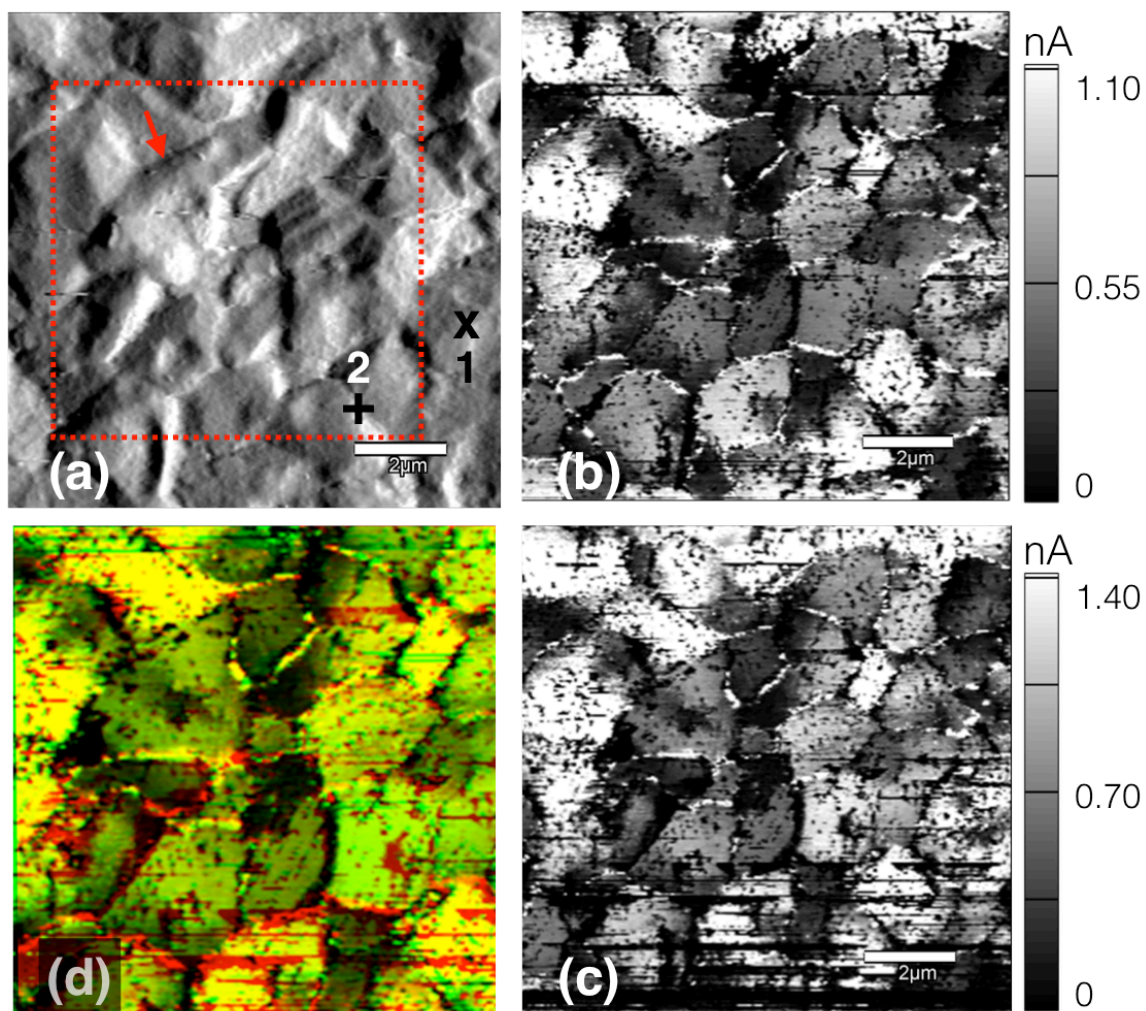


Figure 6.4: C-AFM analysis of a CdCl₂ annealed CdTe sample. (a) Deflection (derivative of topography) image for the scan area to highlight the topographical features. C-AFM current maps of the sample in (b) the absence, and (c) the presence of weak external sample illumination. (d) Superposition of red color-coded image (b) with green color-coded image (c). Note: The RMS roughness of scan area is 135 nm. All images represent the same scan area and the scale bars represent 2 μm in length.

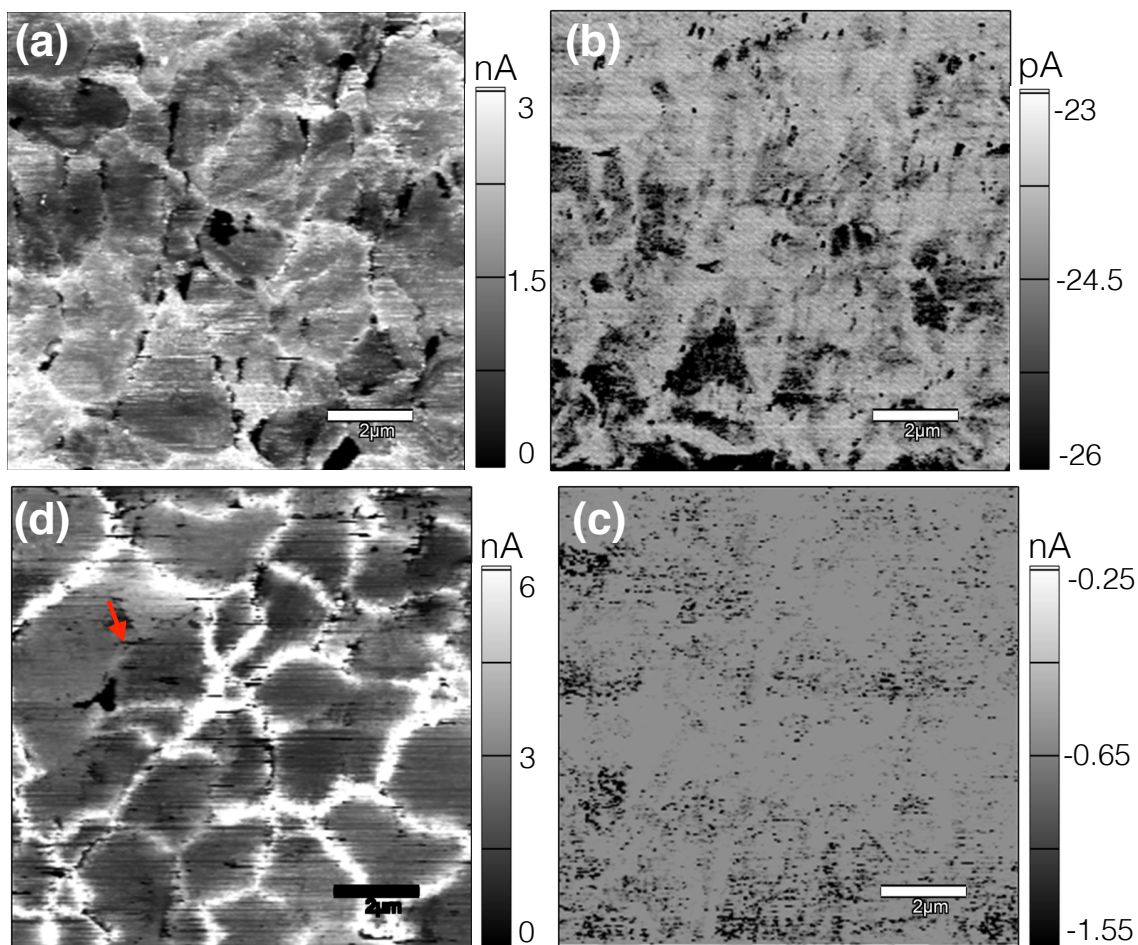


Figure 6.5: C-AFM current maps acquired at +6V [(a) and (d)] and -6V [(b) and (c)] sample bias for the as-deposited [(a) and (b)] and CdCl₂ annealed [(c) and (d)] CdTe samples.

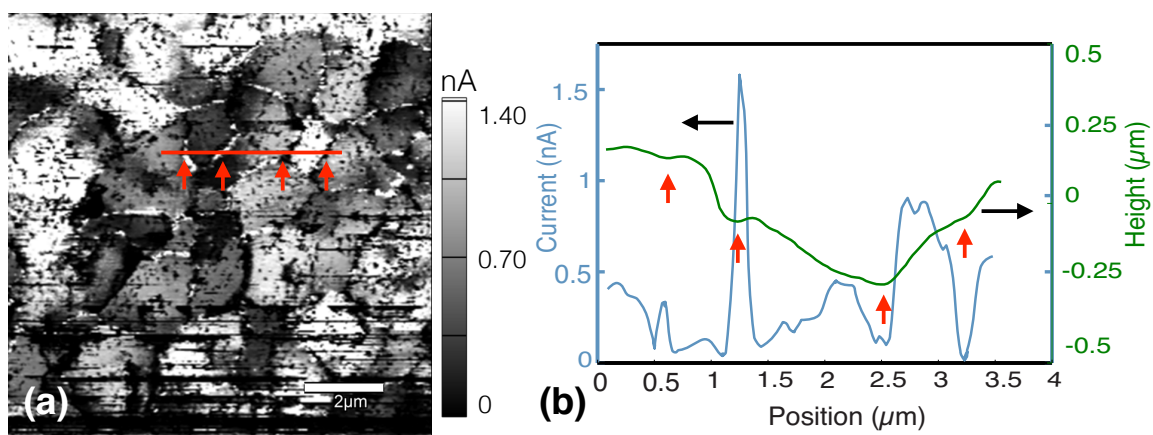


Figure 6.6: (a) A reproduction of Figure 6.4(c), and (b) topography (height) and current data along the red line in image (a). The arrows in images (a) and (b) indicate the same spatial grain boundary positions.

6.6 References

- [1] S. G. Kumar and K. S. R. K. Rao, “Physics and chemistry of CdTe/CdS thin film heterojunction photovoltaic devices: fundamental and critical aspects,” *Energy Environ. Sci.*, vol. 7, no. 1, pp. 45–102, Dec. 2013.
- [2] H. B. Michaelson, “The work function of the elements and its periodicity,” *J. Appl. Phys.*, vol. 48, no. 11, pp. 4729–4733, Nov. 1977.
- [3] M. C. Alonso-García and J. M. Ruíz, “Analysis and modelling the reverse characteristic of photovoltaic cells,” *Sol. Energy Mater. Sol. Cells*, vol. 90, no. 7–8, pp. 1105–1120, May 2006.
- [4] O. Breitenstein, J. Bauer, J.-M. Wagner, and A. Lotnyk, “Imaging physical parameters of pre-breakdown Sites by lock-in thermography techniques,” *Prog. Photovolt. Res. Appl.*, vol. 16, no. 8, pp. 679–685, Dec. 2008.
- [5] D. Lausch *et al.*, “Identification of pre-breakdown mechanism of silicon solar cells at low reverse voltages,” *Appl. Phys. Lett.*, vol. 97, no. 7, p. 73506, Aug. 2010.
- [6] O. Breitenstein, J. Bauer, A. Lotnyk, and J.-M. Wagner, “Defect induced non-ideal dark – characteristics of solar cells,” *Superlattices Microstruct.*, vol. 45, no. 4–5, pp. 182–189, Apr. 2009.
- [7] S. m. Sze and K. K. Ng, “Metal-Semiconductor Contacts,” in *Physics of Semiconductor Devices*, John Wiley & Sons, Inc., 2006, pp. 134–196.
- [8] B. E. McCandless and J. R. Sites, “Cadmium Telluride Solar Cells,” in *Handbook of Photovoltaic Science and Engineering*, A. Luque and S. Hegedus, Eds. John Wiley & Sons, Ltd, 2011, pp. 600–641.
- [9] M. Tuteja *et al.*, “Direct Observation of CdCl₂ Treatment Induced Grain Boundary Carrier Depletion in CdTe Solar Cells Using Scanning Probe Microwave Reflectivity Based Capacitance Measurements,” *J. Phys. Chem. C*, vol. 120, no. 13, pp. 7020–7024, Apr. 2016.
- [10] M. Tuteja, P. Koirala, S. MacLaren, R. Collins, and A. Rockett, “Direct observation of electrical properties of grain boundaries in sputter-deposited CdTe using scan-probe microwave reflectivity based capacitance measurements,” *Appl. Phys. Lett.*, vol. 107, no. 14, p. 142106, Oct. 2015.

CHAPTER 7

CONCLUSIONS

7.1 Conclusions

Low temperature photoluminescence (PL) spectra from sputter-deposited CdTe surfaces and CdS/CdTe junctions, and their line shape and temperature quenching behavior reveal that the dominant emission peaks primarily arise from free-to-bound/donor-acceptor and bound excitonic recombinations. A detailed analysis of temperature and excitation power dependence of the PL spectra reveal the most prominent efficiency limiting defects in these films. These defects arise from Cl-related defect complexes, which are de-activated by the incorporation of Cu in the device, hence, pointing to the role of Cu in plugging recombination routes in the device. The similarities between the PL spectra of polycrystalline (rf-sputtered and CSS-grown) and single crystal CdTe samples indicate that defect-assisted carrier recombinations are not limited to polycrystalline samples. Hence, a probe into the macro-scale electronic behavior of the polycrystalline samples cannot alone explain the observation of lower open-circuit voltages (V_{OC}) in these devices.

Micro scale majority carrier concentration reduction along the grain boundaries in CdCl₂ annealed CdTe films deposited by both sputtering and CSS reveal the grain boundary carrier depletion/compensation due to Cl incorporation. This creates a downward band bending along the grain-grain boundary interface, which facilitates photo-generated carrier separation such that electrons separate out into the boundaries while holes stay in the grain bulk. This effect is in addition to the charge separation at the main junction. Further, micro scale electronic conductivity measurements reveal that CdCl₂ treatment homogenizes and increases the electrical conductivity of CdTe films, hence, promoting the flow of electrons to the front contact along the boundaries, and flow of holes to the back contact along the grain interiors. In addition during the anneal process, the crystalline quality of the grains improved by gettering of defects and impurities into the boundaries, which inhibits recombination in the grain bulk, and the absence of bulk majority carriers in the boundaries leads to a reduction in the overall recombination in the cell, and improved collection of photo-generated carriers.

The V_{OC} in polycrystalline cells is only $\sim (800-900)$ mV, lower than the value of $>1V$ for monocrystalline CdTe cells [1], however, the overall device efficiency for crystalline CdTe solar cells is still lower. This can be explained based on the carrier depleted grain boundaries, ending at the CdS/CdTe junction, connected *in parallel* with the main cell junction, which will decrease the V_{OC} of the cell (as V_{OC} is less than the built-in voltage at the junction). This effect is shown in Figure 7.1. Further, due to carrier depleted grain boundaries, the effective junction area (A) that participates in the carrier collection increases. This results in an observation of lower V_{OC} for polycrystalline devices as an increase in A reduces the photovoltage needed to balance out the photocurrent.

7.2 Suggested Optimal Device Structure

According to the description outlined above, it might seem that an increase in the grain boundary density (through reduced grain size) will increase the charge separation and provide more routes for photo-generated electron transport. However, in polycrystalline CdTe cells, with carrier depleted boundaries, this will also imply that holes would have to cross some grain boundary barriers before collection at the back contact, as shown in Figure 7.2 (a). Therefore, decreased grain size will also potentially increase the avenues for carrier recombination.

From the advantageous and the harmful effects of grain boundaries in CdTe solar cells, it seems that the average grain size (diameter of $1-3 \mu m$) in the film, as found in empirically optimized devices, represents a good compromise between the various effects noted above. It is suggested that with columnar rather than isotropic grains, of diameters greater than the depletion width at the grain/grain boundary interface ($\sim 100-150$ nm), the electron and hole current pathways will be well-segregated and run un-interrupted, resulting in improved cell performance. This is, in-fact, observed in the case of empirically optimized polycrystalline CdTe solar cells (see Figure 7.3), where several of the CdTe grains run through the thickness of the CdTe film. It is important to note that the process of deposition of the back contact involves p-doping of the back surface of CdTe, away from the glass side, which prevents shunting of the device.

Hence, I conclude that in order to further enhance the performance of polycrystalline CdTe solar cells, alternate deposition methods/conditions for CdTe should be researched such that the growth of columnar CdTe grains (with axis perpendicular to the CdS/CdTe junction) is promoted, as shown in Figure 7.2 (b).

7.3 Figures

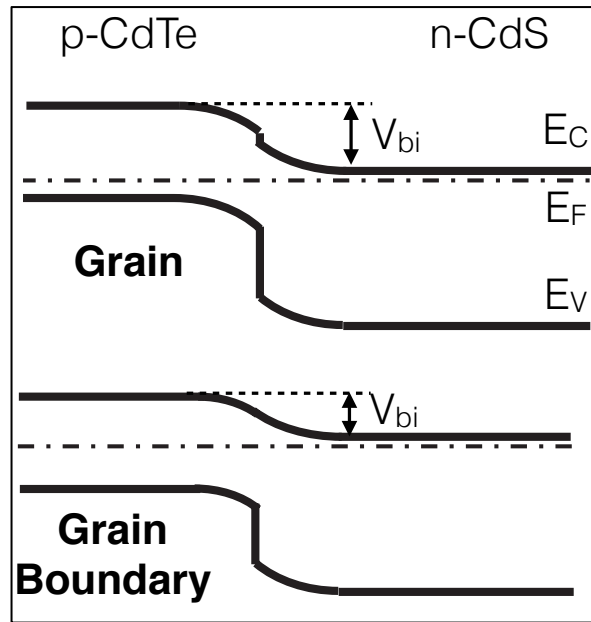


Figure 7.1: The reduction of built-in voltage (and hence photovoltage) at the p-n junction along the carrier depleted grain boundaries as compared to the p-doped CdTe grains.

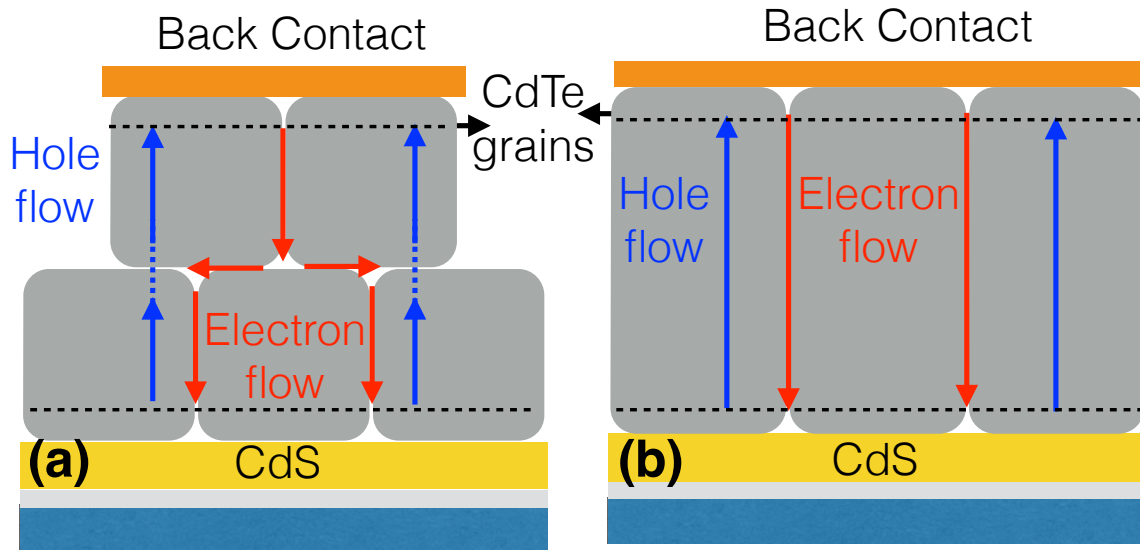


Figure 7.2: A schematic CdTe grain structure showing (a) small grains such that the grain boundaries cross the hole current paths, and (b) long columnar grains that run through the thickness of the CdTe film, such that the hole and electron current paths run uninterrupted.

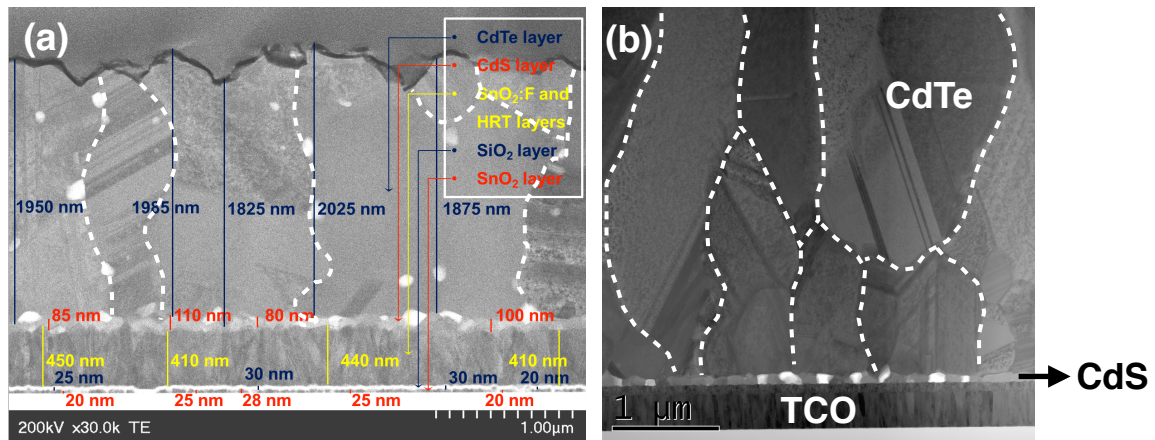


Figure 7.3: Cross-sectional TEM images of (a) rf-sputtered, and (b) CSS grown CdS/CdTe solar cells showing the existence of large columnar-type CdTe grains running through the thickness of the CdTe film. Image courtesy: (a) Dr. Robert Collins and (b) Dr. Chris Ferekides.

7.4 Reference

- [1] J. M. Burst *et al.*, “CdTe solar cells with open-circuit voltage breaking the 1 V barrier,” *Nat. Energy*, vol. 1, no. 3, p. 16015, Feb. 2016.